

Electronic Thesis and Dissertation Repository

4-22-2019 1:00 PM

Effect of ATRX Inactivation on Hippocampal Synaptic Plasticity in Mice

Radu Gugustea, *The University of Western Ontario*

Supervisor: Berube, Nathalie G., *The University of Western Ontario*

Co-Supervisor: Leung, Stan L., *The University of Western Ontario*

A thesis submitted in partial fulfillment of the requirements for the Master of Science degree in Neuroscience

© Radu Gugustea 2019

Follow this and additional works at: <https://ir.lib.uwo.ca/etd>



Part of the [Neuroscience and Neurobiology Commons](#)

Recommended Citation

Gugustea, Radu, "Effect of ATRX Inactivation on Hippocampal Synaptic Plasticity in Mice" (2019).
Electronic Thesis and Dissertation Repository. 6118.
<https://ir.lib.uwo.ca/etd/6118>

This Dissertation/Thesis is brought to you for free and open access by Scholarship@Western. It has been accepted for inclusion in Electronic Thesis and Dissertation Repository by an authorized administrator of Scholarship@Western. For more information, please contact wlsadmin@uwo.ca.

Abstract

The *ATRX* gene encodes an ATP-dependent chromatin remodeling factor and gene mutations cause developmental defects and intellectual disability. Conditional ablation of *Atrx* in mouse postnatal forebrain excitatory neurons (ATRX-KO) leads to spatial learning and memory impairments. Thus, we hypothesized that hippocampal synaptic transmission and plasticity are disrupted in ATRX-KO mice. Long-term potentiation (LTP), a cellular correlate of memory, and input-output relation of paired-pulse responses were studied in urethane-anesthetized mice *in vivo*. Theta-burst stimulation (TBS) of stratum oriens induced robust basal dendritic LTP in CA1 of both ATRX-KO and control mice, while paired-pulse facilitation (PPF) during baseline was lower in ATRX-KO mice. TBS of the medial perforant path induced CA1 distal apical dendritic LTP in control mice but was significantly decreased in ATRX-KO mice. The defects we identified in hippocampal synaptic transmission and LTP may underlie the memory impairments previously identified in the mutant mice.

Keywords

Hippocampus; learning; memory; synaptic plasticity; ATRX; ATR-X syndrome; intellectual disability; knockout; mice; CA1; CA3; DG; apical dendrites; basal dendrites; LTP; PPF; Schaffer collaterals; perforant path; temporoammonic pathway; trisynaptic circuit

Acknowledgments

Thank you to everyone that has helped me along the way with this project; I would not have been able to complete it without your help, guidance, and feedback. A special thanks goes to my co-supervisors, Dr. L Stan Leung and Dr. Nathalie G Bérubé, for their immense support and continual guidance throughout the past two years; this work would not be possible without your contributions. A sincere thank you goes to those individuals that I have collaborated with to bring this project to fruition, from our lab technician, Liangwei Chu, to Renee Tamming and other colleagues at Victoria Hospital. I have grown personally and professionally because of each and every one of you, so I thank you for that. I would like to thank my Advisory Committee, Dr. Arthur Brown and Dr. Wataru Inoue, for their insightful feedback and advice throughout my project. Finally, I would like to thank the Schulich School of Medicine and Dentistry as well as the Neuroscience Graduate Program at Western University for making this research possible.

Table of Contents

Abstract.....	i
Acknowledgments.....	ii
Table of Contents	iii
List of Figures	vii
List of Abbreviations	xi
Chapter 1.....	1
1 Introduction.....	1
1.1 Learning and Memory Literature Review.....	1
1.1.1 Discovery of Hippocampal Function	1
1.1.2 Hippocampal Anatomy	2
1.1.3 Hippocampal Neurotransmission.....	4
1.1.4 Hippocampal Function.....	6
1.1.5 Synaptic Plasticity.....	7
1.2 Intellectual Disability Literature Review	11
1.2.1 Intellectual Disability.....	11
1.2.2 ATR-X Syndrome.....	12
1.2.3 <i>ATRX</i> Gene and Protein	14
1.2.4 Role of <i>ATRX</i> in Learning & Memory	16
1.3 Rationale and Aims.....	17
1.3.1 Rationale	17
1.3.2 Aims.....	18
Chapter 2.....	19
2 Materials and Methods.....	19
2.1 Animal Husbandry/Genotyping.....	19

2.2	Electrode Specifications.....	19
2.3	Experimental Protocol	20
2.3.1	Surgery	20
2.3.2	Electrode Implantation and Optimization.....	21
2.3.3	Experimental Paradigm.....	24
2.3.4	Electrode Verification.....	26
2.4	Inclusion Criteria	28
2.5	Experimental Recordings.....	28
2.5.1	Raw Data.....	28
2.5.2	Current Source Density Analysis.....	29
2.6	Data and Statistical Analyses.....	30
2.6.1	LTP Analysis	30
2.6.2	Input-Output Curve Analysis.....	31
Chapter 3	32
3	Results.....	32
3.1	Stratum oriens stimulation excites the basal dendritic CA1 region of hippocampal pyramidal cells.....	32
3.1.1	Baseline input-output relation: abnormal CA1 basal dendritic PPF following stratum oriens TBS in ATRX-KO mice.....	33
3.1.2	Time course analysis: normal CA1 basal dendritic LTP in ATRX-KO mice following stratum oriens TBS	38
3.1.3	Input-output relation two hours post-TBS: E1 LTP at multiple intensities is not affected in ATRX-KO mice.....	42
3.2	MPP stimulation excites the middle molecular layer of DG granular cells.....	46
3.2.1	Baseline input-output relation: The MPP-DG response saturates at lower MPP stimulus intensity in ATRX-KO mice at baseline	47
3.2.2	Time course analysis: ATRX-KO mice display normal MPP-DG synaptic transmission following LTP induction.....	52

3.2.3	Input-output relation two hours post-TBS: DG excitability may be elevated in ATRX-KO mice	56
3.3	MPP stimulation excites the distal apical dendritic CA1 region of hippocampal pyramidal cells	60
3.3.1	Baseline input-output relation: CA1 distal apical dendritic PPF following MPP stimulation is not altered in ATRX-KO mice	62
3.3.2	Time course analysis: Impairment of E1 and E2 distal apical dendritic LTP following MPP TBS in ATRX-KO mice compared to controls	66
3.3.3	Input-output relation two hours post-TBS: ATRX-KO mice exhibit deficits in CA1 distal apical dendritic LTP post-MPP-TBS	70
3.4	MPP stimulation produces long-latency excitation in the proximal apical dendritic CA1 region of hippocampal pyramidal cells	74
3.4.1	Baseline input-output relation: ATRX-KO mice display baseline PPD rather than PPF at high stimulus intensities	76
3.4.2	Time course analysis: ATRX-KO mice are impaired compared to controls in long-latency proximal apical dendritic CA1 LTP following MPP TBS80	
3.4.3	Input-output relation two hours post-TBS: ATRX-KO mice displayed impaired long-latency proximal apical dendritic LTP post-TBS compared to controls.....	84
Chapter 4	88
4	Discussion	88
4.1	<i>In vivo</i> synaptic transmission and LTP in a mouse model of intellectual disability	88
4.2	Synaptic transmission during baseline.....	89
4.2.1	Stratum oriens to basal dendritic CA1	90
4.2.2	MPP to middle molecular layer of DG	90
4.2.3	MPP to distal apical dendritic CA1	91
4.2.4	MPP to CA1 polysynaptic pathway.....	91
4.3	LTP time course analyses	92
4.3.1	Stratum oriens to basal dendritic CA1 LTP and associated control pathway	92

4.3.2	MPP to distal apical dendritic CA1 LTP and associated control pathway	93
4.3.3	MPP to CA1 polysynaptic pathway LTP.....	94
4.4	Relation of electrophysiological measures to structural and behavioural findings in ATRX-KO mice.....	95
4.5	Future Studies	96
	References.....	98
	Curriculum Vitae	113

List of Figures

Fig. 1. Schematic of hippocampal projections and CA1 pyramidal cell layers.....	5
Fig. 2. Schematic illustrating electrode placement.	24
Fig. 3. Representative histological slices showing locations of different hippocampal electrodes.	27
Fig. 4. Schematic illustrating slope and amplitude measurements.	30
Fig. 5. Representative control mouse displaying basal dendritic excitation in CA1 following stratum oriens stimulation.....	33
Fig. 6. Input-output curves of basal dendritic sink during baseline (pre-TBS) following stratum oriens stimulation in control mice.....	35
Fig. 7. Input-output curves of basal dendritic sink during baseline (pre-TBS) following stratum oriens stimulation in ATRX-KO mice.	36
Fig. 8. Trend of decreased basal dendritic PPF following stratum oriens stimulation in ATRX-KO compared to control mice.....	37
Fig. 9. E1 and E2 basal dendritic LTP following stratum oriens TBS in control mice.	39
Fig. 10. E1 and E2 basal dendritic LTP following stratum oriens TBS in ATRX-KO mice.	40
Fig. 11. Normalized basal dendritic E1, E2, and E2/E1 time courses of ATRX-KO mice compared to controls.....	41
Fig. 12. IO2 response for control mice confirmed LTP in the basal dendritic CA1 at different stimulus intensities following stratum oriens TBS.	43
Fig. 13. IO2 response for ATRX-KO mice indicates PPF as well as trend of potentiated E1 and E2 responses compared to IO1.....	44
Fig. 14. No significant difference between control and ATRX-KO mice in E1, E2, or E2/E1 response at 2 hours post-TBS (IO2).....	45

Fig. 15. Representative control mouse displaying excitation of the middle molecular layer of DG following MPP stimulation.	47
Fig. 16. Input-output curves of middle molecular layer of DG sink during baseline (pre-TBS) following MPP stimulation in control mice.....	49
Fig. 17. Input-output curves of middle molecular layer of DG sink during baseline (pre-TBS) following MPP stimulation in ATRX-KO mice.	50
Fig. 18. Altered input-output curves of the MPP to middle molecular layer of DG in ATRX-KO compared to control mice.....	51
Fig. 19. No change in E1, E2, or E2/E1 of the MPP to DG middle molecular layer response following stratum oriens TBS in control mice.....	53
Fig. 20. Significant increase in E1 of MPP to DG middle molecular layer response following stratum oriens TBS in ATRX-KO mice.....	54
Fig. 21. Normalized MPP to DG middle molecular layer E1, E2, and E2/E1 time courses of ATRX-KO mice compared to control mice.....	55
Fig. 22. No PPF or LTP in the MPP to DG middle molecular layer responses following stratum oriens TBS in controls.	57
Fig. 23. IO2 vs. IO1 response for ATRX-KO mice indicates potentiation of E1 and E2 of MPP to middle molecular layer responses.....	58
Fig. 24. Trend of increased E1 and E2 DG middle molecular layer excitability following MPP stimulation 2 hours post-OR-TBS in ATRX-KO mice compared to controls.....	59
Fig. 25. Representative control mouse displaying distal apical dendritic and proximal apical dendritic excitation in CA1 following MPP and stratum radiatum stimuli, respectively.	61
Fig. 26. CA1 distal apical dendritic excitatory sink slopes E1 and E2 following MPP stimulation during baseline (pre-TBS) in control mice.	63

Fig. 27. CA1 distal apical dendritic excitatory sink slopes E1 and E2 following MPP stimulation during baseline (pre-TBS) in ATRX-KO mice.....	64
Fig. 28. No significant differences in CA1 distal apical dendritic responses following MPP stimulation, E1, E2, or E2/E1, during baseline (pre-TBS) between control and ATRX-KO mice.....	65
Fig. 29. E1 and E2 distal apical dendritic LTP following MPP tetanus in control mice.....	67
Fig. 30. E1 and E2 distal dendritic LTP at some time points post-TBS in ATRX-KO mice.	68
Fig. 31. Impaired distal apical dendritic E1 and E2 LTP following MPP TBS in ATRX-KO mice compared to control mice.....	69
Fig. 32. IO2 response for control mice confirmed LTP in the distal apical dendritic CA1 at different stimulus intensities following MPP TBS.	71
Fig. 33. IO2 response for ATRX-KO mice displays trend of potentiated E1 and E2 responses compared to IO1.	72
Fig. 34. No significant differences between control and ATRX-KO mice in E1, E2, or E2/E1 response in IO2.	73
Fig. 35. Representative control mouse displaying long-latency excitation of the proximal apical dendrites of CA1 following MPP stimulation.....	75
Fig. 36. No significant difference in pre-TBS long-latency proximal apical dendritic A1 and A2 response following MPP stimulation in controls.	77
Fig. 37. No significant difference in pre-TBS long-latency proximal apical dendritic A1 and A2 response following MPP stimulation in ATRX-KO mice.	78
Fig. 38. No significant differences in A1, A2, or A2/A1 pre-TBS long-latency proximal apical dendritic responses post-MPP stimulation between control and ATRX-KO mice.....	79
Fig. 39. Time courses of long-latency proximal apical dendritic sinks A1, A2, and A2/A1 following MPP TBS in controls mice.....	81

Fig. 40. Time course of long-latency proximal apical dendritic sinks A1, A2, and A2/A1 following MPP TBS in ATRX-KO mice.....	82
Fig. 41. Impaired long-latency proximal apical dendritic A1 LTP following MPP TBS in ATRX-KO mice compared to controls.	83
Fig. 42. IO2 response for control mice confirmed LTP in the long-latency proximal apical dendritic sink following MPP TBS.....	85
Fig. 43. IO2 response for ATRX-KO mice displayed trend of potentiated A2 long-latency proximal apical dendritic CA1 response following MPP TBS.....	86
Fig. 44. Trend indicating impaired A1 and A2 long-latency proximal apical dendritic response in ATRX-KO mice compared to controls.....	87
Fig. 45. Summary schematic of hippocampal pathway-specific findings.	89

List of Abbreviations

α CaMKII	α -calcium-calmodulin-dependent protein kinase II
A/P	anterior/posterior
A1	excitatory sink amplitude following first pulse of paired-pulses
A2	excitatory sink amplitude following second pulse of paired-pulses
ADD	ATRX-DNMT3A/B-DNMT3L
AEP	average evoked potential
AMPA	α -amino-3-hydroxyl-5-methyl-4-isoxazolepropionic acid
ANOVA	analysis of variance
AP5	2-amino-phosphonopropionic acid
ATR-X	alpha-thalassemia X-linked intellectual disability syndrome
BW	body weight
CA	cornu ammonis
CSD	current source density
DAXX	death domain associated protein
DG	dentate gyrus
DNMT3	de novo methyltransferase 3
E1	excitatory sink slope following first pulse of paired-pulses
E2	excitatory sink slope following second pulse of paired-pulses
EC	entorhinal cortex
emf	electromotive force
EPSP	excitatory postsynaptic potential
GABA	γ -aminobutyric acid
GluR1	glutamate receptor 1
H3K4me0	histone 3 lysine 4 unmethylated
H3K9me2	histone 3 lysine 9 dimethylated
H3K9me3	histone 3 lysine 9 trimethylated
Hb H	hemoglobin H
HFS	high-frequency stimulation
HP1 α	heterochromatin protein 1 α
I/O	input-output
i.p	intraperitoneally

ICR	imprinted control region
ID	intellectual disability
IO1	baseline input-output curve
IO2	input-output curve two hours post-tetanus
IPI	inter-pulse interval
LTD	long-term depression
LTP	long-term potentiation
M/L	medial/lateral
MeCP2	methyl-CpG-binding protein
MF	mossy fibers
MML	middle molecular layer
MPP	medial perforant path
NMDA	N-methyl-D-aspartate
OR	stratum oriens
pEPSP	population excitatory postsynaptic potential
PHD	plant homeodomain
PML	promyelocytic
PPD	paired-pulse depression
PPF	paired-pulse facilitation
PPS	paired-pulse stimulation
RAD	stratum radiatum
REM	rapid-eye-movement
RM	repeated measures
RR	respiratory rate
SEM	standard error of the mean
SLM	stratum lacunosum moleculare
STP	short-term potentiation
SWI/SNF	SWItch/Sucrose Non-Fermentable
T	threshold intensity
TBS	theta-burst stimulation
TDT	Tucker Davis Technology
XCI	X chromosome inactivation

Chapter 1

1 Introduction

1.1 Learning and Memory Literature Review

1.1.1 Discovery of Hippocampal Function

One of the greatest questions in neuroscience, whose answer still eludes us today, aims to investigate the mechanisms underlying learning and the formation and organization of our memories. With sufficient advancements in technology, scientists embarked on a journey to answer this question in the early 1900s. Karl Lashley, whose work has been widely influential in the development of this field, used a variety of lesioning techniques on animal models to investigate the consequences of disrupting cortical networks on learned behaviours (Lashley 1950). After disrupting most of the brain's association areas in animals that had learned complex behaviours, he paradoxically found that those animals were still able to perform those behaviours as well as learn new ones at the same rate as controls (Lashley 1950). Unable to find the memory trace he was looking for, he concluded that memories were distributed diffusely throughout the cortex in a network of hundreds of thousands to millions of neurons (Lashley 1950), but the mechanisms underlying memory formation and distribution were still elusive. In the 1950s, clinicians performed fractional lobotomies of the frontal lobe and even extended the lesion to the anterior hippocampus in some cases to reduce seizure activity in the brains of schizophrenic and epileptic patients. Upon extending these lesions bilaterally to the hippocampus, they noticed severe memory loss (Scoville and Milner 1957). Henry Molaison, famously known as Patient H.M, was one of these individuals who underwent a bilateral medial temporal lobectomy to reduce seizure activity. Following his surgery, he exhibited severe anterograde amnesia—the inability to form new long-term memories post-surgery. Interestingly, he was able to recall vivid memories from his childhood and his procedural memories were still intact (Milner 1962). Since its first anatomical description in the 16th century by Julius Caesar (Bir et al. 2015), the hippocampus had finally been linked to the formation of long-term memories. Over the past several decades, much progress has been made in terms of describing hippocampal structure and function, but as with any scientific pursuit, there are still questions that remain unanswered.

1.1.2 Hippocampal Anatomy

1.1.2.1 Structure

The hippocampus is a structure located in the medial temporal lobe of the human brain, which is composed of several different subregions and cell types. The anatomical organization of the hippocampus in rodents has been described in great detail by Ramón y Cajal and Lorente de Nó using Golgi staining (Ramón y Cajal 1911; Lorente de Nó 1934). The hippocampus is composed of the hippocampus proper, the dentate gyrus (DG), the subicular complex, as well as the entorhinal cortex (EC) (Amaral and Witter 1989; Insausti 1993). The hippocampus proper is further subdivided into cornu ammonis (CA) subregions including CA1, CA2, and CA3 (Glees and Griffith 1952). Similarly, the subicular complex is subdivided into the subiculum, presubiculum, and parasubiculum (Amaral and Witter 1989). Finally, the EC in rodents was described as having medial and lateral subdivisions (Amaral and Witter 1989).

The principal cell type of the hippocampus proper is the pyramidal neuron. These cells have a triangular cell body located in the stratum pyramidale cell layer, which spans approximately 50–100 μm . In the CA1 region of the hippocampus, pyramidal neurons project basal dendrites above the cell body into the stratum oriens (OR) cell layer. Conversely, they project apical dendrites in the opposite direction into the stratum radiatum (RAD) and stratum lacunosum moleculare (SLM) cell layers, corresponding to the proximal and distal apical dendrites, respectively (Knowles 1992). Below the SLM lies the hippocampal fissure, which separates the SLM of CA1 from the dendritic tree of the granular cells in the DG (Amaral and Witter 1989). The organization of the CA3 pyramidal cell layers is altered compared to that of CA1 pyramidal neurons, specifically with the characterization of the stratum lucidum cell layer between the cell body and RAD (Knowles 1992). The stratum lucidum can be distinguished morphologically from the other cell layers because it features thorny excrescences, which synapse with mossy fibers from the DG (Andersen et al. 2007). Finally, the CA3 region is further subdivided into the functionally-unique ordered subregions CA3a, CA3b, and CA3c. These regions differ in their projections to the CA1 regions and are organized such that CA3a is located distal to the DG whereas CA3c is located proximal to the DG (Lorente de Nó 1934).

The DG is located underneath the CA1 region of the hippocampus and it forms a V-shape around the adjacent hippocampus proper. The suprapyramidal blade of the DG is located above the pyramidal cell layer of the adjacent hippocampus proper, while the infrapyramidal blade is

located below (Amaral and Witter 1989). The principal cell type of the DG is the granular cell, which is located in the granular cell layer. These cells project dendrites upward into the molecular layer of the DG, which lies just below the hippocampal fissure. The polymorphic cell layer, also known as the dentate hilus, is located below the granular cell layer (Knowles, 1992). The hilus is occupied by a variety of interneurons, varying in shape, size, and location, as well as mossy fiber collaterals that pass from the EC through to the trisynaptic circuit—one of the major hippocampal synaptic pathways (Andersen et al. 2007).

1.1.2.2 Circuitry

The structures described above are widely interconnected to give rise to physiologically relevant hippocampal synaptic pathways. The major source of input into the hippocampus comes from EC layer II and III neurons and information propagates unidirectionally to the CA1 region and subiculum, which serve as major hippocampal outputs back to the cortex (Amaral and Witter 1989). Layer II of EC projects to the molecular layer of DG as well as the CA3 region of the hippocampus, leading to excitation of the trisynaptic circuit. The trisynaptic circuit features EC projections to DG via the perforant path, DG projections to CA3 via mossy fibers, CA3 projections to basal and apical dendrites of CA1 via Schaffer collaterals, and CA1 output from the hippocampus (Amaral and Witter 1989) (Fig. 1A). The basal dendrites of CA1 are more numerous than the apical dendrites (Ramón y Cajal 1911; Lorente de Nó 1934; Blackstad 1958), which could explain why the CA3 to basal dendritic CA1 projection is more robust than the apical dendritic projection (Capocchi et al. 1992). Studies have also identified a commissural pathway projecting from CA3 of one hemisphere to the CA1 region of the contralateral hemisphere (Gottlieb and Cowan 1973; Amaral and Witter 1989). Furthermore, the CA3 fibers have been shown to backpropagate to the DG, with more collaterals being projected from CA3 neurons proximal to DG than those distal to it (Ishizuka et al. 1990; Li et al. 1994). As a result, the CA3 region has been identified as a key projection area in the hippocampus resulting in widespread activation of different regions as well as the generation of reverberating networks (Ishizuka et al. 1990; Li et al. 1994) that may play a role in hippocampal function. Whereas layer II of EC activates the hippocampal trisynaptic circuit, layer III of EC projects monosynaptically

to the distal apical dendrites of the CA1 region via the temporoammonic pathway (Amaral and Witter 1989).

1.1.3 Hippocampal Neurotransmission

The hippocampus is made up of several different cell types, including principal cells—pyramidal neurons and granular cells—as well as interneurons. Investigation of the hippocampal perforant path has indicated that the synapses formed between principal cells are excitatory and feature glutamatergic neurotransmission (White et al. 1977; Colbert and Levy 1992). Following stimulation of these excitatory synaptic pathways, depolarization occurs, resulting in the influx of Na^+ into the axon. The increase in membrane potential causes voltage-gated Ca^{2+} channels on the presynaptic membrane to open, resulting in the rapid influx of Ca^{2+} into the presynaptic axon terminal. The influx of Ca^{2+} causes the release of presynaptic vesicles containing the neurotransmitter glutamate. Glutamate binds to postsynaptic α -amino-3-hydroxyl-5-methyl-4-isoxazolepropionic acid (AMPA) and N-methyl-D-aspartate (NMDA) receptors, resulting in depolarization of the postsynaptic neuron and the activation of downstream cascades. The administration of glutamate analogues was found to compete with endogenous glutamate at these synapses (White et al. 1977), and glutamate receptor antagonists were found to abolish the population excitatory postsynaptic potential (pEPSP) generated following stimulation of the temporoammonic pathway (Colbert and Levy 1992). In contrast to the principal cells, various types of interneurons in the hippocampus use γ -aminobutyric acid (GABA), an inhibitory neurotransmitter, to temporally regulate the activity of the excitatory synapses (Freund and Buzsaki 1996). Examples of these interneurons include basket cells, chandelier cells, and bistratified cells, and they each differ in their localization to specific cell layers of the hippocampus, as well as their size and shape (Freund and Buzsaki 1996). Although inhibitory interneurons only comprise approximately 10–15% of the hippocampal neuronal population, their physiological diversity allows them to efficiently regulate hippocampal synaptic pathway function (Pelkey et al. 2017).

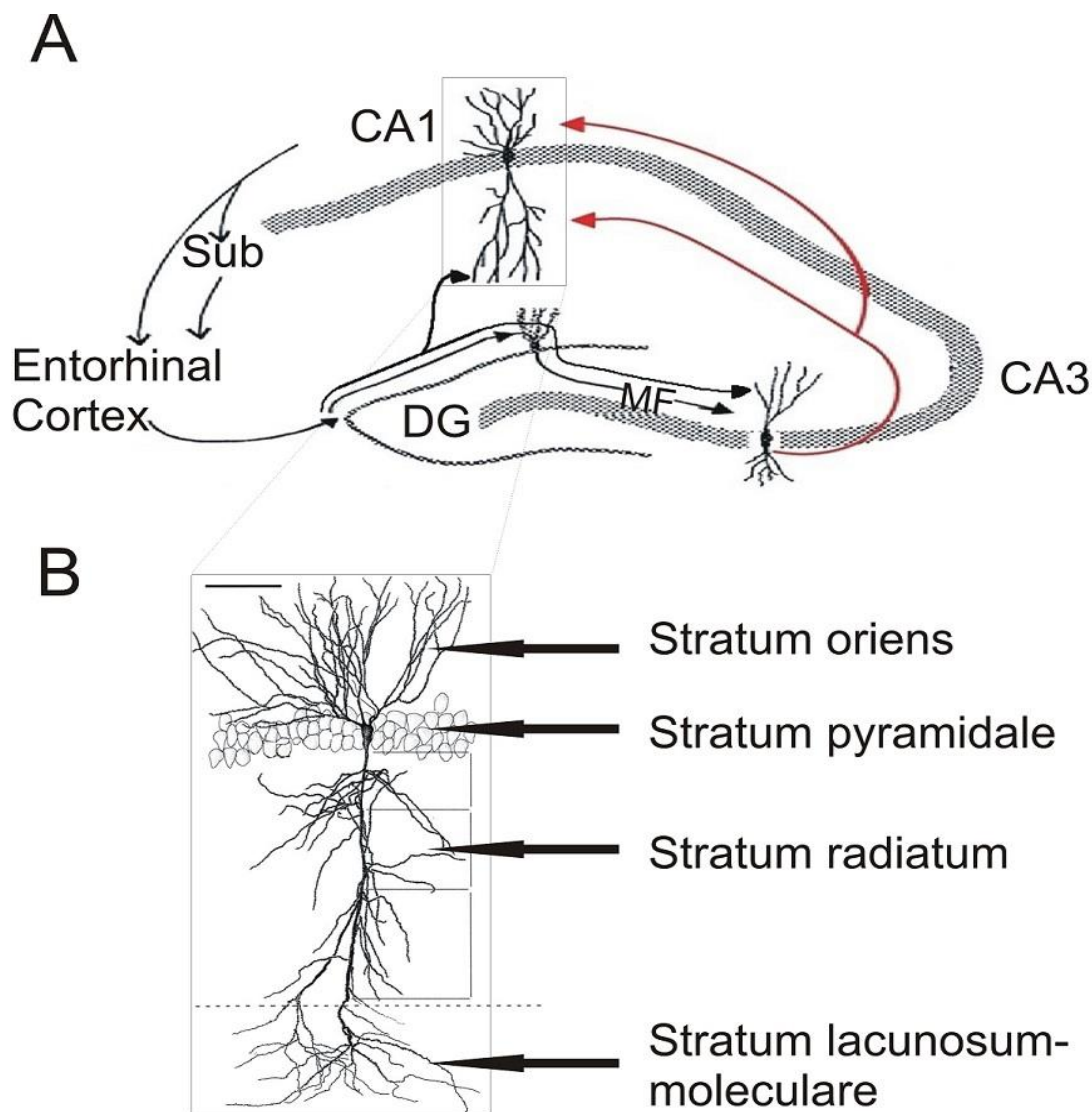


Fig. 1. Schematic of hippocampal projections and CA1 pyramidal cell layers.

A) Coronal section of rat hippocampus illustrating hippocampal structure and circuitry. Arrows indicate the direction of information propagation. Information projects from the entorhinal cortex (EC) to the dentate gyrus (DG) through the perforant path, from the DG to the CA3 via the mossy fibers (MF), and from the CA3 to CA1 via the Schaffer collaterals. The CA1 outputs information back to EC (originally illustrated by L. Stan Leung; permission obtained for use) **B)** Magnification of a CA1 pyramidal neuron with cell layers labeled. The basal dendrites project to the stratum oriens, whereas the proximal and distal apical dendrites project to the stratum radiatum and the stratum lacunosum moleculare, respectively (originally illustrated by Megias et al. 2001).

1.1.4 Hippocampal Function

The hippocampus contributes directly to a subset of long-term memory known as declarative memory. Declarative memory is a type of explicit (conscious) memory that is either episodic or semantic in nature. Episodic memories refer to vivid recollections of past events, with detailed descriptions of who was involved as well as what happened and where it took place. Semantic memories, on the other hand, refer to factual knowledge that is accumulated over time and can be consciously recalled. Declarative memories differ from procedural memories, which are implicit (unconscious) recollections of skilled behaviour. Whereas declarative memories can be formed in as little as one trial, procedural memories are developed over long periods of time through repetition (Nakashiba et al. 2008).

The hippocampus has been linked to memory formation through clinical studies investigating lesions to the medial temporal lobe which have resulted in anterograde amnesia, one such example of this being Patient H.M. However, in the case of Patient H.M, it must be noted that structures immediately surrounding the hippocampus were also removed during the surgery (Milner 1962), which may have confounded interpretations made at the time (Squire and Zola-Morgan 2011). Follow-up studies that performed hippocampal lesions on animals did not display the same drastic consequences seen in Patient H.M, however, a lesion of the hippocampus in combination with the amygdaloid body did (Mishkin 1978). Eventually, evidence was gathered from a human patient with a hippocampal CA1 lesion who exhibited similar memory impairments as Patient H.M, supporting the role of the hippocampus in the formation of declarative memories (Zola-Morgan et al. 1986).

The role of the hippocampus has been widely studied in animals using various invasive techniques aimed to unravel the underlying mechanisms responsible for learning and memory. In rodents, behavioural and electrophysiological experiments supported the role of the hippocampus in spatial learning and memory, however, there is yet to be a consensus on the specific function of each hippocampal synaptic pathway in the formation of declarative memories. For instance, although the trisynaptic circuit projects through every major synapse in the hippocampus, inactivating the trisynaptic circuit while preserving the temporoammonic pathway—monosynaptic EC projection to CA1—still resulted in spatial learning (Nakashiba et al. 2008). Although the temporoammonic pathway was sufficient for spatial learning to take place, it was found that the trisynaptic circuit was important for rapid one-trial contextual

learning in mice as well as the spatial tuning of CA1 cells (Nakashiba et al. 2008). Further investigations of the temporoammonic pathway have suggested a role in long-term spatial memory recollection, with the CA3 to CA1 circuitry being necessary for recall (Brun et al. 2002; Brun et al. 2008). Specific regions of the hippocampus have also been found to play certain roles in learning and memory. For instance, whereas the CA3 to CA1 synapses are important for spatial memory (Leung and Shen 1995), the CA2 region of the hippocampus has been implicated in social memory (Hitti and Siegelbaum 2014). Finally, investigations using computer models of hippocampal microcircuitry to investigate learning and memory have concluded that hippocampal oscillatory activity as well as GABA-mediated inhibition play a major role in memory recall (Cutsuridis et al. 2010). Overall, it appears that hippocampus-mediated formation of declarative memories likely involves several subregions and synaptic pathways working collaboratively, as there is much overlap between the functional significance of each pathway.

1.1.5 Synaptic Plasticity

Synaptic plasticity refers to our brain's ability to modify the associative strengths of its synapses in real-time to optimize neural networks for certain functions. In other words, our ability to learn and adapt in everyday life stems from the constant alteration of our synapses in response to our experiences. This line of thinking was first proposed in 1949, when Donald Hebb suggested that learning and memory were complex behaviours that could be simplified down to changes in synaptic plasticity. In agreement with Karl Lashley's theories of the memory trace at the time, Hebb proposed that memories existed within the synapses between neurons, with learning being the modification of these synapses. He further proposed the famous phrase, "cells that fire together wire together" as a model for the association of neurons into cooperative neural networks. According to the theory, which is still widely accepted today, simultaneous activation of neurons in response to an event results in the formation of stronger synapses between those neurons and weaker synapses with neurons that have non-synchronous firing. In this way, our brains constantly modulate our neural networks, strengthening synapses we use frequently and weakening synapses that are less important. Importantly, these modulations in synaptic strength represent a global brain phenomenon and are not simply restricted to the hippocampus.

1.1.5.1 Long-Term Potentiation

Long-term potentiation (LTP) is the long-lasting increase in the size of an excitatory postsynaptic potential (EPSP) following repetitive activation of excitatory synapses, and it is thought to be the cellular mechanism underlying learning and memory (Bliss and Lømo 1973; Bliss and Collingridge 1993). The opposite phenomenon, long-term depression (LTD), is a long-lasting decrease in the size of an EPSP due to low-frequency activation of excitatory synapses (Dudek and Bear 1995). Recently, LTP and LTD were shown to have a causal link with the reactivation and inactivation of associative memories, respectively (Nabavi et al. 2014), establishing their role as cellular correlates of learning and memory. LTP can be induced in the hippocampal synapses via a high-frequency stimulation (HFS) or a theta-burst stimulation (TBS). Whereas HFS involves stimulating synapses 50 or more times at high frequencies, usually 100–200 Hz, TBS involves stimulation at the physiologically relevant theta rhythm, which is the hippocampal rhythmic oscillatory activity present during active spatial exploratory behaviours as well as during rapid-eye-movement (REM) sleep (Leung 1998). Interestingly, it has been found that HFS is better than TBS at eliciting apical dendritic LTP at the CA3 to CA1 Schaffer collateral synapse, however, both types of tetanic stimulation perform similarly in terms of basal dendritic LTP induction (Leung and Shen 1995). With regards to the temporoammonic pathway, previous studies by our lab have demonstrated that TBS of the perforant path reliably induces LTP in the distal apical dendritic CA1 region.

The mechanisms underlying LTP in hippocampal synapses have been investigated and classified into two categories: NMDA-receptor-dependent and NMDA-receptor-independent. The NMDA receptor is located on the postsynaptic membrane and features a glutamate binding pocket as well as a non-selective cation channel, which is initially blocked by a Mg^{2+} ion when the postsynaptic neuron is at resting membrane potential. Therefore, to activate the NMDA receptor, two events must take place simultaneously: sufficient depolarization of the postsynaptic membrane to cause Mg^{2+} to dissociate from the NMDA ion channel, and binding of glutamate to the NMDA receptor. Activation of the NMDA receptor allows influx of extracellular Na^+ and Ca^{2+} ions into the postsynaptic neuron and efflux of intracellular K^+ ions. It is thought that transient NMDA-receptor-mediated Ca^{2+} entry into the postsynaptic neuron is crucial for LTP induction largely due to the interaction of Ca^{2+} and α -calcium-calmodulin-dependent protein kinase II (α CaMKII) (Miyamoto and Fukunaga 1996). Upon Ca^{2+} binding, α CaMKII undergoes rapid

autophosphorylation of Thr286 (Soderling and Derkach 2000), becoming constitutively active even in the absence of Ca^{2+} . αCaMKII then phosphorylates many intracellular targets including glutamate receptor 1 (GluR1), a subunit of the AMPA receptor, causing an increase in single-channel conductance of AMPA receptors on the postsynaptic membrane (Benke et al. 1998; Malenka and Bear 2004). Inhibiting GluR1 function or deleting expression of αCaMKII has been shown to inhibit LTP whereas increasing the presence of AMPA receptors on the postsynaptic membrane was shown to induce LTP (Malinow and Malenka 2002; Song and Huganir 2002; Malenka and Bear 2004). Because αCaMKII can remain activated in the absence of Ca^{2+} , this protein is thought to be an important mediator of learning and memory processes (Shonesy et al. 2014). On the other hand, NMDA-receptor-independent LTP works through similar downstream mechanisms which involve the activation of αCaMKII , however, Ca^{2+} influx into the postsynaptic neuron occurs via voltage-gated Ca^{2+} channels (Johnston et al. 1992; Johnston and Wu 1994) located on the postsynaptic membrane. In both cases, it appears that Ca^{2+} influx into the postsynaptic neuron is essential for LTP induction and blocking Ca^{2+} entry using various techniques resulted in loss of LTP at hippocampal synapses.

LTP can be described in terms of four key properties: temporal persistence, associativity, cooperativity, and input-specificity. Temporal persistence refers to the long-lasting increase in the magnitude of an EPSP following tetanic stimulation. LTP is associative in the sense that weak synapses can be strengthened by co-tetanizing them with stronger synapses that are more likely to potentiate following tetanus (Wigström and Gustafsson 1986). The cooperativity of LTP has been shown by larger LTP induction at target synapses following tetanus of a larger number of afferent fibers projecting to those synapses (Wigström and Gustafsson 1986). Finally, LTP is input-specific because only the synapses that are tetanized have been shown to potentiate. With regards to temporal persistence, LTP—which normally persists for a minimum of 30–60 minutes post-tetanus—can be classified into three categories based on differences in longevity: LTP1, LTP2, and LTP3 (Abraham and Otani 1991). LTP1 is the shortest form of LTP, only lasting approximately 2.5 hours post-tetanus until the EPSP returns to baseline levels (Abraham 2003). LTP1 features activation of the NMDA receptor in addition to ryanodine receptor-mediated Ca^{2+} release, however, there are not yet changes in protein expression or gene expression. LTP2 is a longer-lasting form of LTP, found to persist approximately 3.5 days post-tetanus (Abraham 2003). LTP2 differs from LTP1 because it features changes in protein synthesis, but it does not

display any modifications in gene expression. Finally, LTP3 is the longest-lasting form of LTP, which persists up to 20.3 days (Abraham 2003) and involves changes to protein synthesis as well as gene expression. LTP3 relies on extracellular Ca^{2+} entry into the postsynaptic neuron whereas LTP1 and LTP2 rely solely on intracellular Ca^{2+} stores to activate downstream cellular pathways. As a result, the source of Ca^{2+} utilized by the postsynaptic neuron may play a role in determining the temporal persistence of LTP (Raymond, 2007).

1.1.5.2 Paired-Pulse Facilitation

Whereas LTP is a long-lasting increase in the size of an EPSP, paired-pulse facilitation (PPF) is a form of short-term potentiation (STP), occurring on the scale of milliseconds. PPF is defined as an increase in the response following the second pulse of a paired-pulse stimulation (PPS) relative to the response following the first pulse just milliseconds prior. If the second response is lower than the first response, this is known as paired-pulse depression (PPD). PPS is commonly used as the stimulation protocol in animal studies investigating PPF and LTP because it simulates the burst-firing of action potentials in neurons, which is a physiologically relevant process.

It is commonly thought that PPF occurs because of leftover Ca^{2+} in the synapse following the first pulse, which enters the presynaptic axon terminal at the second pulse, resulting in increased release of neurotransmitter into the synaptic cleft and increased EPSP. Studies have found a positive correlation between the quantification of presynaptic intracellular Ca^{2+} levels and the extent of PPF achieved (Wu and Saggau 1994). There is, however, evidence that PPF may also follow postsynaptic mechanisms (Bagal et al. 2005).

Whether PPF and LTP are related in any way is still unknown, and the literature on this topic remains controversial. Some studies indicate that an inverse relationship between LTP and PPF exists following LTP induction (Schulz et al. 1994), whereas others concluded that there is no correlation between the two (Manabe et al. 1993). In both cases, however, it appears that Ca^{2+} signaling plays a crucial role. Previous studies in our lab have shown that LTP induction in the temporoammonic pathway correlates with reduced PPF levels at those synapses (Vu et al. unpublished). Taken together, it appears that both pre- and postsynaptic mechanisms likely contribute to LTP and PPF, but more research is required to elucidate the specific relationship between LTP induction and degree of PPF.

1.2 Intellectual Disability Literature Review

1.2.1 Intellectual Disability

1.2.1.1 General Introduction

Disorders causing intellectual disability (ID) have been documented for many years in scientific literature, but only more recently through advances in technology and methodology have we been able to delve deeper into mechanisms underlying their causes. In 1996, the World Health Organization defined ID as a condition resulting in significant impairment in intellectual capabilities and adaptive behaviour. In general, these disorders have been categorized into two groups: syndromic—associated with defects in other organs and often including facial gestalt—or non-syndromic—cognitive impairment that is isolated from other abnormalities. In both cases, ID disorders feature significant cognitive impairments. Approximately 75–90% of all cases of ID feature mild cognitive deficit, with IQ ranging from 50–69. 10–25% of ID cases feature either moderate, severe, or profound cognitive impairment, with IQ ranging from 35–49, 20–34, or less than 20, respectively (Daily et al. 2000). Whereas individuals with mild ID can eventually learn to lead mostly independent lives, those with more severe forms of ID are often unable to perform even basic processes like self-care, meaning they will likely require professional assistance to survive (Daily et al. 2000). Mortality of individuals with severe or profound forms of ID is also significantly higher compared to the general population, whereas those with mild ID show no difference (Similä et al. 1987; Patja et al. 2000). Because of the prevalence of ID and the continual identification of ID-related-genes in scientific literature, further research must be done to shed light on regulatory mechanisms during development and potential therapeutic targets.

1.2.1.2 ID Disorders

Over 150 disorders have been identified that feature an ID component and an isolated X-linked trait, which is often accompanied by somatic, neuromuscular, metabolic, or behavioural abnormalities (Stevenson et al. 2012; des Portes 2013). It is estimated that X-linked ID disorders affect 1–2% of the general population, with a larger proportion of individuals from developing/low-income countries being affected than those from developed/high-income countries (Durkin 2002; Maulik et al. 2011). Like many other disorders, the ID phenotype can be produced due to genetic predisposition as well as environmental factors. Many ID disorders

also share similarities in terms of not only phenotype but also disorder progression, indicating that perhaps similar mechanisms play a role in their development. For example, some of the most well-studied ID disorders are known to feature spontaneous seizure activity within the brain, including Juberg-Marsidi, Smith-Fineman-Myers, Coffin-Lowry, and ATR-X syndromes (Stevenson et al. 2012). Over the years, etiological diagnosis in a clinical setting has improved drastically due to the introduction of genomic screening methods for rare disorders featuring an ID component, but there is still much progress to be made as we move forward (Kvarnung and Nordgren 2017).

1.2.2 ATR-X Syndrome

1.2.2.1 Discovery

α -thalassemia X-linked intellectual disability (ATR-X) syndrome was initially characterized in the late 1900s when Weatherall and colleagues observed three Northern European families who had sons that presented with severe cognitive deficits and ID paired with α -thalassemia—a reduction in the production of hemoglobin. Specifically, the patients were described as having increased hemoglobin H inclusions (Hb H) in their erythrocytes, caused by decreased expression of the α -globin gene cluster—responsible for producing α -globin, a subunit of hemoglobin (Weatherall et al. 1981). This decrease in expression was due to transcriptional downregulation of the α -globin gene, producing less mRNA (Weatherall et al. 1981). Up until that point, hemoglobin H disorders resulting in α -thalassemia have been identified but never associated with an ID phenotype. Over the following few years, Higgs and colleagues discovered several more ID patients that displayed the same α -thalassemia phenotype (Higgs et al. 1989). Eventually, a cohort of 13 patients was established and it was found that 8 of them had mutations near the tip of chromosome 16, corresponding specifically to the location of the α -globin gene cluster. The remaining 5 patients, however, were not found to have any mutations on chromosome 16, but still had the characteristic traits of severe ID, facial and genital abnormalities, as well as a mild form of hemoglobin H disease (Wilkie et al. 1991). This led researchers to question whether another mechanism was responsible for the ID phenotype and downregulation of the α -globin gene cluster. Nevertheless, because the non-deletion form of the ID syndrome did not feature

male to male transmission, it was classified as an X-linked ID syndrome and eventually named ATR-X syndrome (Gibbons et al. 1991).

1.2.2.2 Clinical Studies

ATR-X syndrome is a rare congenital X-linked ID syndrome associated with moderate to profound cognitive impairment, severe expressive language disorder, developmental delay, facial abnormalities—facial dysmorphism, hypotonia, hypertelorism, upturned nose with anteverted nares, and epicanthic folds of the eyelid—, genital abnormalities, and in some cases, α -thalassemia (Weatherall et al. 1981; Gibbons et al. 1995; Villard et al. 1996; Gibbons 2006; Stevenson 2014). It is estimated that ATR-X syndrome affects < 1–9/1,000,000 individuals in the general population (Gibbons 2006). In approximately one third of the cases, patients are prone to clonic/tonic or myoclonic seizures (Gibbons and Higgs 2000; Gibbons 2006). Before more modern techniques arose, diagnosis of ATR-X syndrome was often established by a positive test result for presence of Hb H inclusions in the blood (Gibbons 2006), although some ATR-X patients featured a mild hematological phenotype, making diagnosis more difficult (Logie et al. 1994). More recently, it was discovered that ATR-X patients have a characteristic epigenetic signature associated with hypermethylation at pericentromeric and telomeric regions in DNA which can be used as a biomarker to aid diagnosis (Schenkel et al. 2017). No treatment is currently available for ATR-X syndrome, but studies are continuing to identify potential therapeutic targets to one day treat the disease.

ATR-X syndrome is caused by mutations in *ATRX*, a gene coding for an ATP-dependent chromatin-remodeling protein. Through gene linkage analysis, the locus encoding *ATRX* was estimated to be between Xq12–Xq21.31 (Gibbons et al. 1992), and later refined to Xq13.3 (Gecz et al. 1994; Stayton et al. 1994; Gibbons et al. 1995), which corresponded to a gene known then as *XH2*. Over 70 different human mutations in *ATRX* have been summarized, the most common one being the missense R236C amino acid change (Villard and Fontes 2002), and with most mutations affecting the zinc finger and helicase domains of the gene (Gibbons and Higgs 2000). ATR-X syndrome commonly affects only males, as females with a mutation on one X chromosome display highly skewed X-inactivation of the affected chromosome (Gibbons et al. 1995; Wada et al. 2005). Interestingly, females can exhibit the complete phenotype of affected

males if they preferentially inactivate the unaffected X chromosome (Badens et al. 2006), or if non-skewed X-inactivation takes place (Wada et al. 2005).

1.2.3 *ATRX* Gene and Protein

1.2.3.1 Structure of *ATRX* and Gene Product

ATRX is a gene spanning over 300 kb which contains 36 exons (Picketts et al. 1996). Structural analysis of the gene revealed two highly conserved domains located near the N- and C-termini of the gene product, which are both commonly mutated in ATR-X syndrome. The *ATRX* gene product can be broadly categorized into three regions: a largely hydrophilic segment near the N-terminal, an alternating hydrophilic and hydrophobic middle segment, and the C-terminal domain (Picketts et al. 1996). The N-terminal end of the protein forms a globular domain that shares sequence homology to the de novo methyltransferase 3 (DNMT3) family of DNA methyltransferases (Argentaro et al. 2007). This domain is known as the ATRX-DNMT3A/B-DNMT3L (ADD) domain (Xie et al. 1999; Aapola et al. 2000). Mutations in this domain can affect surface amino acids or ones that are buried in the globular protein to affect both intrinsic function as well as binding with intracellular proteins (Argentaro et al. 2007). Missense mutations in this domain have been found to significantly alter the backbone dynamics of the binding pocket, leading to ATRX dysfunction and the development of ATR-X syndrome (Palaniappan and Ramalingam 2017). In addition, mutations in the plant homeodomain (PHD) domain have been associated with permanent psychomotor deficiencies as well as urogenital abnormalities (Badens et al. 2006). The C-terminal end of ATRX contains 7 collinear domains that share homology with the SWItch/Sucrose Non-Fermentable (SWI/SNF) family of DNA-dependent ATPases (Picketts et al. 1996). Mutations in the C-terminal end have been described as less severe than those of the PHD domain (Badens et al. 2006). The very C-terminus of ATRX contains two more domains which contain multiple glutamine residues (Picketts et al. 1998), and patient mutations in the C-terminal end have been shown to interfere with ATRX localization to promyelocytic (PML) nuclear bodies (Bérubé et al. 2008). Nonsense mutations in the C-terminal end of ATRX result in a truncated protein which reduces or eliminates ATPase functionality. Interestingly, one truncated form of ATRX, known as ATRXt, has been discovered (McDowell

et al. 1999; Bérubé et al. 2000) and it is thought to play an important biological role (Garrick et al. 2004).

1.2.3.2 Function of ATRX

The ATRX protein can mediate its function solely through the intrinsic activity of its conserved domains as well as through its various interactions with binding partners. The ADD domain gives ATRX the ability to bind to histone tails with a specific epigenetic signature. Specifically, two binding pockets in the ADD domain simultaneously recognize unmethylated histone 3 lysine 4 (H3K4me0) as well as di- or tri-methylated histone 3 lysine 9 (H3K9me2 and H3K9me3, respectively) (Dhalayan et al. 2011; Eustermann et al. 2011; Iwase et al. 2011). The ADD domain therefore acts as a histone-reader, enabling ATRX to localize to heterochromatic regions of DNA. This localization to heterochromatin is enhanced through the direct interaction of ATRX with heterochromatin protein 1 α (HP1 α) (McDowell et al. 1999) and is further stabilized by interactions with methyl-CpG-binding protein (MeCP2) (Dhalayan et al. 2011). The interaction of ATRX with heterochromatin is not dependent, however, on the presence of MeCP2 except for in brain tissue, where dependency seems to be altered (Nan et al. 2007). Once localized to heterochromatin, ATRX can use its SWI/SNF ATPase activity to modify the entry site of nucleosomes and translocate across double-stranded DNA (Xue et al. 2003) in a similar fashion to other ATP-dependent DNA translocases like RSC and Sth1 (Saha et al. 2002). ATRX can also bind directly to death domain associated protein (DAXX) (Tang et al. 2004), which is a multi-functional protein found in PML nuclear bodies (Torii et al. 1999; Ishov et al. 1999). Traditionally, DAXX has been regarded as a pro-apoptotic molecule which binds to Fas death domain to induce cellular apoptosis (Yang et al. 1997). More recently, ATRX-DAXX direct interaction has been found to create a chromatin-remodeling complex involved in transcriptional regulation (Tang et al. 2004). DAXX has been shown to specifically bind histone variant H3.3, and together, the ATRX-DAXX-H3.3 complex can deposit H3.3 at pericentromeric and telomeric heterochromatin in a replication-independent manner (Lewis et al. 2010). The ATRX-mediated deposition of H3.3 has also been found to occur within coding regions of GC-rich genes to resolve G quadruplexes and facilitate transcriptional elongation (Levy et al. 2014). Apart from its interactions with DAXX, ATRX can also directly bind to EZH2, a chromatin-associated

protein (Cardoso et al. 1998), and macroH2A histone variants (Ratnakumar et al. 2012). In addition, it has been discovered that ATRX plays a role in maintaining the epigenetic silencing of imprinted genes. For instance, ATRX along with its binding partners cohesin and MeCP2 localizes to the maternal *H19* imprinted control region (ICR) to regulate *H19* gene expression and potentially expression of the neighboring *Igf2* gene (Kernohan et al. 2010). More recently, it has been found that the ATRX-DAXX-H3.3 complex can recognize H3K9me3 signatures in imprinted genes and maintain repression through epigenetic silencing (Voon et al. 2015).

1.2.3.3 Conditional inactivation of *Atrx* in the mouse CNS

Animal studies have given us insight into the effects of altered ATRX expression on normal cellular function as well as disease progression. One study examining global loss of ATRX in male mouse embryos at the 8–16 cell stage observed embryonic lethality due to an inability to form the secondary trophoblast, likely resulting in nutritional deficit for the developing embryo (Garrick et al. 2006). To bypass embryonic lethality, a cre/loxP system was used to delete exon 18 of *Atrx*, equivalent to a null mutation, under control of the FoxG1 promoter, which is activated at E8 or E9 during embryonic development (Bérubé et al. 2005). Male mice were found to have cortical hypocellularity as well as significant disorganization of proliferative neuroepithelium and a loss of the DG (Bérubé et al. 2005). Affected male mice were smaller than littermate controls and most of the mice died 24–48 hours after birth, with one surviving for 24 days with progressively worsening condition (Bérubé et al. 2005). Additionally, ATRX deficiency in the developing forebrain has been shown to result in increased p53-dependent neuronal apoptosis within the dentate neuroepithelium, which was partially rescued by p53 double knockout (Seah et al. 2008). Accumulation of replicative DNA damage is known to occur upon loss of *Atrx* likely due to an accumulation of G quadruplexes in DNA, and this is thought to initiate a DNA damage response (Watson et al. 2013).

1.2.4 Role of ATRX in Learning & Memory

Dysregulation of ATRX has also been related to impairments in learning and memory. Mice with deletion of exon 2 of ATRX and reduced ATRX expression exhibited hippocampal LTP impairments in the CA3 to proximal apical dendritic CA1 Schaffer collateral pathway associated

with a reduction in autophosphorylation of α CaMKII and subsequent phosphorylation of GluR1 subunits (Nogami et al. 2011). These mice also performed worse than controls on contextual fear conditioning, indicating impairments in hippocampus-dependent memory (Nogami et al. 2011). Recent work by our group used a cre/loxP system to conditionally inactivate *ATRX* specifically in postnatal forebrain excitatory neurons, expressing Cre recombinase under the control of the *CaMKII* promoter (Tamming et al. unpublished) to investigate *ATRX* function in the normally developed mouse brain. While these mice displayed normal short-term and working memory, they featured long-term spatial memory impairments in the Morris water maze and contextual fear conditioning, and displayed learning defects in the paired-associate learning operant task (Tamming et al. unpublished). Furthermore, imaging of the hippocampi of these mice revealed normal CA1 proximal apical dendritic branching, but a reduced number of presynaptic vesicles, a wider synaptic cleft, and a larger postsynaptic density (Tamming et al. unpublished).

1.3 Rationale and Aims

1.3.1 Rationale

The role of *ATRX* as a chromatin-remodeling protein involved in histone deposition, transcriptional elongation, gene expression, and cell cycle regulation in the developing and postnatal stage has been established. Loss- and gain-of-function studies have determined that proper *ATRX* expression levels are required for normal development in a variety of tissues. Mouse models of ID have determined that reduced expression of *ATRX* during development resulted in impaired hippocampal spatial learning and memory. Furthermore, postnatal inactivation of *ATRX* in forebrain pyramidal neurons resulted in ultrastructural defects in the hippocampus. While it is evident that *ATRX* plays a crucial role in proper hippocampal function, the hippocampal synaptic pathways that are affected, and the cellular mechanisms underlying these deficits are unknown. The purpose of our study was to investigate major hippocampal synaptic pathways using electrophysiological techniques to provide insight into the causes of long-term spatial memory impairment in mice with postnatal conditional ablation of *ATRX*. We hypothesized that postnatal conditional ablation of *ATRX* will disrupt hippocampal synaptic transmission and plasticity. To test our hypothesis, we proposed two aims.

1.3.2 Aims

1.3.2.1 Aim 1

Our first aim was to establish baseline measures of hippocampal synaptic transmission in two major synaptic pathways using input-output curves. The two pathways we chose to investigate were the CA1/CA3 stratum oriens to CA1 basal dendritic cell layer as well as the MPP to distal apical dendritic CA1 region. Each pathway was investigated separately in control and knockout mice using a series of increasing stimulus intensities (as a function of pathway-specific threshold) to reveal any differences in properties of synaptic transmission which may be present at baseline, before LTP induction. Alongside the investigation of the two pathways mentioned above, corresponding control pathways will also be measured at baseline for differences in properties of synaptic transmission between control and knockout mice.

1.3.2.2 Aim 2

Our second aim was to test hippocampal LTP in each pathway. The hippocampal synaptic pathways mentioned above were tetanized using a theta-burst stimulation (TBS) to induce LTP in the corresponding synapse in CA1. Responses were recorded in 5-minute intervals to produce a time course analysis, where LTP will be indicated by a long-lasting increase in response post-TBS.

Chapter 2

2 Materials and Methods

2.1 Animal Husbandry/Genotyping

All procedures involving animals were conducted in accordance with the regulations of the Animals for Research Act of the province of Ontario and approved by the University of Western Ontario Animal Care and Use Committee. Mice lacking ATRX expression specifically in postnatal excitatory neurons of the forebrain were generated by mating *Atrx* loxP mice (Bérubé et al. 2005) and CaMKIICre mice (Tsien et al. 1996). Male progeny with the genotype *Atrx*^{f/y}-cre⁺ are referred in this thesis as ATRX-KO while male progeny with genotype *Atrx*^{f/y}-cre⁻ were used as controls. Experiments were only performed on male offspring as ATRX-KO female mice did not feature the long-term spatial memory deficits observed in males (Tamming et al. unpublished). Male ATRX-KO mice feature complete loss of ATRX protein expression specifically in differentiated excitatory neurons of the forebrain. Control mice contain the LoxP allele on the X chromosome but do not express Cre recombinase in excitatory neurons of the forebrain. Control and ATRX-KO mice were housed in animal cages for 4–7 months before they were studied experimentally. Mice were weaned based on sex and a maximum of four male mice were housed per cage. All mice had access to food and water *ad libitum* and they were subject to a day/night cycle of 12h/12h. All experiments were performed between 9:00 AM–9:00 PM on mice that were between 16–28 weeks of age. Tail DNA from newborn pups was genotyped by PCR using the primers 17F, 18R, and *neo*^r (Bérubé et al. 2005).

2.2 Electrode Specifications

The stimulating electrodes were composed of stainless-steel wire with a diameter of 0.005 inches and they were insulated with Teflon except at the tips. The recording probes were purchased from NeuroNexus, Ann Arbor, MI. Each recording probe featured 16 recording channels that were aligned on a vertical shank made of silicon. Two types of probes differing in their inter-channel spacing were used; one had a spacing of 50 μm whereas the other featured a spacing of 100 μm between channels.

2.3 Experimental Protocol

2.3.1 Surgery

Experiments were performed on control and ATRX-KO mice at random and blinded to genotype throughout the whole experimental protocol, data collection, and analysis. Control and ATRX-KO male mice were weighed using an electronic balance and anesthetized with an initial dose of urethane at 1.25 mg/kg administered intraperitoneally (i.p) as per body weight (BW) (Hutchison et al. 2009). Beginning 15 minutes after the first anesthetic injection and continuing in 15-minute intervals thereafter, respiratory rate (RR) and toe pinch reflex were monitored to assess depth of anesthesia. If the depth of anesthesia was too shallow (indicated by rapid breathing, a clear toe pinch reflex, and in some cases, movement of the torso and head), mice were administered follow-up doses of 10% of the initial dose in 45-minute intervals for a maximum of 4 follow-up doses. Should the mouse still not be at the surgical level of anesthesia after 4 follow-up doses and 3 hours of waiting, that mouse was euthanized. Atropine (7.5 mg/kg) was delivered to the mouse 30 minutes after the first injection of urethane to prevent excess salivation. Approximately one hour after atropine administration, procaine was applied topically to the ear canal and to the surface of the head with a Q-tip. Once the mouse reached the surgical level of anesthesia (as indicated by complete absence of a toe pinch reflex and a slower RR with deeper breaths), it was secured to a stereotaxic frame for surgery.

The mouse was placed on a heating pad connected to a rectal thermometer which was used to detect body temperature in real-time. The heat pad was calibrated to maintain the body temperature of the mouse at 37 °C and it was covered with one sheet of tissue paper to prevent heat loss. Ear bars were carefully placed inside the ear canal of the mouse to prevent head rotation in the horizontal plane. A mouth bar was inserted behind the front teeth of the mouse and over the tongue to prevent swallowing of the tongue as well as to restrict head rotation in the vertical plane. The skull was leveled by placing bregma and lambda, two skull reference points, on the same horizontal plane. Once successfully mounted to the stereotaxic frame, the mouse head was tightly secured and unable to move in any direction.

A scalpel was used to make an incision of the scalp and small hemostats were used to secure the loose skin, keeping the skull exposed. A drill bit with a tip of approximately 1 mm² was inserted to an electric drill mounted on the stereotaxic frame and used to drill bilateral holes in the mouse skull above specific regions of interest. A mouse atlas (Paxinos and Franklin 1997) was used to

determine anterior/posterior (A/P) and medial/lateral (M/L) coordinates of those regions relative to bregma. The regions of interest were the MPP afferents from the EC (A/P: -4.1 mm; M/L: \pm 2.3 mm), the CA3 region of the hippocampus (A/P: -2.5 mm; M/L: \pm 2.2 mm), and the CA1 region of the hippocampus (A/P: -3.2 mm; M/L: \pm 2.8 mm). Additional holes were drilled above the frontal lobe and cerebellum to act as the recording ground and the stimulus ground, respectively. All holes were drilled slowly through the entire skull to prevent damage to the underlying brain. After drilling was complete, the skull was quickly washed with saline to dissolve any blood clots that formed within the holes. Prior to electrode implantation and optimization, the recording ground and stimulus ground screws were connected to their respective circuits.

2.3.2 Electrode Implantation and Optimization

2.3.2.1 CA3 to Proximal Apical Dendritic Stimulation

Our first pathway of interest was the CA3 to proximal apical dendritic CA1 via the Schaffer collaterals. Previous studies by our lab have successfully induced LTP in the stratum radiatum of CA1 *in vivo* using both high-frequency stimulation (HFS) as well as theta-burst stimulation (TBS) (Hutchison et al. 2009). Because of unknown reasons, we were unable to replicate these results for control or ATRX-KO mice using either HF or TBS at stimulus intensities ranging from 2–4 x threshold (T). As a result, we chose to investigate the CA3 to basal dendritic synapse, which displays more robust LTP than the CA3 to proximal apical dendritic synapse.

2.3.2.2 Stratum Oriens to Basal Dendritic Stimulation

The first hippocampal synaptic pathway under investigation was the stratum oriens (OR) from CA1/CA3 border to CA1 basal dendritic synapse. To verify that changes in the basal dendritic synapse were mediated by OR tetanus, a secondary control pathway was investigated which featured a response in the middle molecular layer (MML) of the DG following MPP stimulation. A 100 μ m recording probe was used to record from the basal dendrites of CA1 as well as the MML of the DG while remaining stationary between trials.

Each stimulation electrode was attached to a separate manipulator that were mounted to the stereotaxic frame to ensure precise adjustments during optimization and stability. The OR stimulus was oriented directly above its corresponding hole in the skull and it was slowly lowered to an initial depth of 1.0 mm below the surface of the brain. The MPP stimulus was placed more posterior on the skull, aligned with its corresponding hole, and it was slowly lowered to an initial depth of 1.0 mm below the surface of the brain as well. Lastly, the 100 μ m-interval recording probe was lowered through its respective hole to an initial depth of 1.5 mm. These initial depths were conservatively selected to speed up the electrode optimization process. Stimulating currents were delivered by a photo-isolated stimulus isolation unit (PSIU6, Astro-Med/Grass Instrument), controlled by a Grass S88 dual stimulator, which was triggered by a designed program using Master 8 pulse generator.

Both OR and MPP electrodes were optimized in a step-by-step fashion which involved repeatedly stimulating each electrode separately, viewing the waveform display of CA1 response on the computer, and deciding on whether to continue lowering the electrode or to stabilize at a certain depth. As the electrodes came closer to their region-of-interest, the stimulus intensity was gradually decreased until a threshold intensity was identified for the response-of-interest. While optimizing the depth of the stimulation electrodes was crucial for stimulating the appropriate hippocampal synaptic pathway, optimizing the depth of the recording probe allowed us to view responses in the basal dendrites of the CA1 region (in the upper recording channels closer to the surface) as well as the MML of the DG (in the lower recording channels), without having to move the probe between trials. Once the OR stimulus generated a basal dendritic response in the CA1 region, and the MPP stimulus generated an excitatory sink in the MML of DG, the stimulus electrodes and recording probe were considered to be optimized and left untouched for the rest of the experiment.

2.3.2.3 MPP to Distal Apical Dendritic Stimulation

The second hippocampal synaptic pathway under investigation was the direct MPP to distal apical dendritic synapse of CA1. To verify that changes in the distal apical dendritic synapse were mediated by MPP tetanus, a secondary control pathway, the stratum radiatum (RAD), was investigated which featured a response in the proximal apical dendrites of CA1, through the

Schaffer collateral pathway, upon stimulation. A 50 μm recording probe was used to record from CA1 while remaining stationary between trials.

Both RAD and MPP stimulation electrodes were attached to manipulators mounted on the stereotaxic frame, and the electrodes were lowered to a depth of 1.0 mm from the surface of the brain. The 50 μm recording probe was also lowered to an initial depth of 1.5 mm. Like previously, both MPP and RAD electrodes were optimized in a step-by-step fashion which involved repeatedly stimulating each electrode separately, viewing the waveform display of CA1 response on the computer, and deciding on whether to continue lowering the electrode or to stabilize at a certain depth. In this case, however, the responses-of-interest for the MPP and RAD stimuli were the distal apical dendritic sink and the proximal apical dendritic sink in the CA1 region, respectively. As the electrodes came closer to their region-of-interest, the stimulus intensity was gradually decreased until a threshold intensity was identified for the response-of-interest. The recording probe was also incrementally lowered through its respective hole in the skull until the waveform display on the computer screen featured a distal apical dendritic sink following MPP stimulation, and a proximal apical dendritic sink following RAD stimulation. At this point, the stimulus electrodes and recording probes were considered to be optimized and left untouched for the rest of the experiment.

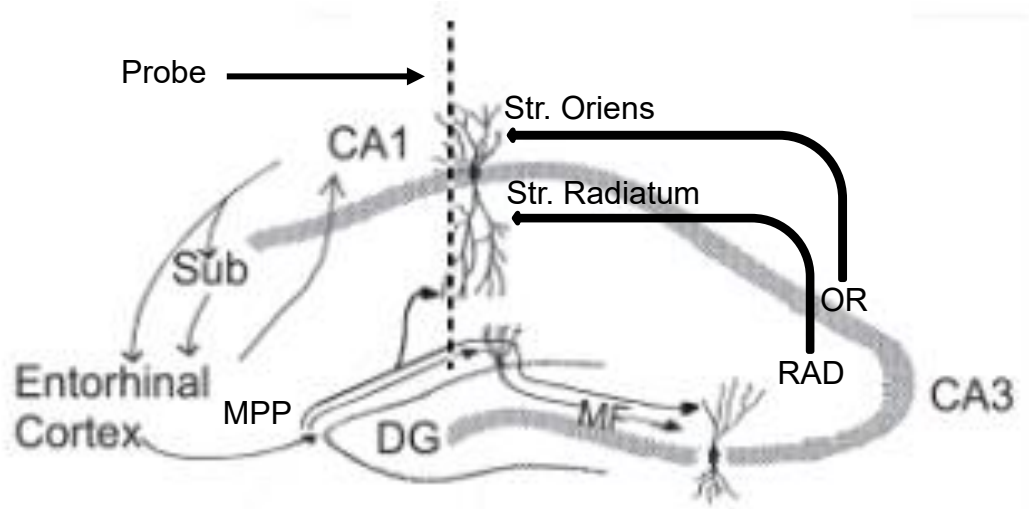


Fig. 2. Schematic illustrating electrode placement.

Coronal section of the mouse hippocampus illustrating the position of the recording probe penetrating the CA1 (same coordinates for 50 μm and 100 μm probes) as well as stimulating electrodes for MPP, stratum oriens as well as stratum radiatum. Stimulation of the angular bundle activated the medial perforant path (MPP) which projects monosynaptically to the distal apical dendrites of the CA1 region via the temporoammonic pathway. Stimulation of OR on CA1/CA3 border preferentially projects to the basal dendrites of the CA1 region. Finally, stimulation of RAD preferentially projects to the proximal apical dendrites of the CA1 region. DG excitation projects through mossy fibers (MF) to CA3, and CA3 in turn projects Schaffer collaterals to CA1. The 16-channel recording probe was inserted to record responses from the basal dendritic CA1 region, the proximal and distal apical dendritic CA1 region, as well as the dentate gyrus (DG) (modified from original image created by L. Stan Leung; permission obtained for use).

2.3.3 Experimental Paradigm

2.3.3.1 LTP Study

In the first study on LTP of the stratum oriens to CA1 basal dendritic excitation, the stratum oriens was tetanized to induce basal dendritic LTP, and the MPP to MML of the DG synapse was used as a control pathway in which changes in synaptic transmission were not expected. In the second study on LTP of the MPP to distal apical dendritic CA1 synapses, the MPP was

tetanzed to induce distal apical dendritic LTP while RAD to proximal apical dendritic CA1 synapse was used as the control pathway.

In each LTP study, the control and experimental pathways were stimulated separately. For each pathway, at 5 min intervals, 8 stimulation sweeps were delivered at 10 s intervals; each sweep consisted of two 0.2 ms duration pulses at 2 x threshold intensity (T), and an inter-pulse interval (IPI) of 50 ms (paired-pulse stimulation, PPS). The 16-channel recordings from the silicon probe were digitized and sampled at 24.4 kHz by a digital processor RA16 from Tucker Davis Technology (TDT) and the 8 sweeps were averaged by custom-made software. Average evoked potentials (AEPs) were recorded every 5 min for a total of 30 minutes during baseline, to produce 6 AEPs for each of the control and experimental pathways. The standard error of the mean (SEM) for the 6 first-pulse slope response E1 and second-pulse slope response E2 (see below) comprising the baseline was divided by the respective mean to estimate the statistical error inherent in the baseline recordings. Baseline recordings were continued until the SEM/mean ratio was less than 10% for a 30-minute period, which was considered to be a stable baseline.

Upon verification of a stable baseline for both E1 and E2 of control and experimental pathways, a high-frequency theta-burst stimulation (TBS; 10 trains at 10 s intervals, 10 bursts at 0.2 s intervals per train, 10 pulses at 100 Hz per burst, with 0.2 ms duration pulses) of stimulus intensity 4 x T was given to one stimulating electrode (either stratum oriens or MPP) to induce LTP. TBS has been shown to be effective for LTP induction in the hippocampus (Leung and Shen 1995). Following TBS, AEP recordings at 5-min intervals were resumed until 120 minutes after TBS.

2.3.3.2 Input-Output Curves

Input-output (I/O) curves were constructed from AEPs made during baseline (IO1) and two hours post-TBS (IO2). AEPs for I/O curves were recorded at increasing stimulus intensity (1, 1.5, 2, 3, 4, 6, and 10 x T); 4 sweeps were averaged for 1–6 x T intensity, and 2 sweeps at 10 x T intensity.

2.3.3.3 Lesions

At the end of recording, 4 sweeps of high-intensity (500 μ A) current of 0.5 s duration each with 50 ms interval paired-pulses were delivered to a stimulus electrode, in order to produce a lesion.

These lesions were then used to locate the stimulating electrode targeted for MPP, stratum oriens or stratum radiatum in the histological slide (below).

2.3.4 Electrode Verification

2.3.4.1 Perfusion

After all recordings have stopped, and lesions have been performed, a lethal dose of 30% urethane was injected into the mouse. With the heart still beating, the mouse was perfused intracardially, first with 60 mL of 10% saline solution to flush blood out of their body, and then with 30 mL of 4% formaldehyde solution to preserve brain tissue. The whole brain was then extracted and stored in 4% formaldehyde solution for a minimum of 72 hours before histological slicing and staining was performed.

2.3.4.2 Histological Procedures

Brains were placed on a cryostat to be frozen and sliced into 60 μm sections coronally. Slices were placed in a saline solution before being transferred to slides for staining. Slices were air-dried for a minimum of 24 hours at room-temperature and then stored in a freezer for safe-keeping. Histological staining was performed with thionin, which binds to Nissl bodies to highlight the cell bodies. Stained coronal sections were viewed with a light microscope to verify electrode placement (Fig. 3).

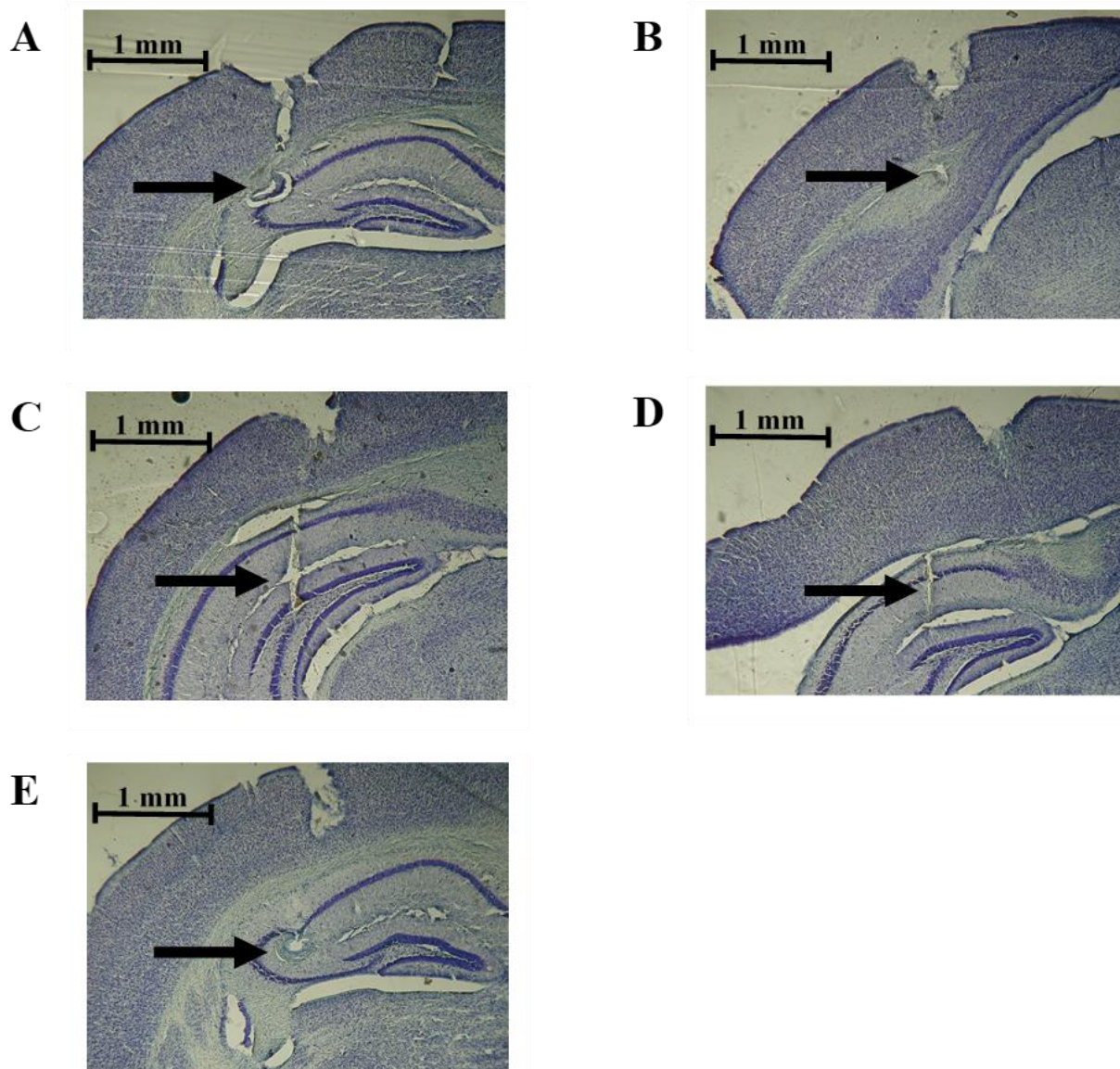


Fig. 3. Representative histological slices showing locations of different hippocampal electrodes.

Coronal sections taken from representative mouse brains stained with thionin. **A)** Location of electrode in stratum oriens that activated basal dendritic excitation in CA1. **B)** Location of MPP electrode in angular bundle that activated the distal apical dendrites of CA1 region. **C)** Location of recording probe penetrating CA1 from a representative control mouse. **D)** Location of a recording probe penetrating CA1 from a representative ATRX-KO mouse. **E)** Location of stimulating electrode in stratum radiatum that activated proximal apical dendritic excitation in CA1.

2.4 Inclusion Criteria

There were specific standards set in place for the baseline which had to be satisfied for the data to be included in the group analyses. Firstly, a stable 30-minute baseline (SEM/mean < 10%) was required for the TBS to be applied to the experimental hippocampal synaptic pathway under investigation. Baseline measures that were largely fluctuating were extended until 30 minutes of stability was achieved. Secondly, single-pulse responses at stimulus intensity $4 \times T$ during I/O curves were required to produce a sub-maximal response which was larger than the response evoked from baseline or post-TBS monitoring ($2 \times T$). If this condition was not met, that data was not included in the group analyses. Thirdly, the pathway-specific responses post-TBS were manually monitored for consistency and reliability by ensuring the response profile did not change as time passed. If the CSD depth profile shifted by one channel or more, resulting in a response profile change, that data was not included in the group analyses. Finally, responses that did not feature a clear component which could be mapped to a specific layer in CA1 were not included in the group analyses. In the event that more than one excitatory sink was identified in different channels, they were only included in the data analyses if it was concluded that the two sinks were independent of one another (i.e. short-latency distal apical dendritic excitatory sink through temporoammonic pathway and long-latency proximal apical dendritic excitatory sink through trisynaptic circuit, both following MPP stimulation).

2.5 Experimental Recordings

2.5.1 Raw Data

The 16-channel recording probe was inserted vertically, approximately perpendicular to CA1 pyramidal cell layer, allowing accurate layer-specific recording of extracellular evoked potentials following stimulation of hippocampal synaptic pathways. The 100 μm recording probe, because of its larger inter-channel distance, was able to record a depth profile ranging from the alveus of the CA1 region to the DG granule cell layer. The 50 μm recording probe, on the other hand, was optimized to record only from the alveus in CA1 to the hippocampal fissure.

2.5.2 Current Source Density Analysis

The AEPs obtained in the raw data were subjected to current source density (CSD) analysis to identify macroscopic locations of current sinks and sources by removing the effects of volume conduction—the spreading of current in the extracellular matrix. A one-dimensional CSD was calculated from the AEPs. CSD(z,t) as a function of depth (z) and time (t) was calculated by a second-order differencing formula:

$$\text{CSD}(z, t) = \sigma [2 \Phi(z, t) - \Phi(z + \Delta z, t) - \Phi(z - \Delta z, t)] / (\Delta z)^2 \quad (\text{Equation 1})$$

where $\Phi(z, t)$ is the potential at z and t, and Δz is the inter-channel spacing on the recording probe (either 100 μm or 50 μm depending on the hippocampal synaptic pathway under investigation). The conductivity σ was assumed to be constant and the output units of the CSD were V/mm^2 . 2-step CSD analysis was performed for all AEPs, including both control and experimental pathway responses as well as input-output curve and LTP study data.

After CSD analysis, the location of the maximal excitatory sink in CA1 following stimulation of a particular hippocampal synaptic pathway at a particular time point was identified and recorded as the largest negative slope with a duration of 1 ms (Fig. 4). This slope-of-interest was not necessarily the slope of the largest excitatory sink across all channels, but it was specific to the pathway that was stimulated and the cell layer that was subsequently activated from that hippocampal pathway. For the MPP to long-latency proximal apical dendritic synapse (via the trisynaptic circuit) only, the amplitude of the largest excitatory sink was recorded instead of the slope because it provided more reliable data with fewer fluctuations (Fig. 4).

The CSD-analyzed responses at each time point in the LTP study and at each stimulus intensity in the I/O curves were compiled in spreadsheets and the data were analyzed independently using slightly different paradigms.

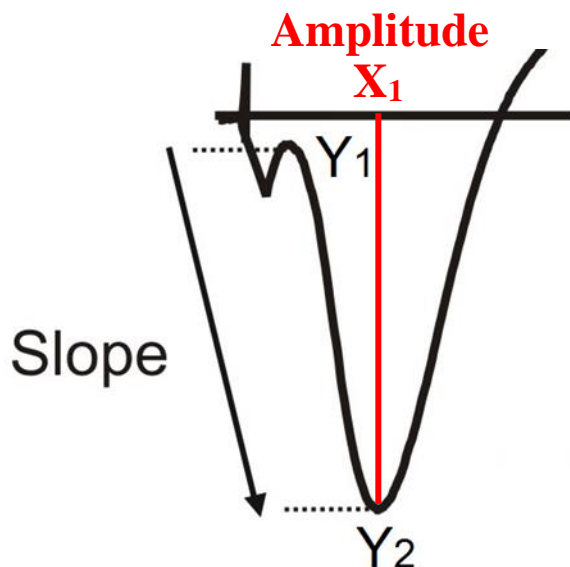


Fig. 4. Schematic illustrating slope and amplitude measurements.

Slope and amplitude measurements were taken from CSD-analyzed data in a specific way to ensure consistent measurements. Slope of the excitatory sink was calculated in 1 ms intervals throughout the whole duration of the rising phase (Y_1 to Y_2) and the value with the largest magnitude was taken as the slope estimate. Amplitude of the excitatory sink was calculated by taking the difference in amplitude from the peak of the excitatory sink relative to a marker placed to the left of the stimulus artifact, at the pre-stimulus baseline. In the schematic above, the amplitude recorded would be equivalent to subtracting the vertical magnitude of Y_2 from X_1 (modified from original version created by Clayton S. Law; permission obtained for use).

2.6 Data and Statistical Analyses

2.6.1 LTP Analysis

The excitatory E1 and E2 sink slopes obtained for each time point in the LTP study were compiled into spreadsheets for each individual mouse. Another parameter, known as paired-pulse facilitation (PPF), was calculated by taking the ratio of E2/E1. Each of E1, E2, and E2/E1 were normalized to their respective mean baseline measure. As such, normalized data were generated which featured an E1, E2, and E2/E1 response of approximately 100%, with any differences occurring post-TBS being attributed to changes in synaptic transmission in the experimental

pathway that was tetanized. The normalized E1, E2, and E2/E1 values were further subjected to averaging across 5 time points (-10 min, -5 min, 0 min, +5 min, +10 min) to smooth the data; averaging was not done across the time of TBS. A 5-point averaged data point is the average of 40 traces (5 time points averaged together, each being the average of 8 traces that were recorded from a particular hippocampal synaptic pathway).

Within-group analyses were performed using a one-way repeated measures (RM) analysis of variance (ANOVA), comparing baseline responses to post-TBS responses. Between-group analyses were performed using a two-way RM ANOVA, comparing post-TBS recordings between control and ATRX-KO groups across multiple time points. If group or group x time effect of an ANOVA was significant, multiple post-hoc comparisons were performed using the Newman Keuls test, which provides a conservative correction of type-I error. Significance level was set to 0.05.

2.6.2 Input-Output Curve Analysis

E1, E2, and E2/E1 data were also obtained for each stimulus intensity in the pre- and post-TBS I/O curves. Both E1 and E2 response for IO1 and IO2 for a particular hippocampal synaptic pathway were normalized by the respective pre-TBS E1 response. This was done to make comparisons between E1 and E2 both before and after tetanic stimulation more easily understood. Within-group analyses were performed using a two-way randomized block ANOVA, discounting the maximal stimulus intensity for E1 IO1 for both control and experimental pathways ($p < 0.05$). Between-group analyses were performed using a two-way RM ANOVA ($p < 0.05$). In both cases, Newman Keuls multiple post-hoc comparisons were performed given the omnibus test suggested a statistically significant difference. Finally, a paired t-test was used to compare maximal absolute sink responses (in mV/mm²) following stimulation at 10 x T between control and ATRX-KO mice.

Chapter 3

3 Results

3.1 Stratum oriens stimulation excites the basal dendritic CA1 region of hippocampal pyramidal cells

The stratum oriens to basal dendritic hippocampal synaptic pathway was studied in control ($n = 11$) and ATRX-KO mice ($n = 6$). In a representative control mouse, the profile of AEPs and CSDs were shown in Fig. 5. After optimization of the stimulating electrode in the stratum oriens, the threshold intensity was found to range between 15–50 μA , with an average threshold intensity of $30.5 \pm 3.11 \mu\text{A}$ for controls ($n = 10$) and $31.67 \pm 3.80 \mu\text{A}$ for ATRX-KO mice ($n = 6$), which was not significantly different between groups ($p = 0.81$, t-test). AEPs in each mouse were recorded with a 100 μm probe following paired-pulse stimulation (PPS) at a set intensity of 2 x threshold (T). CSD analysis yielded basal dendritic excitatory sinks and sources towards the cell layer.

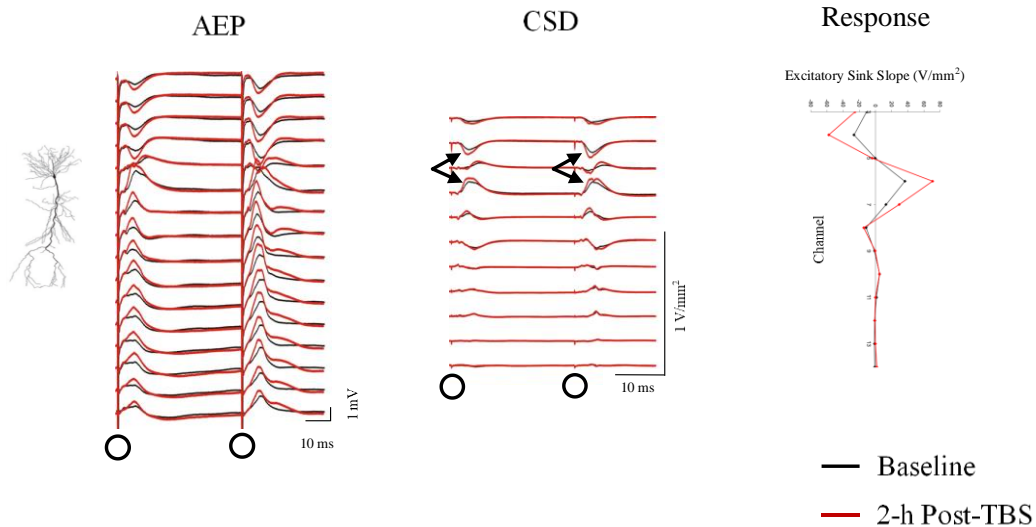


Fig. 5. Representative control mouse displaying basal dendritic excitation in CA1 following stratum oriens stimulation.

Stratum oriens stimulation was delivered at $80 \mu\text{A}$ ($2 \times$ threshold) stimulus intensity. Schematic pyramidal cell is depicted on the left with basal dendrites projecting upwards from the cell body and apical dendrites projecting downwards. Paired-pulse stimulation (indicated by black circles) of OR resulted in average evoked potentials (AEP; average of 8 sweeps) across 16 channels of the recording probe, which were analyzed for current source densities (CSDs) in the middle diagram. CSD response as a function of channel depth (3–14) is shown on the right. Current sink (upward black arrow) indicates basal dendritic excitation, and current source (downward black arrow) indicates reversal at the CA1 pyramidal cell layer. Black traces indicate baseline and red traces display recordings taken 2 hours post-OR-TBS, showing increased responses after TBS.

3.1.1 Baseline input-output relation: abnormal CA1 basal dendritic PPF following stratum oriens TBS in ATRX-KO mice

Baseline relation between basal dendritic excitation and stimulus intensity was studied by constructing input-output (I/O) curves during baseline recordings (IO1) for both control ($n = 10$; one control mouse did not have I/O data) and ATRX-KO mice ($n = 6$). The excitatory sink slope at the basal dendritic CA1 following the first pulse (E1) or the second pulse (E2) was observed to increase gradually with stratum oriens stimulus intensity in control mice (Fig. 6) and in ATRX-KO mice (Fig. 7). Excitatory slopes in each mouse were normalized by the maximal E1 during

baseline at 10 x T stimulus intensity. Two-way repeated measures ANOVA comparing control and ATRX-KO basal dendritic CA1 response following stratum oriens stimulation at increasing intensities displayed no statistically significant group (control versus ATRX-KO) or group x intensity interaction effect for E1 (Fig. 8A), or E2 response (Fig. 8B).

Paired-pulse facilitation (PPF), defined as the E2/E1 ratio, was calculated at each stimulus intensity. At 2 x T stimulus intensity, PPF was not significantly different between control and ATRX-KO mice (1.59 ± 0.081 and 1.37 ± 0.17 , respectively; $p > 0.05$, t-test). Similar PPF was found for both control and ATRX-KO mice at 1.5–6 x T intensity (Fig. 6; Fig. 7; $p < 0.05$). There was, however, a significant group effect ($F_{1,14} = 6.08$, $p = 0.027$) on E2/E1, indicating a difference in PPF between control and ATRX-KO mice (Fig. 8C). The PPF difference was larger at high (>3 x T) stimulus intensity (Fig. 8C), but Newman Keuls multiple pairwise post-hoc comparisons failed to reveal a statistically significant difference between groups at a fixed stimulus intensity ($p > 0.05$). These results indicate that ATRX-KO mice exhibit impaired basal dendritic PPF following stratum oriens stimulation, which is more exaggerated at high stimulus intensities (>3 x T).

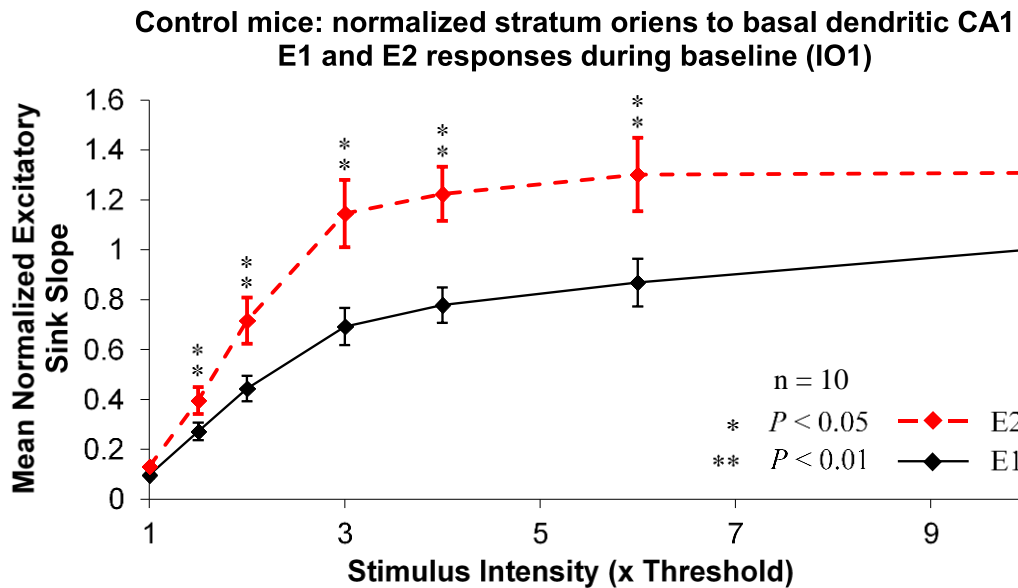


Fig. 6. Input-output curves of basal dendritic sink during baseline (pre-TBS) following stratum oriens stimulation in control mice.

Mean normalized excitatory sink slope (\pm SEM) (y-axis) in the basal dendritic CA1 region following first pulse (E1) and second pulse (E2) of stratum oriens stimulation at increasing intensity (x-axis) in control mice ($n = 10$). Response slopes in each mouse were normalized by E1 slope at 10 x threshold intensity. E2 was significantly larger than E1 from 1.5–6 x T ($p < 0.01$, Newman Keuls post-hoc comparison following a significant group x intensity interaction effect in two-way randomized block ANOVA). 10 x T difference between E1 and E2 was not considered due to normalizing procedure resulting in SEM of 0 for E1 at 10 x T.

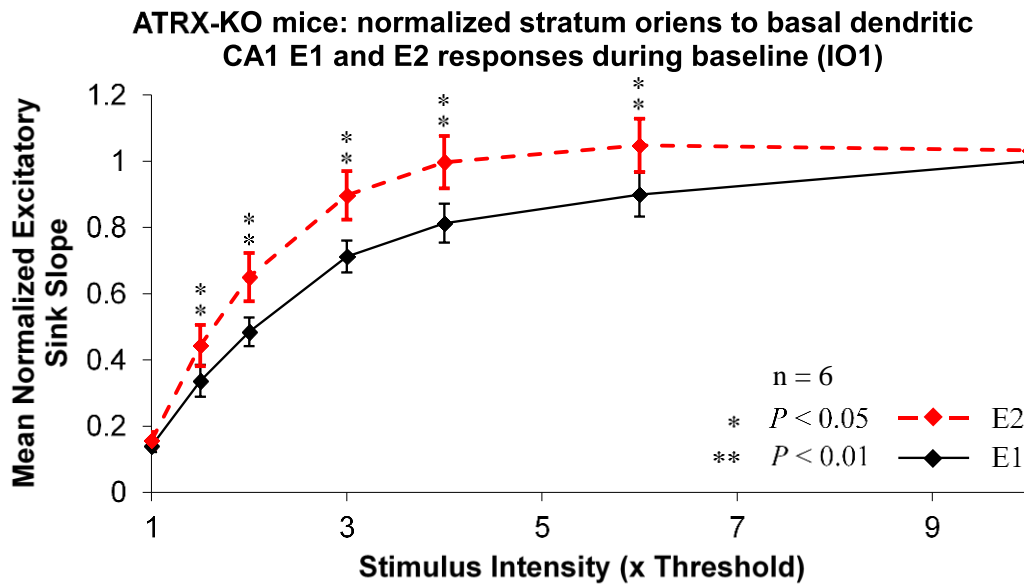


Fig. 7. Input-output curves of basal dendritic sink during baseline (pre-TBS) following stratum oriens stimulation in ATRX-KO mice.

Mean normalized excitatory sink slope (\pm SEM) (y-axis) in the basal dendritic CA1 region following first pulse (E1) and second pulse (E2) of stratum oriens stimulation at increasing intensity (x-axis) in ATRX-KO mice ($n = 6$). Response slopes in each mouse were normalized by E1 slope at 10 x threshold intensity. There was a significant group (E1 versus E2) x intensity interaction effect (two-way randomized block ANOVA; $F_{5,25} = 3.49$, $p = 0.0158$) between E1 and E2 responses. Newman Keuls multiple post-hoc comparisons revealed that E2 was significantly larger than E1 from 1.5–6 x T ($p < 0.01$). This confirms paired-pulse facilitation in the basal dendritic CA1 region during baseline in ATRX-KO mice.

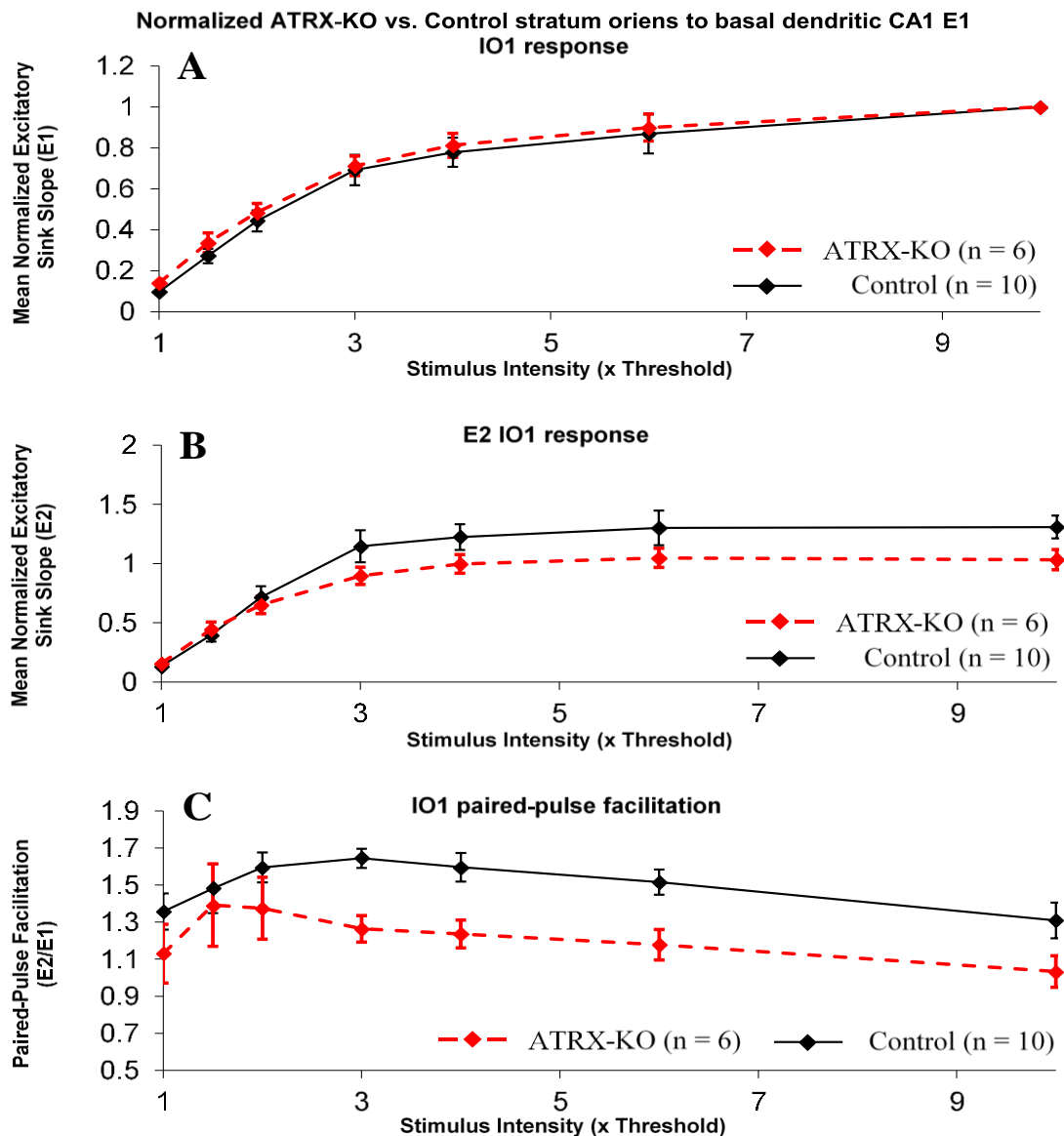


Fig. 8. Trend of decreased basal dendritic PPF following stratum oriens stimulation in ATRX-KO compared to control mice.

Mean normalized excitatory sink slope (\pm SEM) (y-axis) in the basal dendritic CA1 region following first pulse (E1) and second pulse (E2) of stratum oriens stimulation at increasing intensity (x-axis), as well as basal dendritic paired-pulse facilitation (PPF) in control (n = 10) and ATRX-KO mice (n = 6). **A**) E1 response in pre-TBS I/O curve (IO1) displayed no significant differences between control and ATRX-KO mice, as verified by two-way repeated measures ANOVA. **B**) Same as (A) but E2 response was plotted instead of E1. **C**) PPF was lower in ATRX-KO compared to control (group effect, two-way repeated measures ANOVA, see Results).

3.1.2 Time course analysis: normal CA1 basal dendritic LTP in ATRX-KO mice following stratum oriens TBS

Upon establishing a stable baseline (see Methods), theta-burst stimulation (TBS) was delivered to the stratum oriens at 4 x T to induce LTP in the basal dendritic CA1 region of the hippocampus. The length of time taken to establish a stable baseline varied between 30–60 minutes but did not differ between control and ATRX-KO mice. LTP was demonstrated as an increase in basal dendritic CA1 response following stratum oriens TBS for 2 hours post-TBS (Fig. 5). Both control (n = 11) and ATRX-KO mice (n = 6) displayed statistically significant LTP in the basal dendritic CA1 region following stratum oriens TBS. For statistical analysis, each measure was averaged from five consecutive time points, and the post-TBS times started at 12 min and ended at 112 min. The basal dendritic CA1 response E1 was significantly increased after TBS compared to the baseline in control (Fig. 9) and ATRX-KO mice (Fig. 10) (one-way repeated measures ANOVA: $F_{22,220} = 5.96, p < 0.0001$ and $F_{22,110} = 7.36, p < 0.0001$, respectively). E2 response was also significantly increased from baseline in control and ATRX-KO mice (one-way repeated measures ANOVA: $F_{22,220} = 4.72, p < 0.0001$ and $F_{22,110} = 5.76, p < 0.0001$, respectively). Newman Keuls multiple post-hoc comparisons indicated that the increase in E1 and E2 compared to baseline occurred at the first time point following TBS and was sustained for the full two-hour post-TBS for both control and ATRX-KO mice ($p < 0.05$). Because both E1 and E2 responses potentiated, normalized paired-pulse facilitation (E2/E1) post-TBS vs. pre-TBS did not change for either control or ATRX-KO mice ($p < 0.05$, Newman Keuls multiple post-hoc comparisons), although there was a significant within-groups effect for control mice (one-way repeated measures ANOVA, $F_{22,220} = 1.64, p = 0.039$). Two-way repeated measures ANOVA comparing time courses of normalized E1, E2, and paired-pulse facilitation post-TBS between groups displayed no significant group or group x time interaction effects (Fig. 11A, B, C). From these data, we can conclude that both control and ATRX-KO mice exhibit statistically significant LTP in the basal dendritic CA1 region following stratum oriens TBS, with no differences between groups across E1, E2, or E2/E1 response over time.

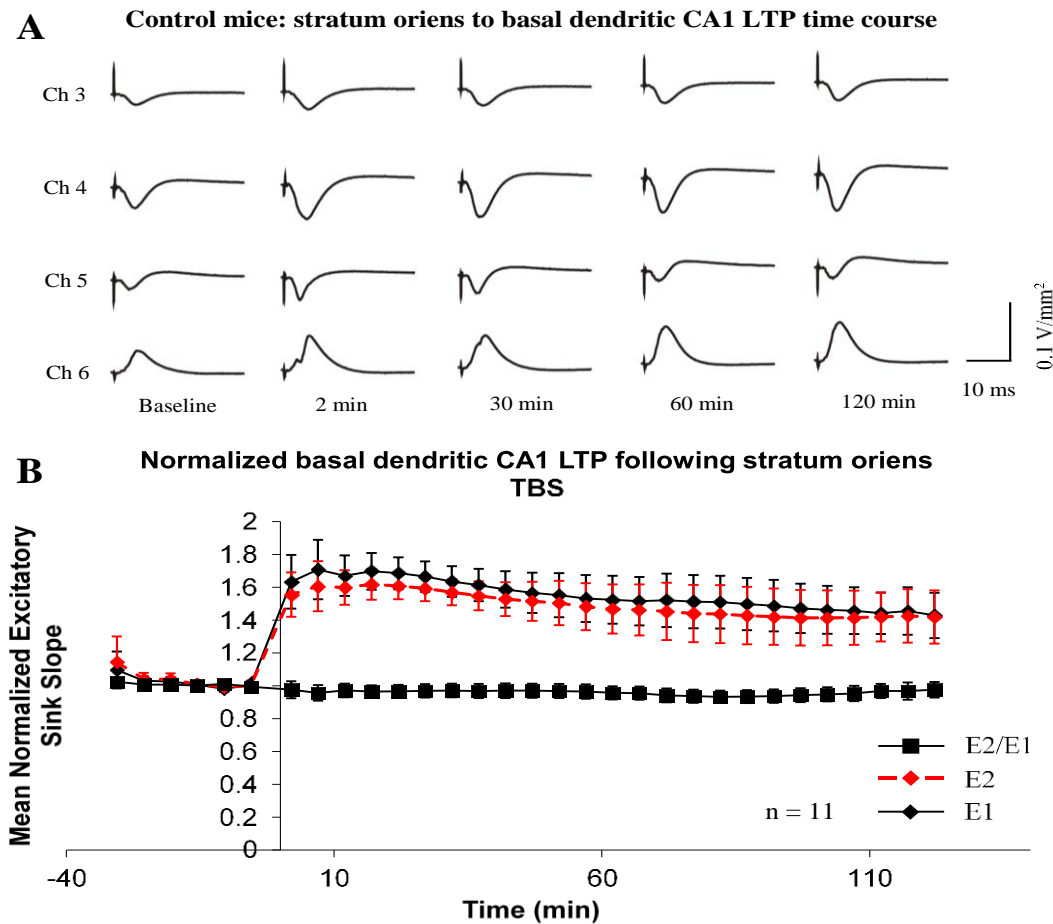


Fig. 9. E1 and E2 basal dendritic LTP following stratum oriens TBS in control mice.

A) Basal dendritic CA1 LTP time course following stratum oriens TBS in a representative control mouse. CSD responses of selected channels are displayed for baseline, 2 min, 30 min, 60 min, and 120 min post-TBS. Basal dendritic sink (excitation) is shown in Ch 4, with a corresponding source at the pyramidal cell layer in Ch 6. **B)** Mean normalized excitatory sink slope (\pm SEM) (y-axis) in the basal dendritic CA1 region as a function of time (x-axis) both before and after LTP induction by stratum oriens TBS (time = 0) in control mice (n = 11). Response following first pulse (E1), second pulse (E2), and ratio (E2/E1) were normalized by their respective baseline mean measure and further averaged across 5 consecutive time points. Responses at 2, 7, 117, and 122 min post-TBS, and -5, -10, -25, -30 min during baseline were not averaged, but were plotted to show a more complete time course. E1 and E2 responses showed significant increase post-TBS compared to their respective baseline (Newman-Keuls post-hoc difference after a significant one-way repeated measures ANOVA, see Results).

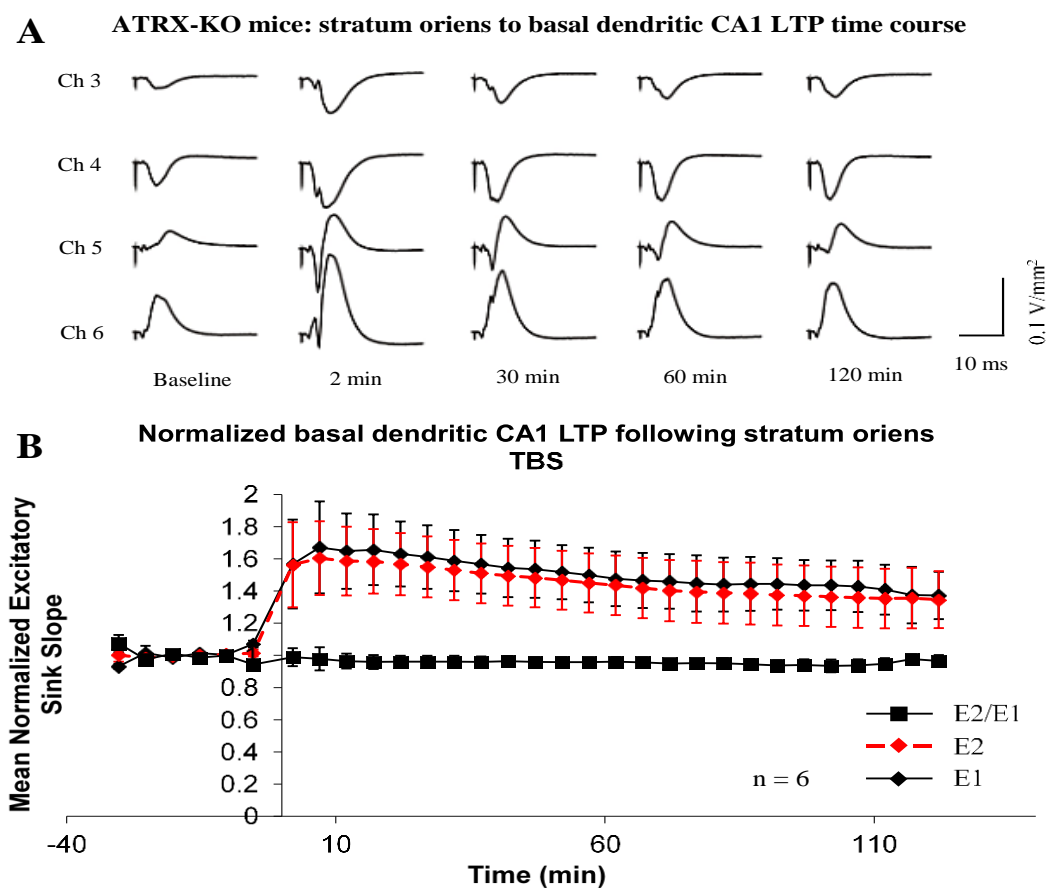


Fig. 10. E1 and E2 basal dendritic LTP following stratum oriens TBS in ATRX-KO mice.

A) Basal dendritic CA1 LTP time course following stratum oriens TBS in a representative ATRX-KO mouse. CSD responses of selected channels are displayed for baseline, 2 min, 30 min, 60 min, and 120 min post-TBS. Basal dendritic sink (excitation) is shown in Ch 4, with a corresponding source at the pyramidal cell layer in Ch 6. B) Mean normalized excitatory sink slope (\pm SEM) (y-axis) in the basal dendritic CA1 region as a function of time (x-axis) both before and after LTP induction by stratum oriens TBS (time = 0) in ATRX-KO mice (n = 6). Response following first pulse (E1), second pulse (E2), and ratio (E2/E1) were normalized by their respective baseline mean measure and further averaged across 5 consecutive time points. Responses at 2, 7, 117, and 122 min post-TBS, and -5, -10, -25, -30 min during baseline were not averaged, but were plotted to show a more complete time course. E1 responses showed significant increase post-TBS compared to baseline (Newman Keuls post-hoc difference following a significant one-way repeated measures ANOVA). The same was found for E2 responses. Normalized E2/E1 ratio did not change post-TBS compared to baseline.

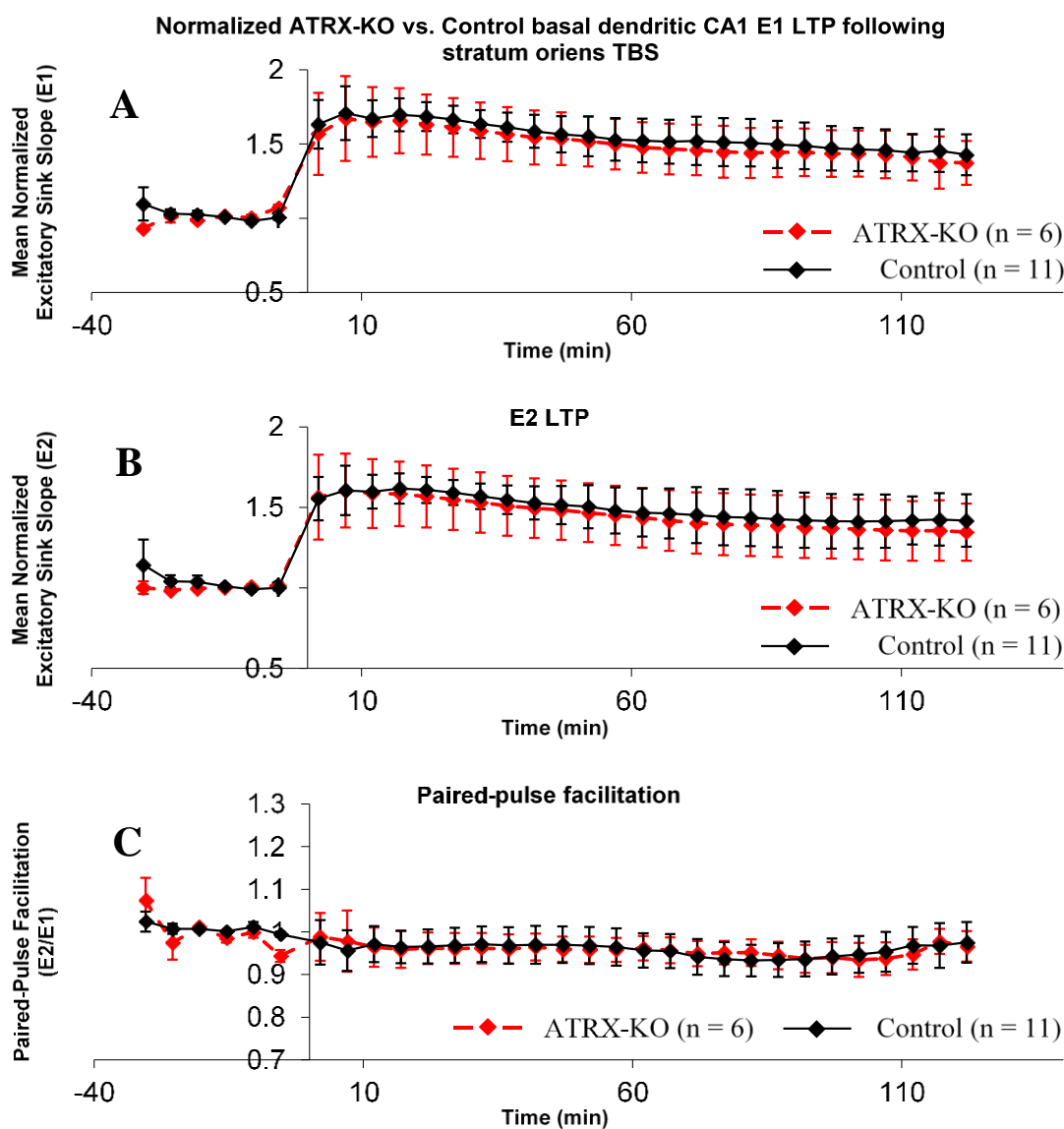


Fig. 11. Normalized basal dendritic E1, E2, and E2/E1 time courses of ATRX-KO mice compared to controls.

Mean normalized excitatory sink slope (\pm SEM) (y-axis) in the basal dendritic CA1 region as a function of time (x-axis) both before and after LTP induction by stratum oriens TBS (time = 0) in control (n = 11) and ATRX-KO mice (n = 6). Response following first pulse (E1), second pulse (E2), and ratio (E2/E1) were normalized by their respective baseline mean measure and further averaged across 5 consecutive time points. **A**) E1 response was not significantly different between control and ATRX-KO mice (two-way repeated measures ANOVA). **B**) Same as (A), but E2 was plotted instead of E1. **C**) Paired-pulse facilitation (E2/E1) plotted with time also showed no difference between groups.

3.1.3 Input-output relation two hours post-TBS: E1 LTP at multiple intensities is not affected in ATRX-KO mice

A final I/O curve (IO2) was generated for the stratum oriens to basal dendritic CA1 at 2 hours post-TBS for both control ($n = 10$) and ATRX-KO mice ($n = 6$). Like in IO1, control and ATRX-KO mice displayed statistically significant paired-pulse facilitation (PPF) in the basal dendrites of CA1 following stratum oriens stimulation two hours post-TBS. IO2 of controls, like IO1, showed significant differences between E2 and E1 at all stimulus intensities (Fig. 12A), while IO2 of ATRX-KO mice (Fig. 13A), only displayed a significant increase of E2 over E1 at 2–3 x T (Newman Keuls multiple post-hoc comparisons, $p < 0.05$ for each). Comparison of E1 response, or E2 response, between IO1 and IO2 (Fig. 12B, C) in control mice revealed a significant group (IO1 versus IO2) x intensity interaction effect (E1: $F_{5,45} = 9.06$, $p < 0.0001$; E2: $F_{6,54} = 2.90$, $p = 0.016$) and statistically significant increases in E1 and E2 in IO2 relative to IO1 at stimulus intensities of 2 x T or greater ($p < 0.05$). Thus, control mice experienced E1 and E2 basal dendritic LTP at more than one stimulus intensity following stratum oriens TBS. Comparisons of E1 response between IO1 and IO2 in ATRX-KO mice also showed a significant group x intensity interaction effect (Fig. 13B) ($F_{5,25} = 5.45$, $p = 0.0016$), but only responses at higher intensities (4–10 x T) displayed significant increases in E1 in IO2 relative to IO1 (Newman Keuls multiple post-hoc comparisons, $p < 0.05$). Interestingly, comparisons of E2 response between IO1 and IO2 in ATRX-KO mice showed no significant group difference (Fig. 13C), except for a trend of a group x intensity interaction effect ($F_{6,30} = 2.09$, $p = 0.084$), suggesting a larger E1 in IO2 compared to IO1. These findings suggest that E2 in ATRX-KO mice were not reliably increased across stimulus intensity, because of the decrease in PPF at higher intensity. However, comparisons of E1 and E2 response in IO2 between control and ATRX-KO mice (Fig. 14A, B) suggest that there are no significant group or group x intensity interaction effects between groups (verified by two-way repeated measures ANOVA). Finally, I/O curves of paired-pulse facilitation post-TBS were not different between control and ATRX-KO mice (Fig. 14C), and two-way ANOVA showed no significant group or group x intensity interaction effect. In conclusion, the I/O curves of both control and ATRX-KO mice confirm statistically significant basal dendritic LTP of E1 at more than one stimulus intensity following stratum oriens TBS, and that I/O curves of E1, E2, and E2/E1 responses were not found to differ between ATRX-KO mice and control groups.

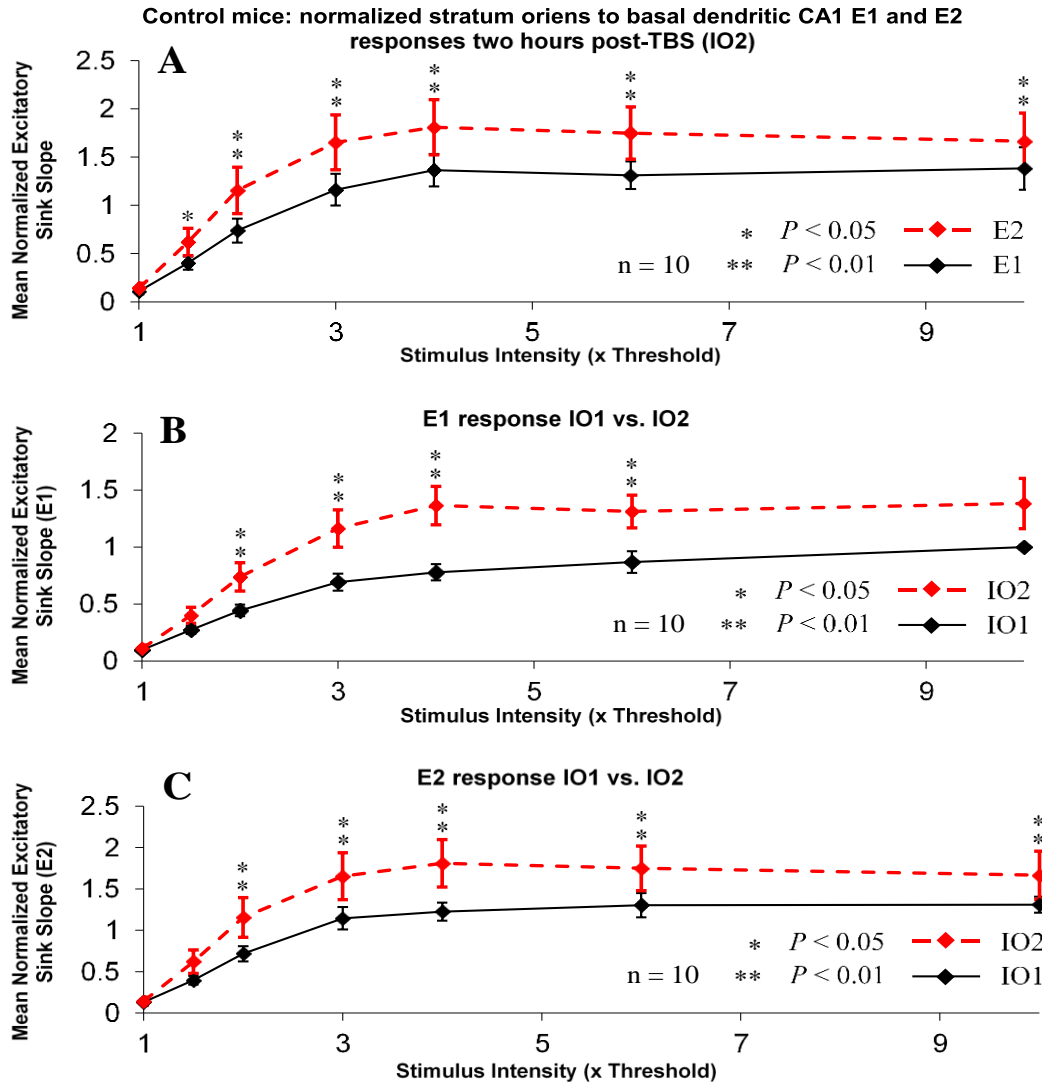


Fig. 12. IO2 response for control mice confirmed LTP in the basal dendritic CA1 at different stimulus intensities following stratum oriens TBS.

Mean normalized excitatory sink slope (\pm SEM) in basal dendritic CA1 region following first pulse (E1) and second pulse (E2) of stratum oriens stimulation at increasing intensity (x-axis) two hours post-TBS (IO2) in control mice ($n = 10$). **A**) E1 and E2 response as a function of stimulus intensity. E2 was significantly greater than E1 at 2–10 x T ($p < 0.01$, Newman Keuls post-hoc comparisons following significant two-way randomized block ANOVA). **B**) E1 response plotted for baseline (IO1) and IO2. E1 responses in IO2 were significantly greater than in IO1 at stimulus intensities of 2–6 x T ($p < 0.01$). **C**) Same as (B) except E2 responses were plotted with significant post-hoc differences after a significant group x intensity interaction effect in two-way ANOVA.

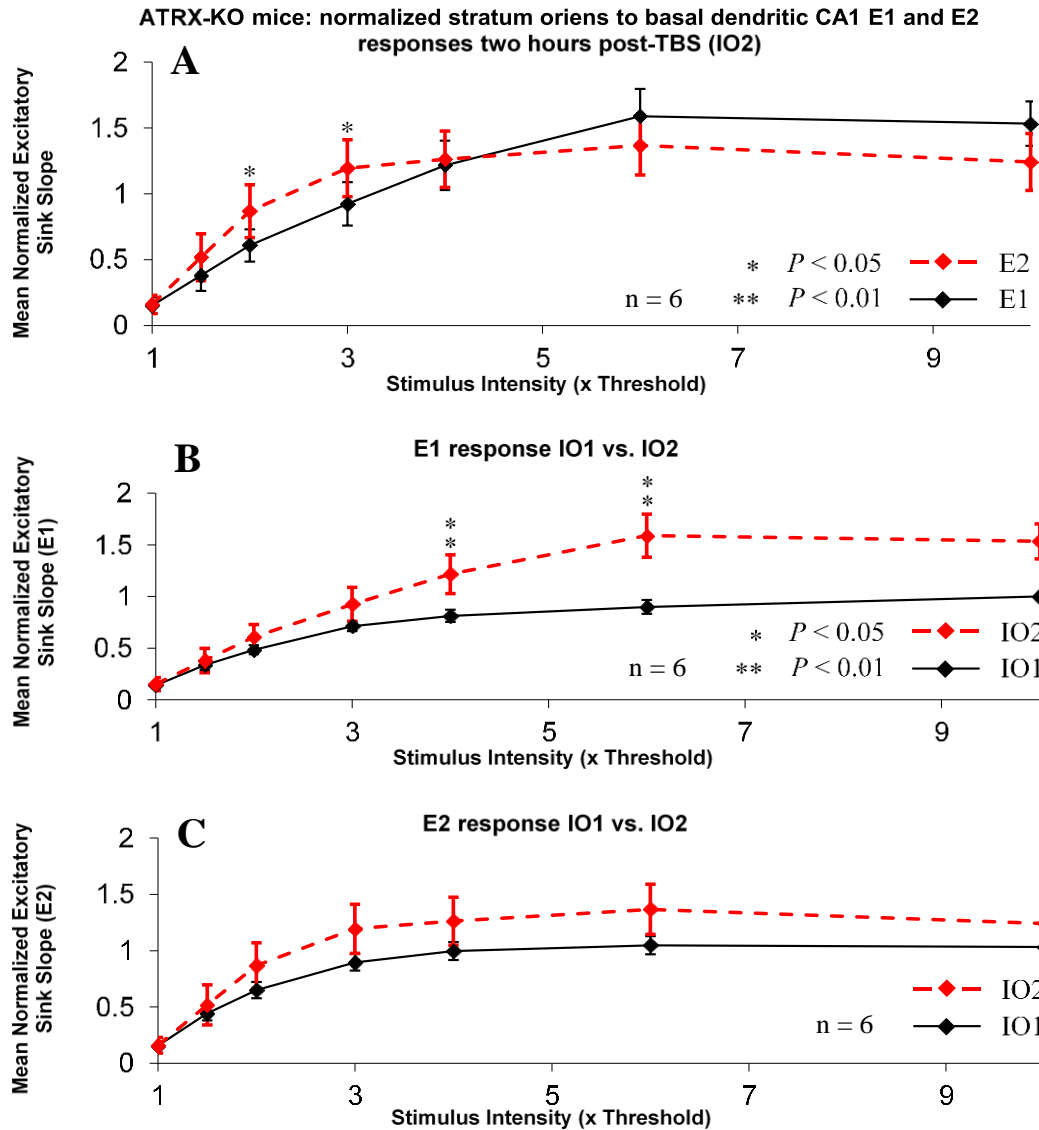


Fig. 13. IO2 response for ATRX-KO mice indicates PPF as well as trend of potentiated E1 and E2 responses compared to IO1.

Mean normalized excitatory sink slope (\pm SEM) in basal dendritic CA1 region after first pulse (E1) and second pulse (E2) of stratum oriens stimulation at increasing intensity (x-axis) two hours post-TBS (IO2) in ATRX-KO mice (n = 6). **A**) E1 and E2 response as a function of stimulus intensity. E2 was significantly greater than E1 at 2–3 x T ($p < 0.05$, Newman Keuls post-hoc comparisons following significant two-way randomized block ANOVA). **B**) E1 response plotted for baseline (IO1) and IO2. E1 responses in IO2 were significantly greater than in IO1 at stimulus intensities of 4–6 x T ($p < 0.01$). **C**) Same as (B) except E2 responses were plotted with no significant differences in E2 response between IO1 and IO2 (see Results).

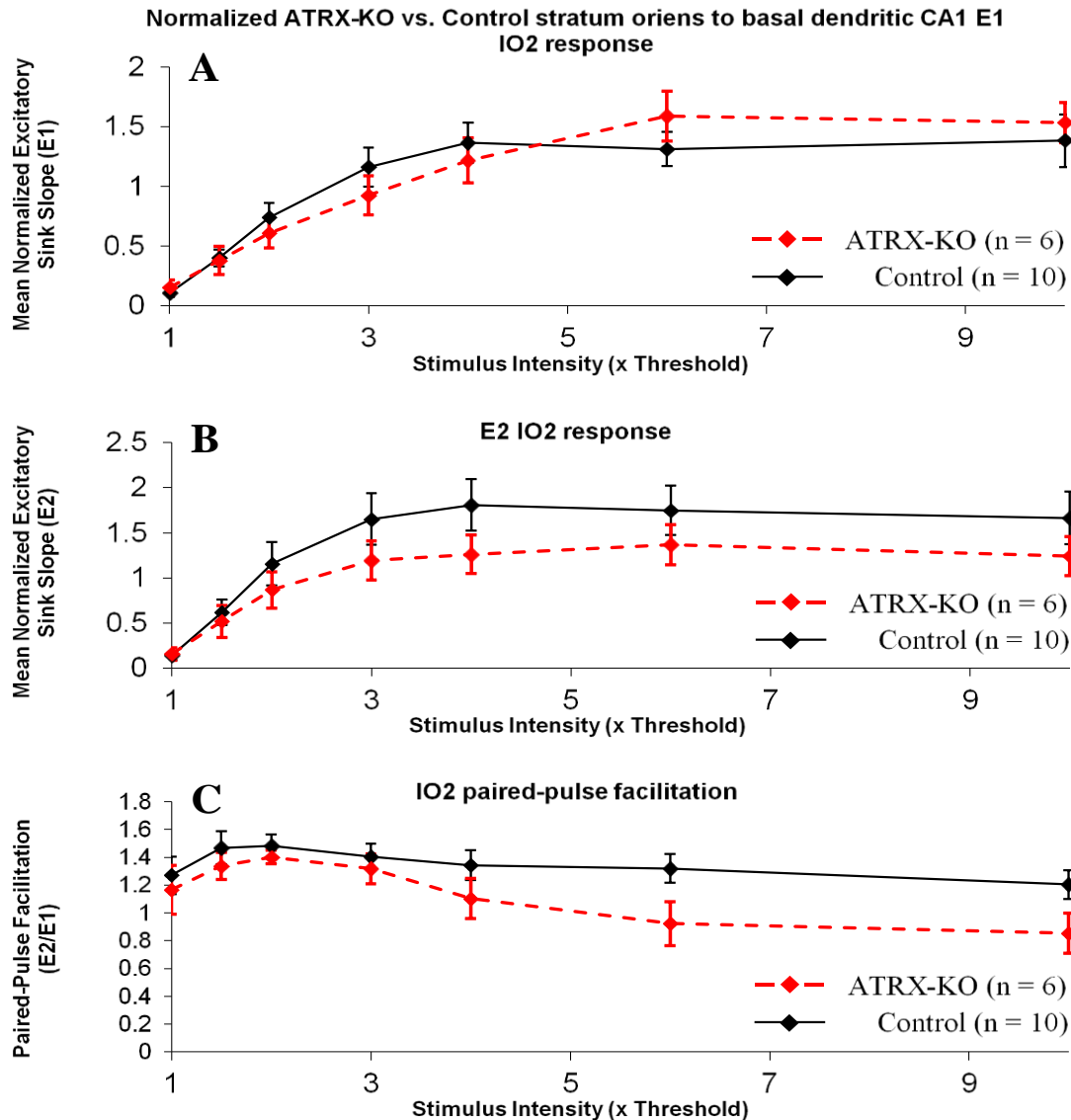


Fig. 14. No significant difference between control and ATRX-KO mice in E1, E2, or E2/E1 response at 2 hours post-TBS (IO2).

Mean normalized excitatory sink slope (\pm SEM) in basal dendritic CA1 region after first pulse (E1) and second pulse (E2) of stratum oriens stimulation at increasing intensity (x-axis) two hours post-TBS (IO2), as well as basal dendritic paired-pulse facilitation (PPF) in control (n = 10) and ATRX-KO mice (n = 6). **A**) E1 response in IO2 displays no significant differences between control and ATRX-KO mice, as verified by two-way repeated measures ANOVA. **B**) Same as (A) but E2 response was plotted instead of E1. **C**) PPF, measured by E2/E1, at increasing stratum oriens stimulus intensity displayed no significant group or group x intensity interaction effect between control and ATRX-KO mice (two-way repeated measures ANOVA).

3.2 MPP stimulation excites the middle molecular layer of DG granular cells

The medial perforant path (MPP) to middle molecular layer of the dentate gyrus (DG) synaptic pathway served as a non-tetanized control pathway that was recorded alongside the stratum oriens to basal dendritic pathway in control ($n = 8$; two control mice did not display clear MPP to middle molecular layer of DG excitation) and ATRX-KO mice ($n = 6$) (Fig. 15). At the MPP stimulating electrode, the threshold intensity was found to range between 10–25 μA , with an average threshold intensity of $15.88 \pm 1.90 \mu\text{A}$ for controls and $24.17 \pm 5.69 \mu\text{A}$ for ATRX-KO mice, which was not significantly different between groups ($p = 0.15$, t-test).

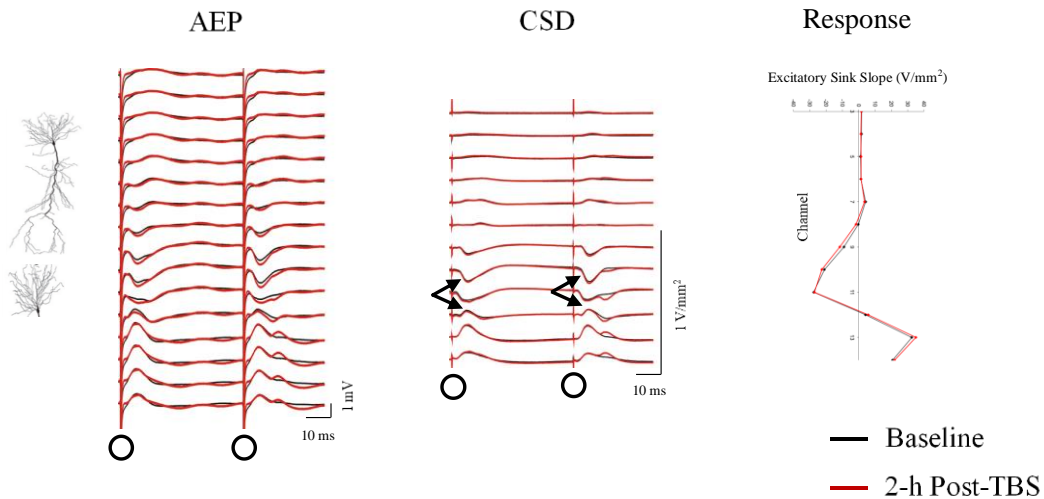


Fig. 15. Representative control mouse displaying excitation of the middle molecular layer of DG following MPP stimulation.

MPP stimulation was delivered at $40 \mu\text{A}$ ($2 \times$ threshold) stimulus intensity. Schematic pyramidal cell with dentate granule cell below it is depicted on the left. The granular cell projects dendrites upwards into the molecular layer of the DG. Paired-pulse stimulation (indicated by black circles) of MPP resulted in average evoked potentials (AEP; average of 8 sweeps) across 16 channels of the recording probe, which were analyzed for current source densities (CSDs) in the middle diagram. CSD response as a function of channel depth (3–14) is shown on the right. Current sink (upward black arrow) indicates excitation of the middle molecular layer of DG granule cells, and current source (downward black arrow) indicates reversal at the DG granular cell layer. Black traces indicate baseline and red traces display recordings taken 2 hours post-OR-TBS, showing no change in this pathway after TBS.

3.2.1 Baseline input-output relation: The MPP-DG response saturates at lower MPP stimulus intensity in ATRX-KO mice at baseline

I/O curves were generated during baseline recordings (IO1) for both control ($n = 8$) and ATRX-KO mice ($n = 6$). The largest excitatory sink slope corresponding to the middle molecular layer of the DG following the first pulse (E1) and second pulse (E2) was recorded, and E2/E1 was calculated at each stimulus intensity.

Both control ($n = 8$) and ATRX-KO mice ($n = 6$) were found to display significant PPF ($E2 > E1$) in the middle molecular layer of DG response following MPP stimulation. In controls, $E2$ was significantly greater than $E1$ ($p < 0.01$) at stimulus intensities of 1–6 x T (Fig. 16), whereas in ATRX-KO mice, $E2$ was significantly larger than $E1$ ($p < 0.05$) at intensities of 1.5–6 x T (Fig. 17). Two-way repeated measures ANOVA comparing control and ATRX-KO middle molecular layer of DG response following increasing stimulus intensity at MPP displayed a statistically significant group x intensity interaction effect for $E1$ (Fig. 18A; $F_{5,60} = 2.62$, $p = 0.033$), and for $E2$ response (Fig. 18B; $F_{6,72} = 2.92$, $p = 0.013$). Specifically, normalized $E1$ and $E2$ responses in the middle molecular layer of DG in ATRX-KO mice were found to be significantly greater than controls at stimulus intensities of 3–6 x T (Newman Keuls multiple post-hoc comparisons, $p < 0.05$). Additionally, there was a significant group x intensity interaction effect when comparing $E2/E1$ response in control and ATRX-KO mice (Fig. 18C; $F_{6,72} = 3.39$, $p = 0.0053$), but pairwise comparisons suggested a significant difference only at a stimulus intensity of 1 x T (Newman Keuls post-hoc test, $p < 0.01$). From these results, we can conclude that there are differences in MPP to middle molecular layer of the DG synaptic transmission between control and ATRX-KO mice which are present during baseline. While they both featured PPF of the MPP to DG synapse, the ATRX-KO mice showed a lower intensity for response saturation.

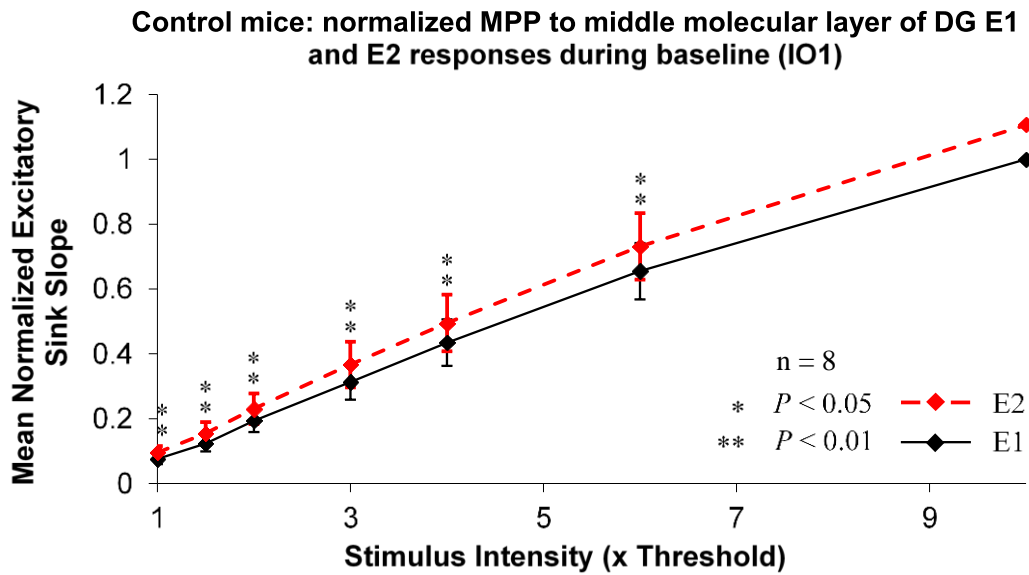


Fig. 16. Input-output curves of middle molecular layer of DG sink during baseline (pre-TBS) following MPP stimulation in control mice.

Mean normalized excitatory sink slope (\pm SEM) (y-axis) in the middle molecular layer of the DG following first pulse (E1) and second pulse (E2) of MPP stimulation at increasing intensity (x-axis) in control mice ($n = 8$). Response slopes were normalized by E1 slope at 10 x threshold intensity in each mouse. E2 was significantly larger than E1 from 1–6 x T ($p < 0.01$, Newman Keuls post-hoc comparison following a significant group x intensity interaction effect in two-way randomized block ANOVA). 10 x T difference between E1 and E2 was not considered due to normalizing procedure resulting in SEM of 0 for E1 at 10 x T.

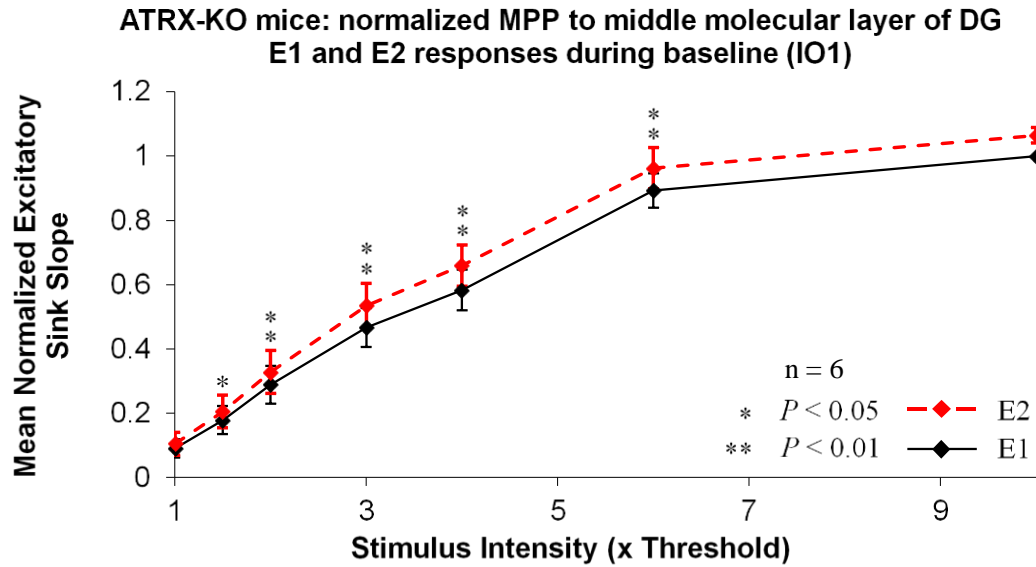


Fig. 17. Input-output curves of middle molecular layer of DG sink during baseline (pre-TBS) following MPP stimulation in ATRX-KO mice.

Mean normalized excitatory sink slope (\pm SEM) (y-axis) in the middle molecular layer of the DG following first pulse (E1) and second pulse (E2) of MPP stimulation at increasing intensity (x-axis) in ATRX-KO mice ($n = 6$). Response slopes were normalized by E1 slope at 10 x threshold intensity in each mouse. There was a significant group x intensity interaction effect (two-way randomized block ANOVA; $F_{5,25} = 4.11$, $p = 0.0074$) between E1 and E2 responses. Newman Keuls multiple post-hoc comparisons revealed that E2 was significantly larger than E1 from 1.5–6 x T ($p < 0.05$). This confirmed paired-pulse facilitation in the middle molecular layer of DG during baseline in ATRX-KO mice.

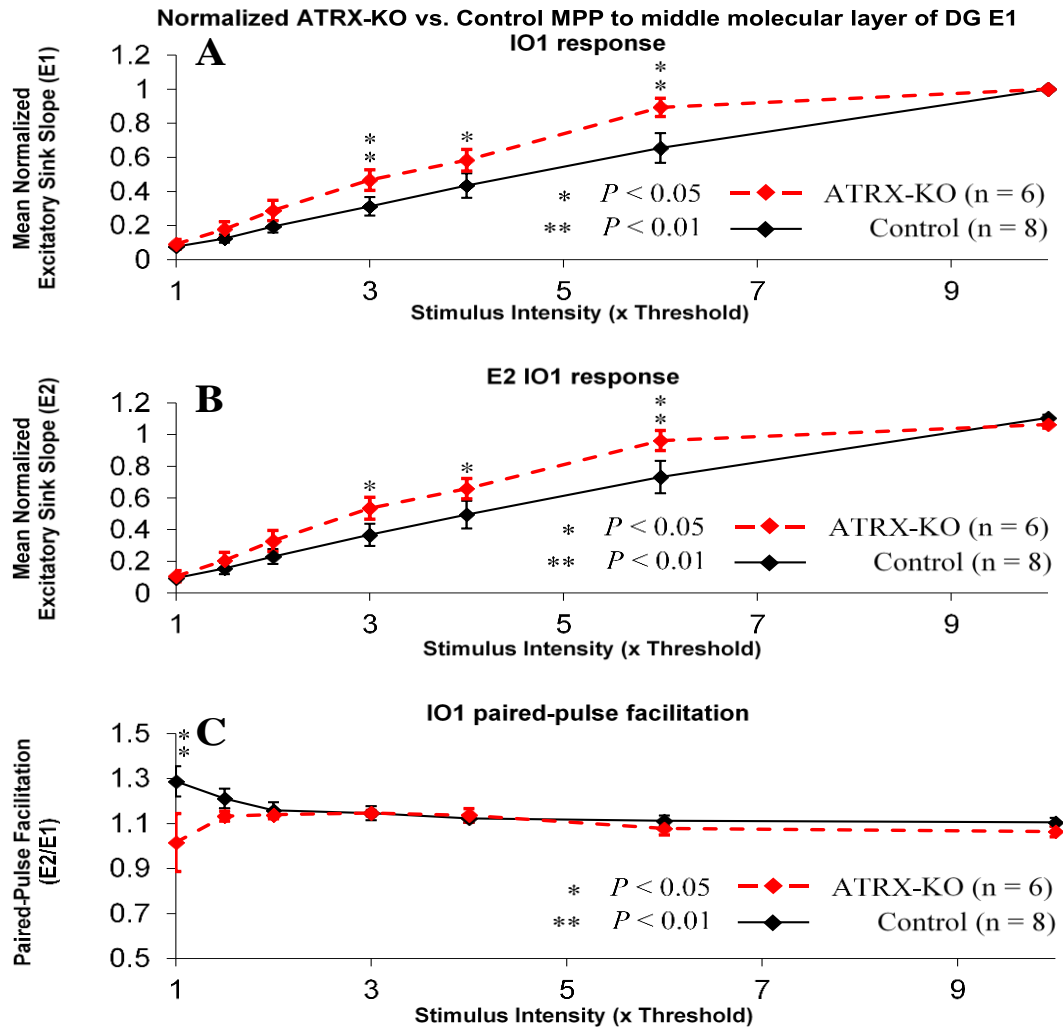


Fig. 18. Altered input-output curves of the MPP to middle molecular layer of DG in ATRX-KO compared to control mice.

Mean normalized excitatory sink slope (\pm SEM) (y-axis) in the middle molecular layer of DG following first pulse (E1) and second pulse (E2) of MPP stimulation at increasing intensity (x-axis), as well as paired-pulse facilitation (PPF) in control (n = 8) and ATRX-KO mice (n = 6). **A)** E1 response in pre-TBS I/O curve (IO1) is more excitable in ATRX-KO mice at stimulus intensities of 3–6 x T compared to controls ($p < 0.05$, Newman Keuls post-hoc comparisons following significant group x intensity interaction effect in two-way repeated measures ANOVA). **B)** Same as (A) but E2 response was plotted instead of E1. **C)** PPF, measured as E2/E1, was significantly different between groups only at a stimulus intensity of 1 x T ($p < 0.01$, see Results).

3.2.2 Time course analysis: ATRX-KO mice display normal MPP-DG synaptic transmission following LTP induction

Following TBS of stratum oriens, the excitatory DG sink evoked by MPP stimulation (a pathway meant to be control for the tetanized pathway) did not show a significant change for E1, E2, or E2/E1, at 2 x T intensity, in control mice ($n = 8$; Fig. 15) compared to baseline. We did, however, find that E1 response following MPP stimulation showed a statistical trend to be different among time points (one-way repeated measures ANOVA: $F_{22,176} = 1.52$, $p = 0.073$; Fig. 19). Nevertheless, the average E1 response in the middle molecular layer of the DG following stratum oriens TBS was $106.23 \pm 6.62\%$ ($n = 8$ control mice), whereas basal dendritic E1 LTP in controls was $155.29 \pm 13.66\%$ ($n = 11$). In ATRX-KO mice ($n = 6$), a statistically significant difference was observed in E1 and E2 response before and after TBS (Fig. 20; E1: $F_{22,110} = 4.13$, $p < 0.0001$; E2: $F_{22,66} = 2.37$, $p = 0.0038$, one-way repeated measures ANOVA). However, Newman Keuls multiple post-hoc comparisons only indicate a significant increase in E1 response relative to baseline at 115 min post-TBS, whereas not a single time point for E2 response was found to be significantly different than baseline values ($p < 0.05$). E2/E1 ratio did not change in the middle molecular layer of the DG post-TBS compared to pre-TBS. Two-way repeated measures ANOVA comparing time courses of MPP to DG E1, E2, or E2/E1 responses following stratum oriens TBS displayed no significant group (control versus ATRX-KO) or group x time interaction effect (Fig. 21A, B, C). We conclude that control mice displayed no differences in MPP to DG synaptic transmission, whereas ATRX-KO mice had a significant increase in E1 at 115 minutes post-TBS compared to baseline. In general, this pathway was not found to vary much throughout the time course analysis, and thus served as a control pathway for the investigation of basal dendritic LTP following stratum oriens TBS.

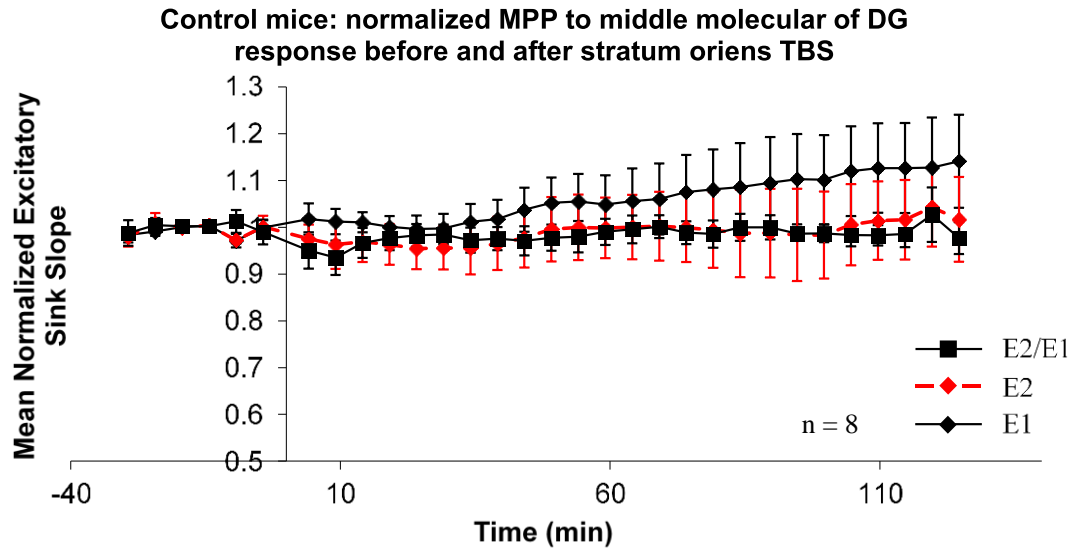


Fig. 19. No change in E1, E2, or E2/E1 of the MPP to DG middle molecular layer response following stratum oriens TBS in control mice.

Mean normalized excitatory sink slope (\pm SEM) (y-axis) in the middle molecular layer of DG as a function of time (x-axis) following MPP stimulation in control mice ($n = 8$). Response following first pulse (E1), second pulse (E2), and ratio (E2/E1) were normalized by their respective baseline mean measure and further averaged across 5 consecutive time points. Responses at 2, 7, 117, and 122 min post-TBS, and -5, -10, -25, -30 min during baseline were not averaged, but were plotted to show a more complete time course. There was no significant difference in E1, E2, or E2/E1 response after stratum oriens TBS compared to baseline (see Results).

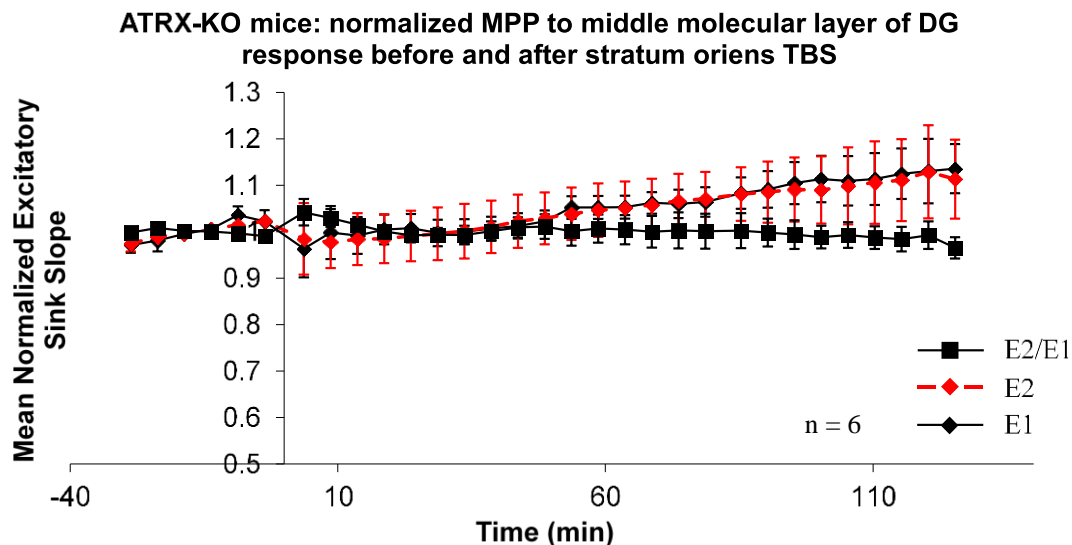


Fig. 20. Significant increase in E1 of MPP to DG middle molecular layer response following stratum oriens TBS in ATRX-KO mice.

Mean normalized excitatory sink slope (\pm SEM) (y-axis) in the middle molecular layer of DG as a function of time (x-axis) following MPP stimulation in ATRX-KO mice ($n = 6$). Response following first pulse (E1), second pulse (E2), and ratio (E2/E1) were normalized by their respective baseline mean measure and further averaged across 5 consecutive time points. Responses at 2, 7, 117, and 122 min post-TBS, and -5, -10, -25, -30 min during baseline were not averaged, but were plotted to show a more complete time course. One-way repeated measures ANOVA indicated a statistically significant increase in E1 ($F_{22,110} = 4.13$, $p < 0.0001$) and E2 response ($F_{22,66} = 2.37$, $p = 0.0038$) relative to baseline following stratum oriens TBS. Newman Keuls multiple post-hoc comparisons revealed that E1 response was significantly larger relative to baseline at 115 min post-TBS whereas E2 response was not different than baseline at any time point post-TBS ($p < 0.05$). Normalized E2/E1 ratio did not change post-TBS compared to baseline. It can be concluded that ATRX-KO mice display a significant increase in E1 middle molecular layer of DG response following stratum oriens TBS.

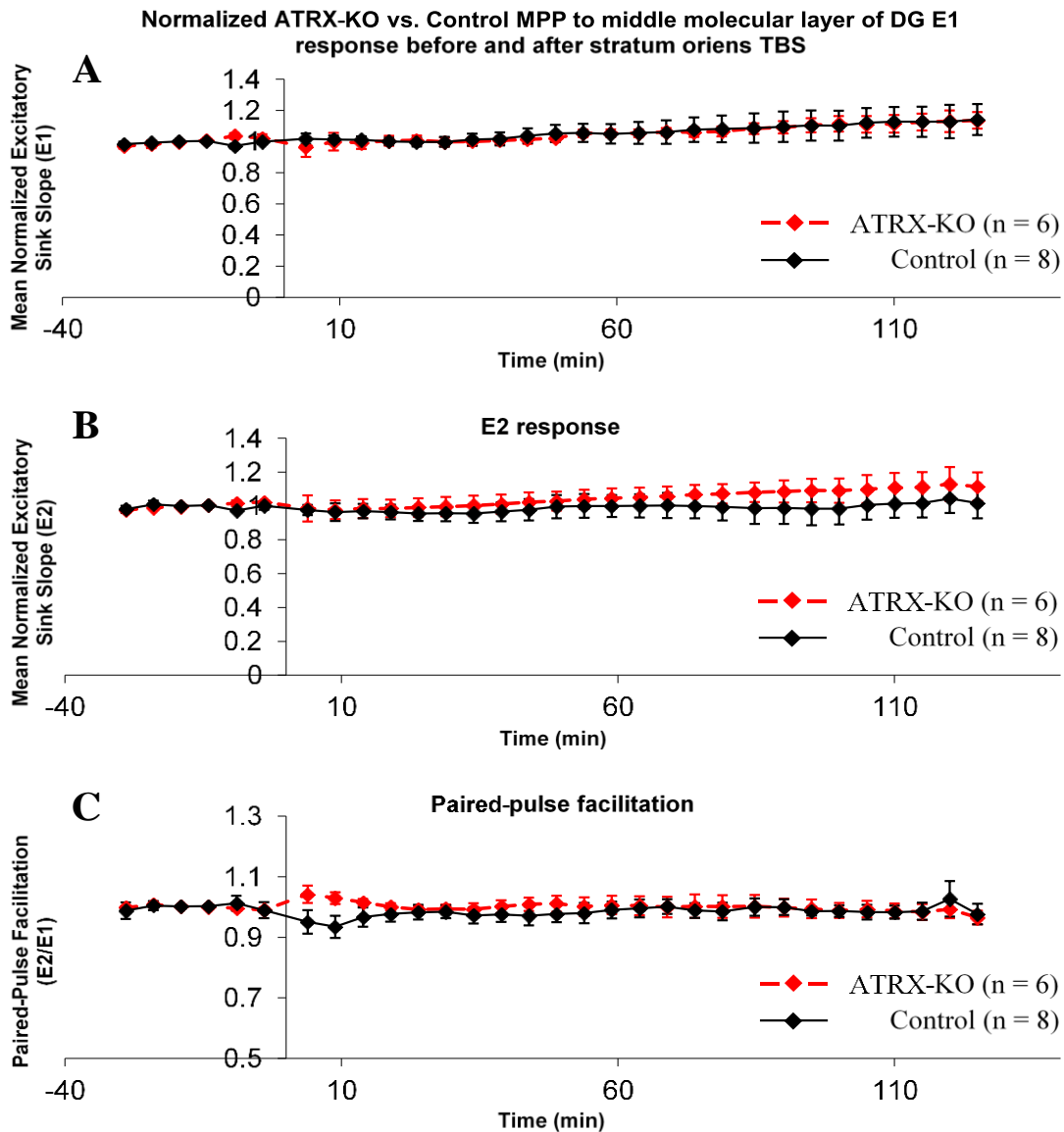


Fig. 21. Normalized MPP to DG middle molecular layer E1, E2, and E2/E1 time courses of ATRX-KO mice compared to control mice.

Mean normalized excitatory sink slope (\pm SEM) (y-axis) in the middle molecular layer of DG as a function of time (x-axis) following MPP stimulation in control ($n = 8$) and ATRX-KO mice ($n = 6$). Response following first pulse (E1), second pulse (E2), and ratio (E2/E1) were normalized by their respective baseline mean measure and further averaged across 5 consecutive time points. **A)** E1 response was not significantly different between control and ATRX-KO mice (two-way repeated measures ANOVA). **B)** Same as (A), but E2 was plotted instead of E1. **C)** Paired-pulse facilitation (E2/E1) plotted with time also showed no difference between groups.

3.2.3 Input-output relation two hours post-TBS: DG excitability may be elevated in ATRX-KO mice

Two hours after stratum oriens TBS, a final I/O curve (IO2) was generated for the DG middle molecular layer sink responses for both control ($n = 8$) and ATRX-KO mice ($n = 6$). Neither control ($n = 8$) nor ATRX-KO mice ($n = 6$) displayed statistically significant paired-pulse facilitation (PPF) in the middle molecular layer of DG following MPP stimulation in IO2 (Fig. 22A, 23A). Comparison of E1 and E2 response between IO1 and IO2 (Fig. 22B, C) in control mice revealed no significant group or group \times intensity interaction effect for either E1 or E2. These findings confirmed that control mice did not experience any significant change in DG middle molecular layer response following MPP stimulation post-OR-TBS. Two-way randomized block ANOVA did, however, display a trend for E1 response being increased in IO2 compared to IO1 ($F_{5,35} = 2.25$, $p = 0.071$) in control mice (Fig. 22B). In ATRX-KO mice, both E1 and E2 response were significantly greater in IO2 compared to IO1 ($p < 0.05$) at stimulus intensities of 2–6 \times T (Fig. 23B) and 3–10 \times T (Fig. 23C), respectively (Newman Keuls multiple post-hoc comparisons following a significant group \times intensity interaction effect in two-way randomized block ANOVA). IO2 of E1 or E2 response indicates saturation of response at lower stimulus intensity in ATRX-KO mice than control mice (Fig. 24A, B), which was similar to IO1. However, two-way repeated measures ANOVA only indicated a trend of a group (control versus ATRX-KO) \times intensity interaction effect for E1 ($F_{6,72} = 2.17$, $p = 0.056$) and E2 ($F_{6,72} = 1.99$, $p = 0.079$). In addition, there was no significant difference in E2/E1 for PPF in IO2 between controls and ATRX-KO mice (Fig. 24C). In conclusion, control and ATRX-KO mice do not display PPF at 2 \times T post-TBS, and the I/O curves confirmed that some potentiation of the MPP to DG middle molecular layer response occurred following stratum oriens TBS in ATRX-KO mice. A trend ($0.05 < p < 0.10$) still indicated that E1 and E2 DG middle molecular layer responses following MPP stimulation in ATRX-KO mice were more excitable than in controls, and there was no longer a significant difference in PPF between groups post-TBS.

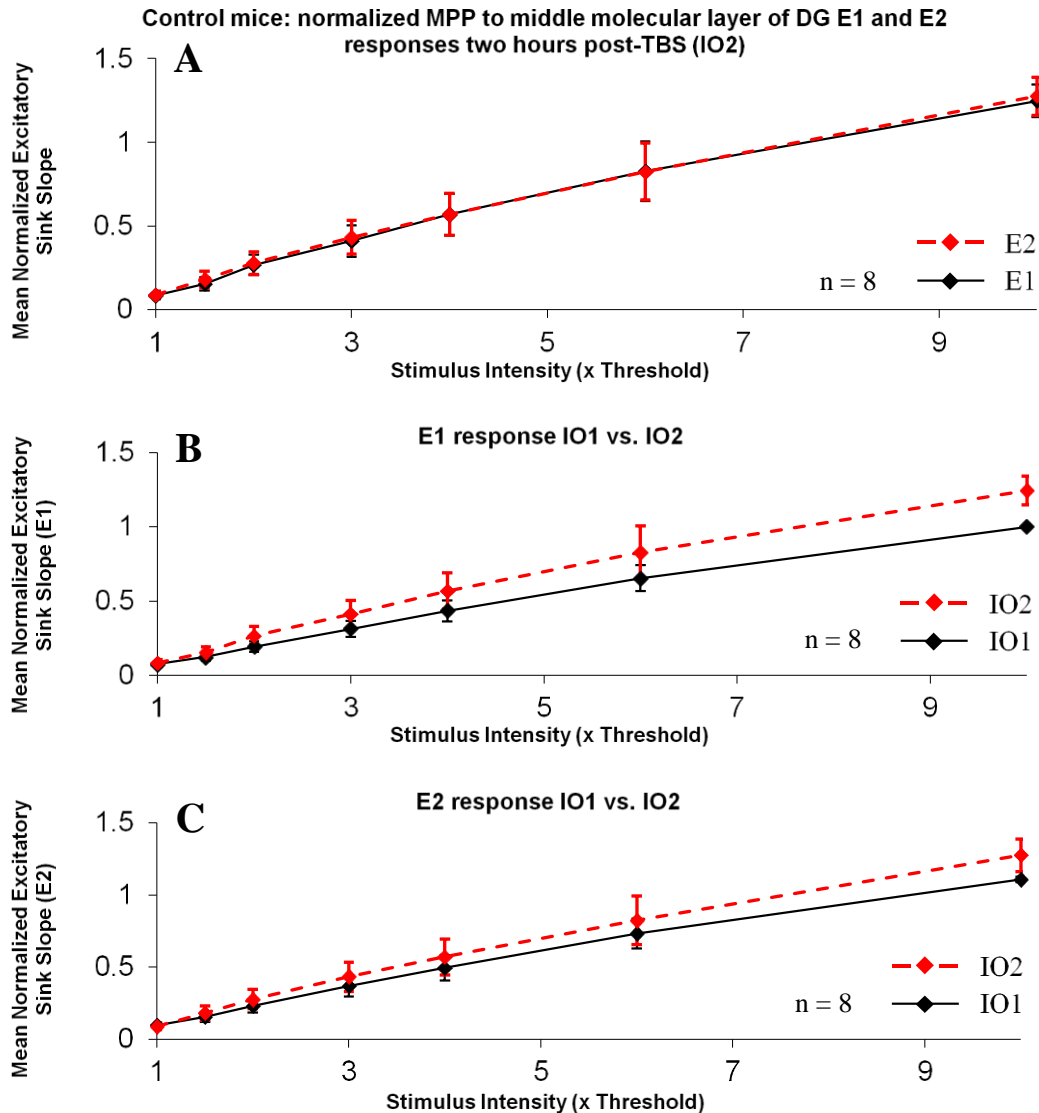


Fig. 22. No PPF or LTP in the MPP to DG middle molecular layer responses following stratum oriens TBS in controls.

Mean normalized excitatory sink slope (\pm SEM) in middle molecular layer of DG following first pulse (E1) and second pulse (E2) of MPP stimulation at increasing intensity (x-axis) two hours post-TBS of stratum oriens (IO2) in control mice (n = 8). **A**) E1 and E2 response as a function of stimulus intensity. Two-way randomized block ANOVA revealed no significant group or group x intensity interaction effect between E1 and E2 responses at increasing stimulus intensity. **B**) E1 response, plotted for baseline (IO1) and IO2, displayed a trend of being increased in IO2 compared to IO1 (see Results). **C**) Same as (B) except E2 responses were plotted displaying no significant differences between IO1 and IO2 (two-way randomized block ANOVA).

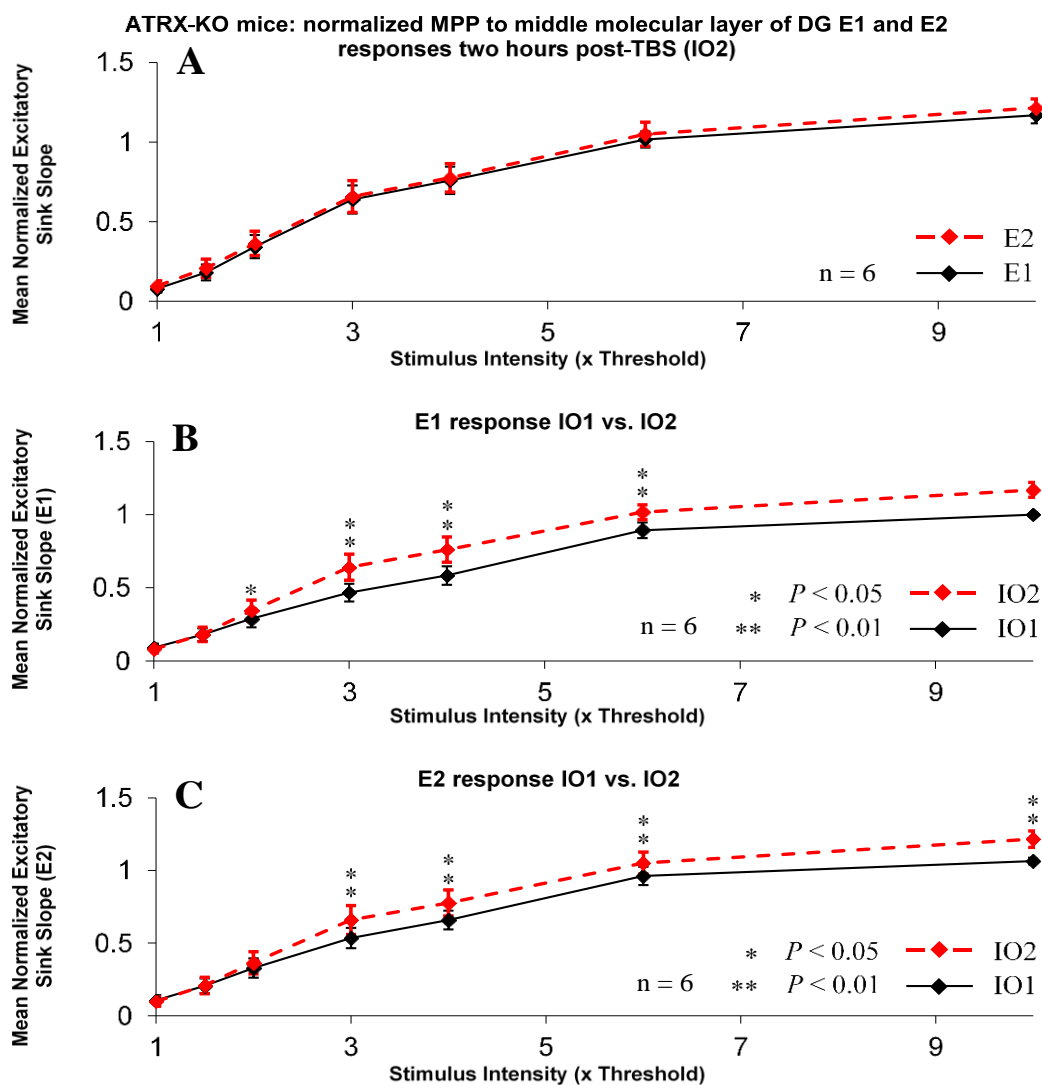


Fig. 23. IO2 vs. IO1 response for ATRX-KO mice indicates potentiation of E1 and E2 of MPP to middle molecular layer responses.

Mean normalized excitatory sink slope (\pm SEM) in middle molecular layer of DG after first pulse (E1) and second pulse (E2) of MPP stimulation at increasing intensity (x-axis) two hours post-TBS of the stratum oriens (IO2) in ATRX-KO mice ($n = 6$). **A**) E1 and E2 response as a function of stimulus intensity, with no significant differences between groups (E1 versus E2) at increasing stimulus intensity. **B**) E1 response plotted for baseline (IO1) and IO2. E1 responses in IO2 were significantly greater than in IO1 at stimulus intensities of 2–6 x T ($p < 0.05$). **C**) Same as (B) except E2 responses were plotted instead of E1. E2 response was significantly larger in IO2 compared to IO1 at 3–10 x T ($p < 0.01$, Newman Keuls post-hoc difference following significant two-way ANOVA).

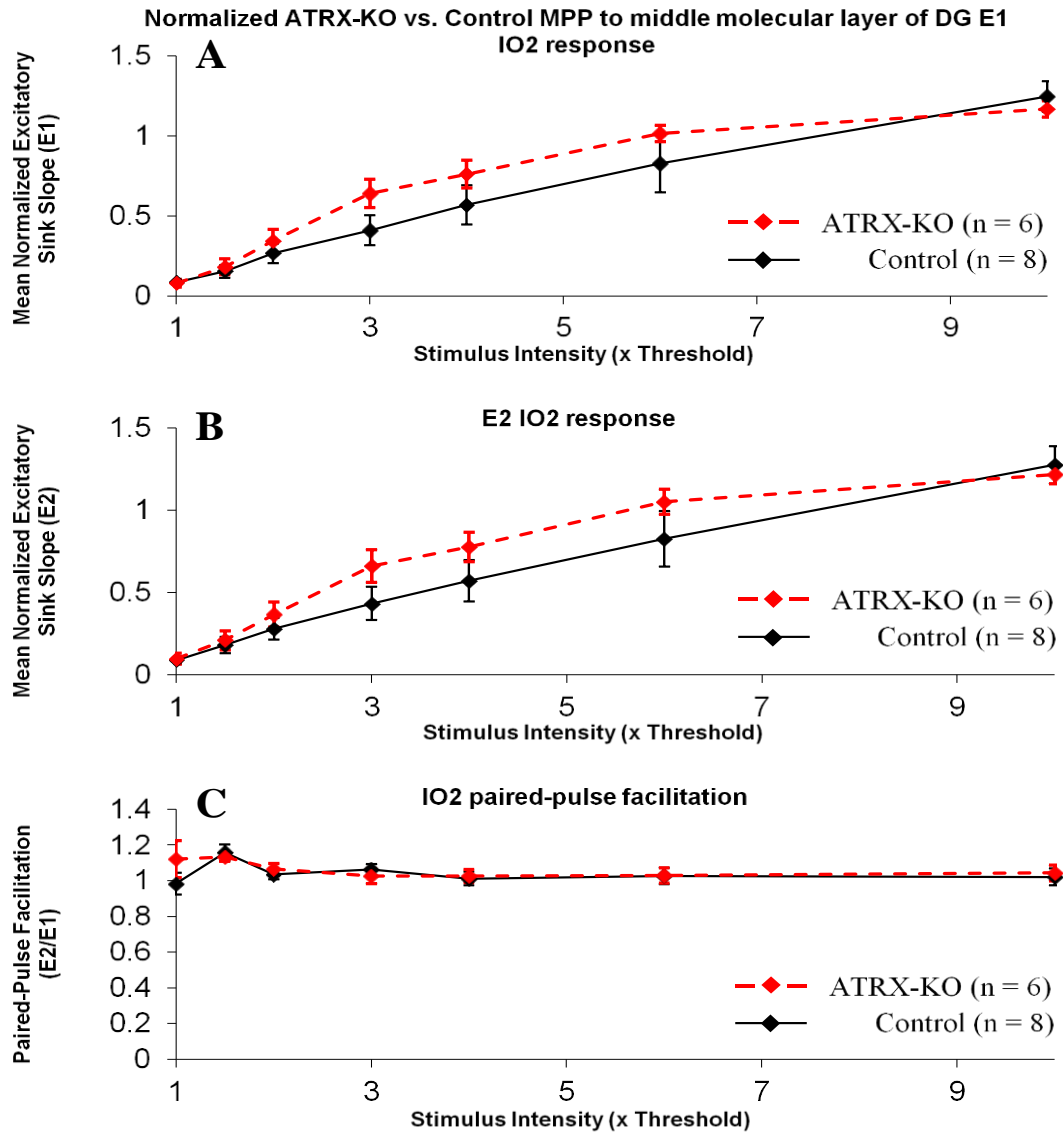


Fig. 24. Trend of increased E1 and E2 DG middle molecular layer excitability following MPP stimulation 2 hours post-OR-TBS in ATRX-KO mice compared to controls.

Mean normalized excitatory sink slope (\pm SEM) in middle molecular layer of DG after first pulse (E1) and second pulse (E2) of MPP stimulation at increasing intensity (x-axis) two hours post-TBS (IO2), as well as paired-pulse facilitation (PPF) in control (n = 8) and ATRX-KO mice (n = 6). **A**) E1 response in IO2 displayed no significant differences between control and ATRX-KO mice (two-way repeated measures ANOVA). However, a trend of increased excitability in E1 response at 3–6 x T in ATRX-KO mice compared to controls was found. **B**) Same as (A) but E2 response was plotted instead of E1 (see Results). **C**) PPF, measured by E2/E1, at increasing MPP stimulus intensity displayed no significant differences between control and ATRX-KO mice.

3.3 MPP stimulation excites the distal apical dendritic CA1 region of hippocampal pyramidal cells

The MPP to distal apical dendritic hippocampal synaptic pathway was the second experimental pathway to be tested in control ($n = 6$) and ATRX-KO mice ($n = 6$) (Fig. 25A). After optimization of the MPP stimulation electrode, threshold intensity of this pathway was found to range between 25–50 μA , with an average threshold intensity of $30 \pm 4.08 \mu\text{A}$ for controls and $35 \pm 5.48 \mu\text{A}$ for ATRX-KO mice, which was not significantly different between groups ($p = 0.48$, t-test). A 50 μm probe was used to record average evoked potentials (AEPs) in the distal apical dendrites of CA1 following paired-pulse stimulation of MPP at 2 x threshold (T) intensity. CSD analysis yielded a distal apical dendritic excitatory sink at SLM and corresponding sources in the stratum radiatum (RAD). This profile of RAD-source and SLM-sink did not change with time, but the whole profile, both sources and sinks, was increased after TBS of MPP (Fig. 25A Depth Profile). The CA3 stratum radiatum, confirmed by histology (Methods), was stimulated to excite the proximal apical dendritic synapses (via Schaffer collaterals) as a non-tetanized control pathway in control ($n = 2$) and ATRX-KO mice ($n = 3$) (Fig. 25B). AEPs in the proximal apical dendrites of CA1 following paired-pulse stimulation of CA3 at 2 x T were recorded. CSD analysis revealed a RAD excitatory sink following CA3 stimulation and a corresponding source in the pyramidal cell layer. Normalized responses 2-hours post-MPP-TBS in both control (0.97 ± 0.011) and ATRX-KO mice (1.07 ± 0.12) were similar to baseline, but statistical analysis was not used to verify this due to the low n value in our groups. We were unable to isolate clear short-latency proximal apical dendritic CA1 responses in all mice, thus, reducing the number of mice for analyses. At the CA3 stimulating electrode, the threshold intensity was found to range between 10–50 μA , with an average threshold intensity of $31 \pm 4.85 \mu\text{A}$ for controls and $29.6 \pm 7.19 \mu\text{A}$ for ATRX-KO mice, which was not significantly different between groups ($p = 0.88$, t-test). In general, this pathway was not found to vary much throughout the time course analysis, and thus served as a control pathway for the investigation of distal apical dendritic LTP following MPP TBS.

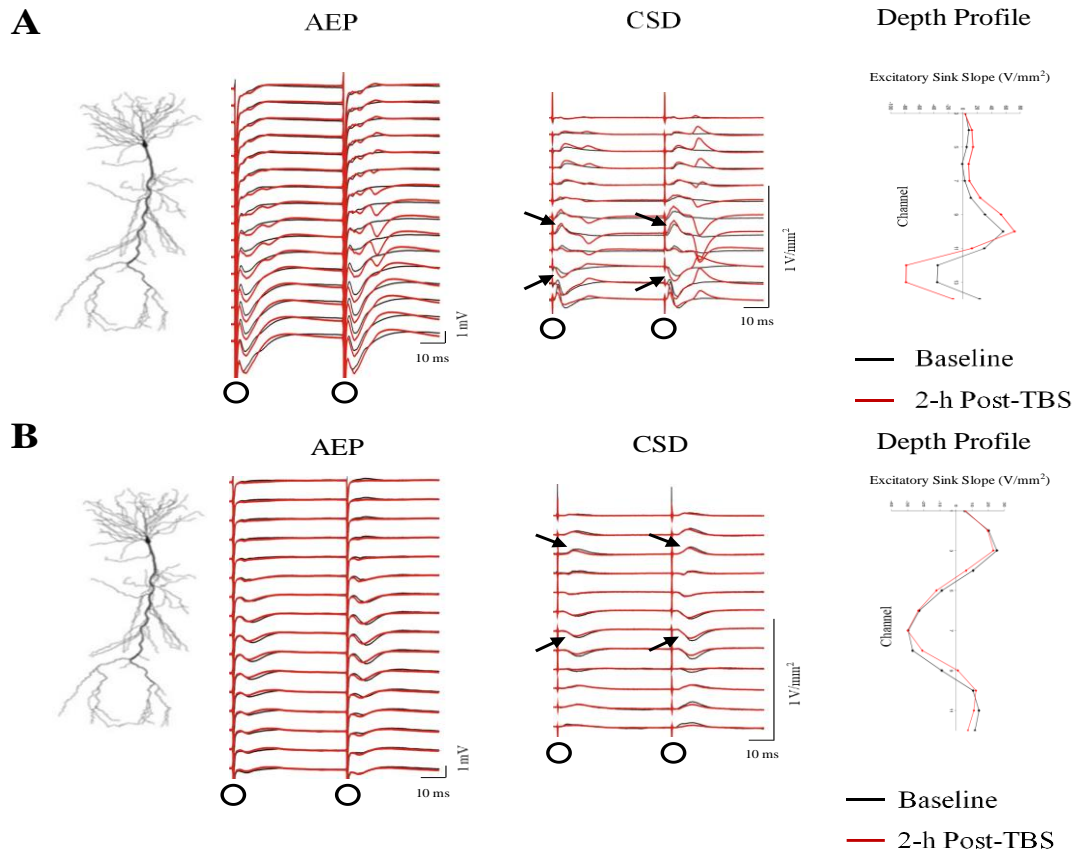


Fig. 25. Representative control mouse displaying distal apical dendritic and proximal apical dendritic excitation in CA1 following MPP and stratum radiatum stimuli, respectively.

A) MPP stimulation was delivered at 50 μA (2 x threshold) stimulus intensity. Schematic pyramidal cell is depicted on the left with basal dendrites projecting upwards from the cell body and apical dendrites projecting downwards. Paired-pulse stimulation (indicated by black circles) of MPP resulted in average evoked potentials (AEP; average of 8 sweeps) across 16 channels of the recording probe, which were analyzed for current source densities (CSDs) in the middle diagram. CSD response as a function of channel depth (3–14) is shown on the right. Current sink (upward black arrow) indicates excitation of the distal apical dendrites of the CA1 pyramidal cells, and current source (downward black arrow) indicates reversal at the CA1 stratum radiatum cell layer. Black traces indicate baseline and red traces display recordings taken 2 hours post-MPP-TBS, showing increased responses after TBS. **B)** Similar to (A), but stratum radiatum was stimulated (50 μA) to excite proximal apical dendrites in CA1 region. Upward arrow corresponds to proximal apical dendritic sink whereas downward arrow corresponds to reversal in CA1 pyramidal cell layer.

3.3.1 Baseline input-output relation: CA1 distal apical dendritic PPF following MPP stimulation is not altered in ATRX-KO mice

Baseline relation between distal apical dendritic excitation and MPP stimulus intensity was studied using input-output (I/O) curves for both control (n = 6) and ATRX-KO mice (n = 6). The excitatory sink slope at the distal apical dendritic CA1 following the first pulse (E1) or the second pulse (E2) was observed to increase gradually with MPP stimulus intensity in control mice (Fig. 26) and in ATRX-KO mice (Fig. 27). Excitatory slopes in each mouse were normalized by the maximal E1 during baseline at 10 x T stimulus intensity. Two-way repeated measures ANOVA comparing control and ATRX-KO distal apical dendritic CA1 response following MPP stimulation at increasing intensity displayed no statistically significant group (control versus ATRX-KO) or group x intensity interaction effect for E1 (Fig. 28A), or E2 response (Fig. 28B). Paired-pulse facilitation (PPF), defined as the E2/E1 ratio, was not significantly different between control and ATRX-KO mice following stimulation of MPP at any intensity (Fig. 28C). We can conclude that both control and ATRX-KO mice feature baseline PPF in the distal apical dendrites of the CA1 region at some MPP stimulus intensities. There were no differences found between groups in E1, E2, or E2/E1 distal apical dendritic response following MPP stimulation during the baseline I/O curve (IO1).

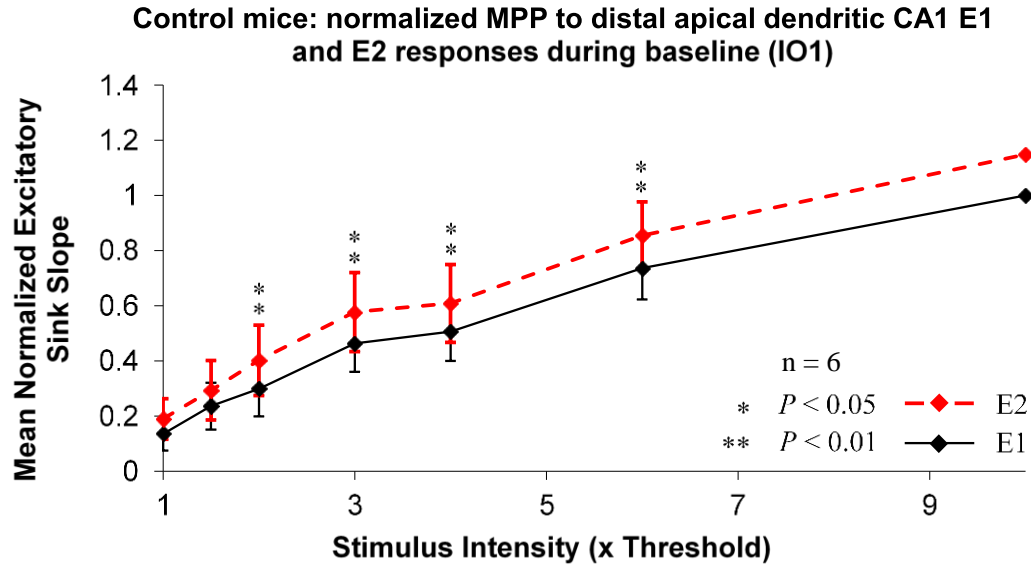


Fig. 26. CA1 distal apical dendritic excitatory sink slopes E1 and E2 following MPP stimulation during baseline (pre-TBS) in control mice.

Mean normalized excitatory sink slope (\pm SEM) (y-axis) in the distal apical dendritic CA1 region following first pulse (E1) and second pulse (E2) of MPP stimulation at increasing intensity (x-axis) in control mice (n = 6). E2 was significantly larger than E1 from 2–6 x T ($p < 0.01$, Newman Keuls post-hoc comparison following a significant group x intensity interaction effect in two-way randomized block ANOVA). 10 x T difference between E1 and E2 was not considered due to normalizing procedure resulting in SEM of 0 for E1 at 10 x T.

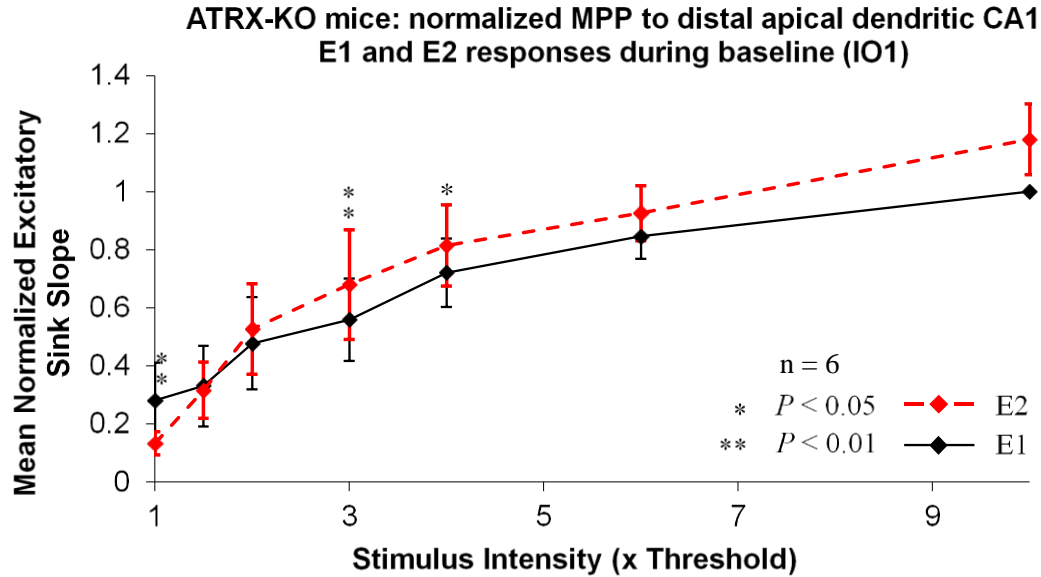


Fig. 27. CA1 distal apical dendritic excitatory sink slopes E1 and E2 following MPP stimulation during baseline (pre-TBS) in ATRX-KO mice.

Mean normalized excitatory sink slope (\pm SEM) (y-axis) in the distal apical dendritic CA1 region following first pulse (E1) and second pulse (E2) of MPP stimulation at increasing intensity (x-axis) in ATRX-KO mice ($n = 6$). There was a significant group (E1 versus E2) \times intensity interaction effect (two-way randomized block ANOVA; $F_{5,25} = 6.01$, $p = 0.0009$) between E1 and E2 responses. Newman Keuls multiple post-hoc comparisons revealed that E2 was significantly larger than E1 at 1 and 3–4 \times T ($p < 0.05$). This confirms paired-pulse facilitation in the distal apical dendritic CA1 region during baseline in ATRX-KO mice at some stimulus intensities, but not at 2 \times T.

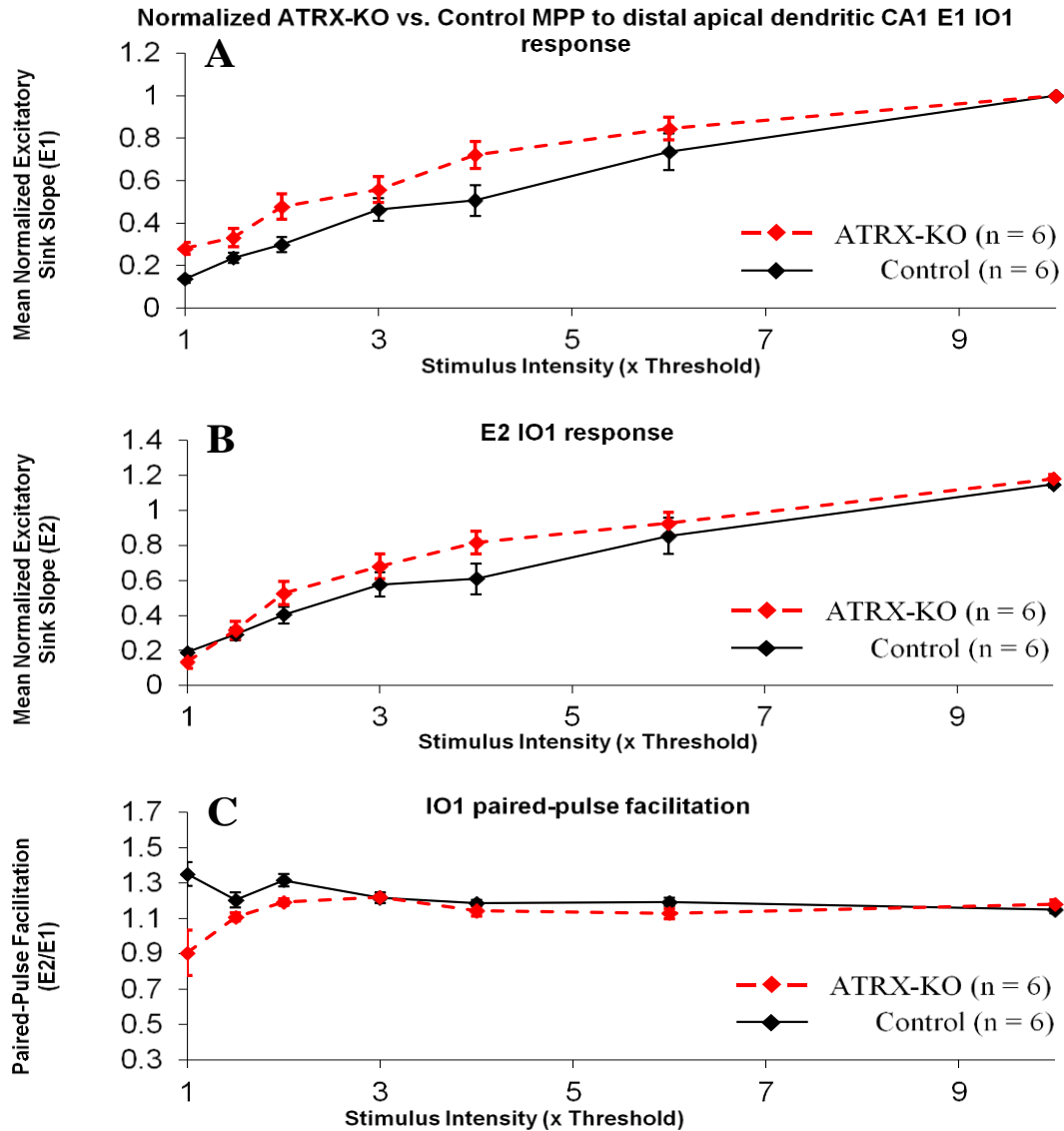


Fig. 28. No significant differences in CA1 distal apical dendritic responses following MPP stimulation, E1, E2, or E2/E1, during baseline (pre-TBS) between control and ATRX-KO mice.

Mean normalized excitatory sink slope (\pm SEM) (y-axis) in the distal apical dendritic CA1 region following first pulse (E1) and second pulse (E2) of MPP stimulation at increasing intensity (x-axis), as well as distal apical dendritic paired-pulse facilitation (PPF) in control (n = 6) and ATRX-KO mice (n = 6). **A**) E1 response in pre-TBS I/O curve (IO1) displayed no significant differences between control and ATRX-KO mice, as verified by two-way repeated measures ANOVA. **B**) Same as (A) but E2 response was plotted instead of E1. **C**) PPF was not significantly different between control and ATRX-KO mice (two-way repeated measures ANOVA).

3.3.2 Time course analysis: Impairment of E1 and E2 distal apical dendritic LTP following MPP TBS in ATRX-KO mice compared to controls

Upon establishing a stable baseline (see Methods), theta-burst stimulation (TBS) was delivered to the MPP at 4 x T to induce LTP in the distal apical dendritic CA1 region of the hippocampus. The length of time taken to establish a stable baseline varied between 30–60 minutes but did not differ between control and ATRX-KO mice. LTP was demonstrated as a long-lasting increase in distal apical dendritic CA1 response following MPP TBS (Fig. 25). For statistical analysis, each measure was averaged from five consecutive time points, and the post-TBS times started at 12 min and ended at 112 min.

Statistically significant temporal changes were found for E1 of control (Fig. 29) and ATRX-KO mice (Fig. 30) (one-way repeated measures ANOVA: $F_{22,110} = 5.92$, $p < 0.0001$ and $F_{22,110} = 2.68$, $p = 0.0004$, respectively), and for E2 ($F_{22,110} = 4.79$, $p < 0.0001$ and $F_{22,110} = 1.94$, $p = 0.014$, respectively). Newman Keuls multiple post-hoc comparisons revealed that control mice displayed statistically significant E1 and E2 LTP relative to baseline measures. Two-way repeated measures ANOVA comparing E1 LTP and E2 LTP between groups (Fig. 31A, B) indicated a significant group x time interaction effect for E1 ($F_{20,200} = 2.44$, $p = 0.0009$) as well as E2 ($F_{20,200} = 1.73$, $p = 0.031$), where ATRX-KO E1 and E2 LTP was significantly impaired compared to controls approximately one-hour post-TBS ($p < 0.05$). There were no significant differences between groups in the time course of distal apical dendritic E2/E1 response following MPP tetanus (Fig. 31C). We conclude that ATRX-KO mice exhibited less robust distal apical dendritic LTP than controls following MPP TBS, as shown by impaired E1 and E2 enhancement compared to controls starting approximately one-hour post-TBS.

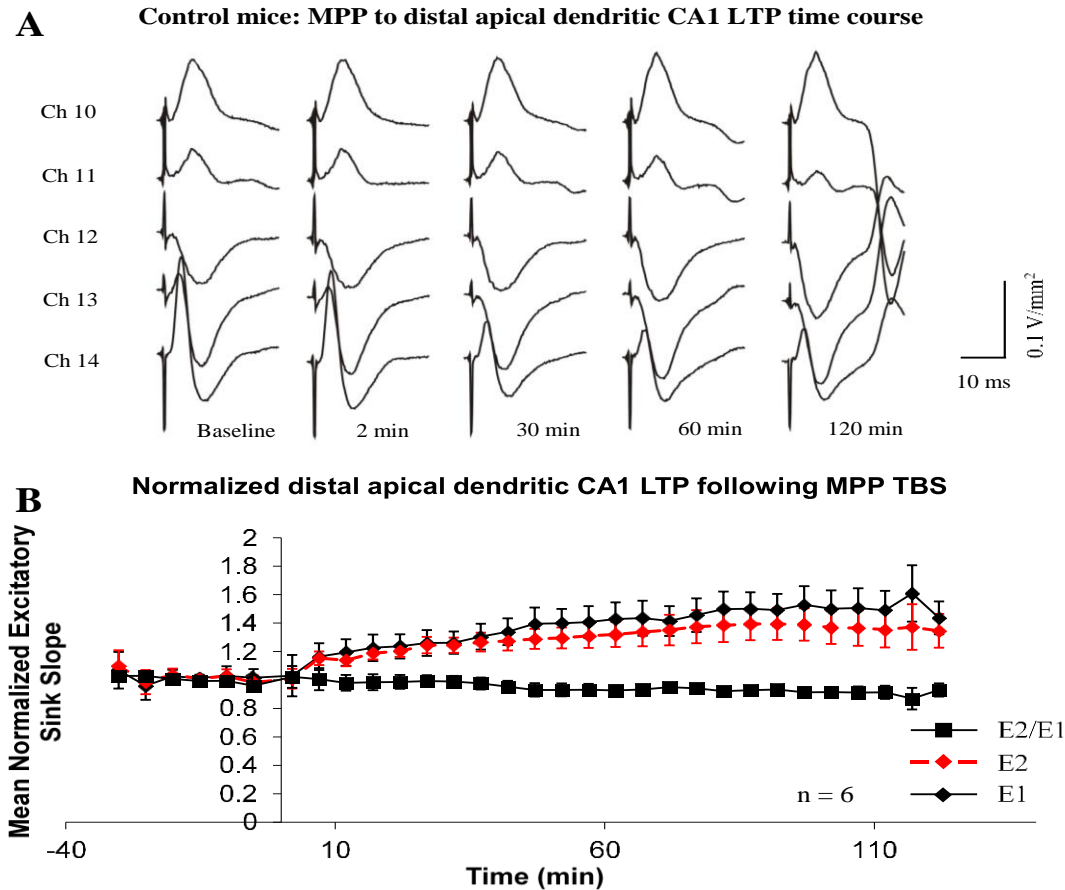


Fig. 29. E1 and E2 distal apical dendritic LTP following MPP tetanus in control mice.

A) Distal apical dendritic CA1 LTP time course following MPP TBS in a representative control mouse. CSD responses of selected channels are displayed for baseline, 2 min, 30 min, 60 min, and 120 min post-TBS. Distal apical dendritic sink (excitation) is shown in Ch 12, with a corresponding source at the stratum radiatum cell layer in Ch 10. **B)** Mean normalized excitatory sink slope (\pm SEM) (y-axis) in the distal apical dendritic CA1 region as a function of time (x-axis) both before and after LTP induction by MPP TBS (time = 0) in control mice (n = 6). Response following first pulse (E1), second pulse (E2), and ratio (E2/E1) were normalized by their respective baseline mean measure and further averaged across 5 consecutive time points, except responses at 2, 7, 117, and 122 min post-TBS, and -5, -10, -25, and -30 min (pre-TBS) were not averaged. One-way repeated measures ANOVA indicated a significant increase in E1 from 47–112 min post-TBS and E2 response from 37–112 min post-TBS relative to baseline ($p < 0.05$, Newman Keuls multiple post-hoc comparisons, see Results). Normalized E2/E1 ratio did not change post-TBS compared to baseline.

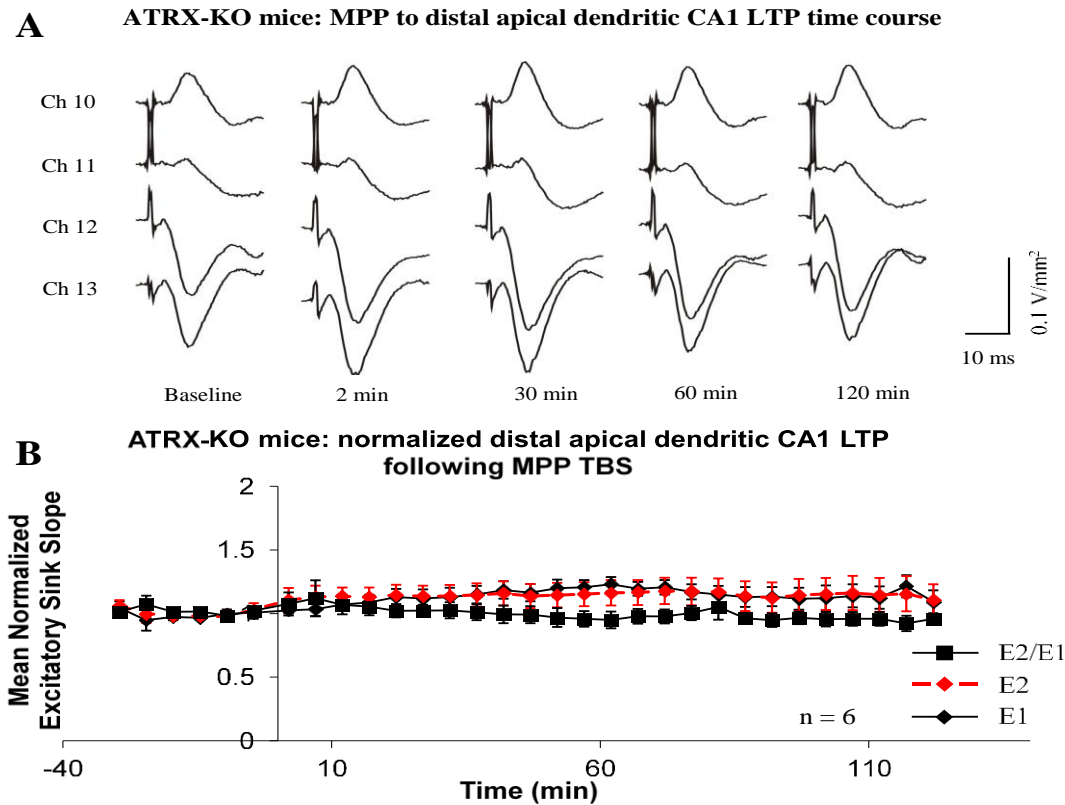


Fig. 30. E1 and E2 distal dendritic LTP at some time points post-TBS in ATRX-KO mice.

A) Distal apical dendritic CA1 LTP time course following MPP TBS in a representative ATRX-KO mouse. CSD responses of selected channels are displayed for baseline, 2 min, 30 min, 60 min, and 120 min post-TBS. Distal apical dendritic sink (excitation) is shown in Ch 13, with a corresponding source at the stratum radiatum cell layer in Ch 10. **B)** Mean normalized excitatory sink slope (\pm SEM) (y-axis) in the distal apical dendritic CA1 region as a function of time (x-axis) both before and after LTP induction by MPP TBS (time = 0) in ATRX-KO mice (n = 6). Response following first pulse (E1), second pulse (E2), and ratio (E2/E1) were normalized by their respective baseline mean measure and further averaged across 5 consecutive time points, except responses at 2, 7, 117, and 122 min post-TBS, and -5, -10, -25, and -30 min (pre-TBS) were not averaged. One-way repeated measures ANOVA indicated a significant increase in E1 at 47 and 52–72 minutes post-MPP-TBS and E2 response at 12–17, 27, 72–82, and 92 minutes post-tetanus relative to baseline ($p < 0.05$, Newman Keuls multiple post-hoc comparisons, see Results). Normalized E2/E1 ratio did not change post-TBS compared to baseline. It can be concluded that ATRX-KO mice exhibited LTP at some time points in the distal apical dendritic CA1 region following MPP tetanus.

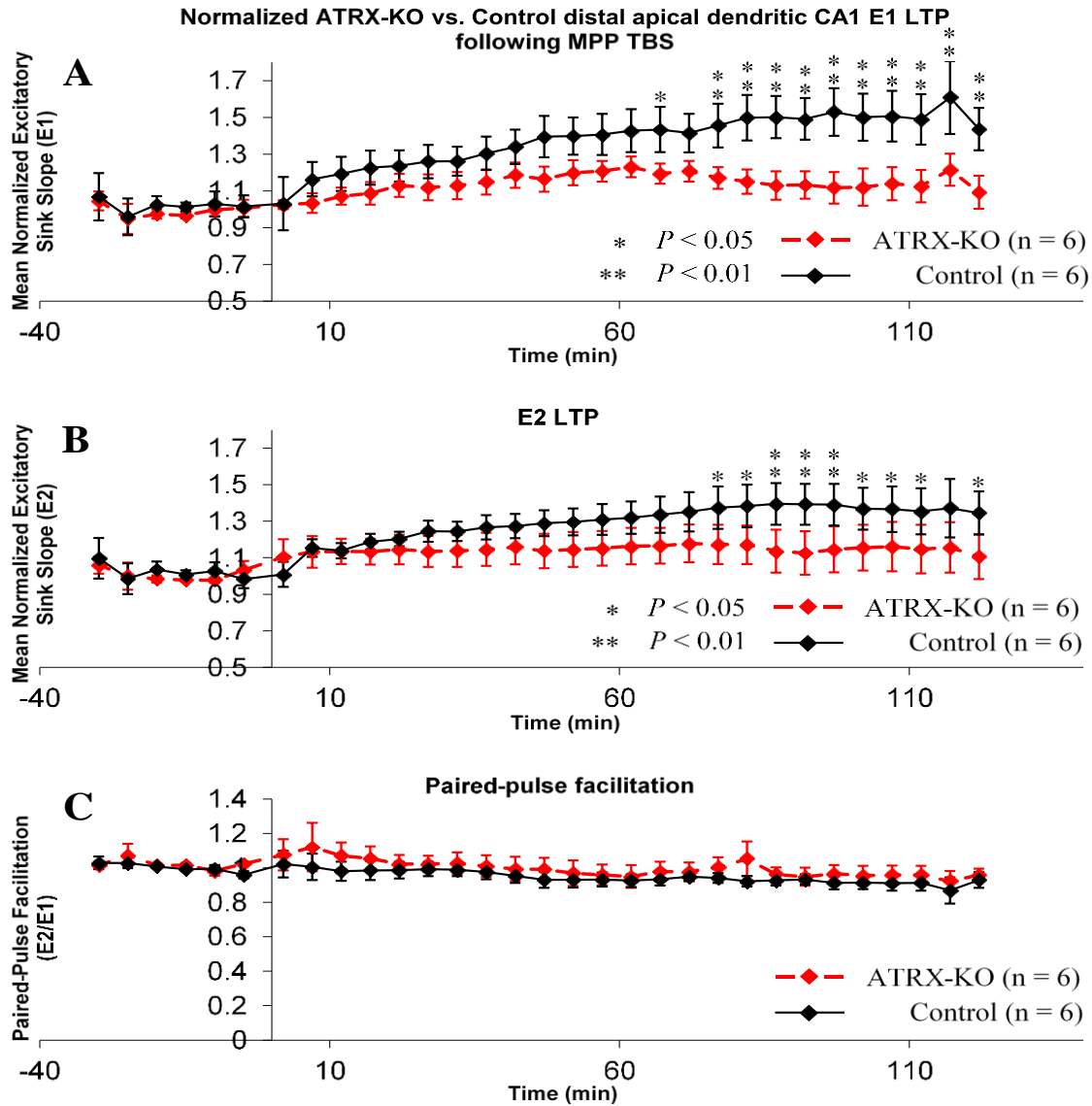


Fig. 31. Impaired distal apical dendritic E1 and E2 LTP following MPP TBS in ATRX-KO mice compared to control mice.

Mean normalized excitatory sink slope (\pm SEM) (y-axis) in the distal apical dendritic CA1 region as a function of time (x-axis) before and after LTP induction by MPP TBS (time = 0) in control (n = 6) and ATRX-KO mice (n = 6). Response following first pulse (E1), second pulse (E2), and ratio (E2/E1) were normalized and averaged (see Methods). **A**) E1 was decreased in ATRX-KO mice compared to control mice from 67–120 min post-TBS ($p < 0.05$, Newman Keuls post-hoc comparison). **B**) Same as (A) but E2 was plotted; E2 was significantly lower in ATRX-KO mice than control mice from 77–120 min post-TBS ($p < 0.05$). **C**) There were no significant differences in PPF between groups.

3.3.3 Input-output relation two hours post-TBS: ATRX-KO mice exhibit deficits in CA1 distal apical dendritic LTP post-MPP-TBS

A final I/O curve (IO2) was generated for the MPP to distal apical dendritic CA1 at 2 hours post-TBS for both control (n = 6) and ATRX-KO mice (n = 6). Like in IO1, control mice (n = 6) displayed statistically significant group (E1 versus E2) x intensity interaction effect for IO2, indicating PPF (E2 > E1) in the distal apical dendrites of CA1 following MPP stimulation two hours post-TBS (Fig. 32A; two-way randomized block ANOVA: $F_{6,30} = 4.38$, $p = 0.0027$). Conversely, ATRX-KO mice (n = 6) no longer displayed a significant difference between E1 and E2 responses during IO2 (Fig. 33A), which was seen during IO1. Comparison of E1 and E2 response between IO1 and IO2 (Fig. 32B, C) in control mice revealed a significant group (IO1 versus IO2) x intensity interaction effect (E1: $F_{5,25} = 6.20$, $p = 0.0007$; E2: $F_{6,30} = 6.45$, $p = 0.0002$), where both E1 and E2 were increased post-TBS compared to baseline, confirming E1 and E2 distal apical dendritic LTP following MPP TBS. ATRX-KO mice did not have any significant differences for E1 or E2 response when IO1 and IO2 were compared (Fig. 33B, C); only a trend of increased response in IO2 compared to IO1 was found for E1 response ($F_{5,25} = 2.44$, $p = 0.062$) and E2 response ($F_{6,30} = 2.07$, $p = 0.087$). This confirms that ATRX-KO mice were impaired in distal apical dendritic E1 and E2 LTP following MPP TBS. Comparisons of E1 and E2 response in IO2 between control and ATRX-KO mice (Fig. 34A, B) suggested that there are no significant group (control versus ATRX-KO) or group x intensity interaction effects (verified by two-way repeated measures ANOVA). ATRX-KO mice, however, did appear to show higher E1 and E2 responses than controls in the distal apical dendritic CA1 region following MPP stimulation at 3–4 x T. Paired-pulse facilitation has been investigated in I/O curves post-TBS and compared between control and ATRX-KO mice (Fig. 34C). No significant differences were observed between groups for distal apical dendritic PPF in IO2. In conclusion, control mice continue to display PPF post-TBS, whereas ATRX-KO mice do not, indicating that MPP TBS may have reduced distal apical dendritic PPF in ATRX-KO mice. Furthermore, robust distal apical dendritic CA1 E1 and E2 LTP has been confirmed by I/O curves for control mice, but not for ATRX-KO mice, supporting that ATRX-KO mice were incapable of achieving the same extent of distal apical dendritic LTP as controls. Lastly, E1, E2, and E2/E1 responses were not found to significantly differ between groups.

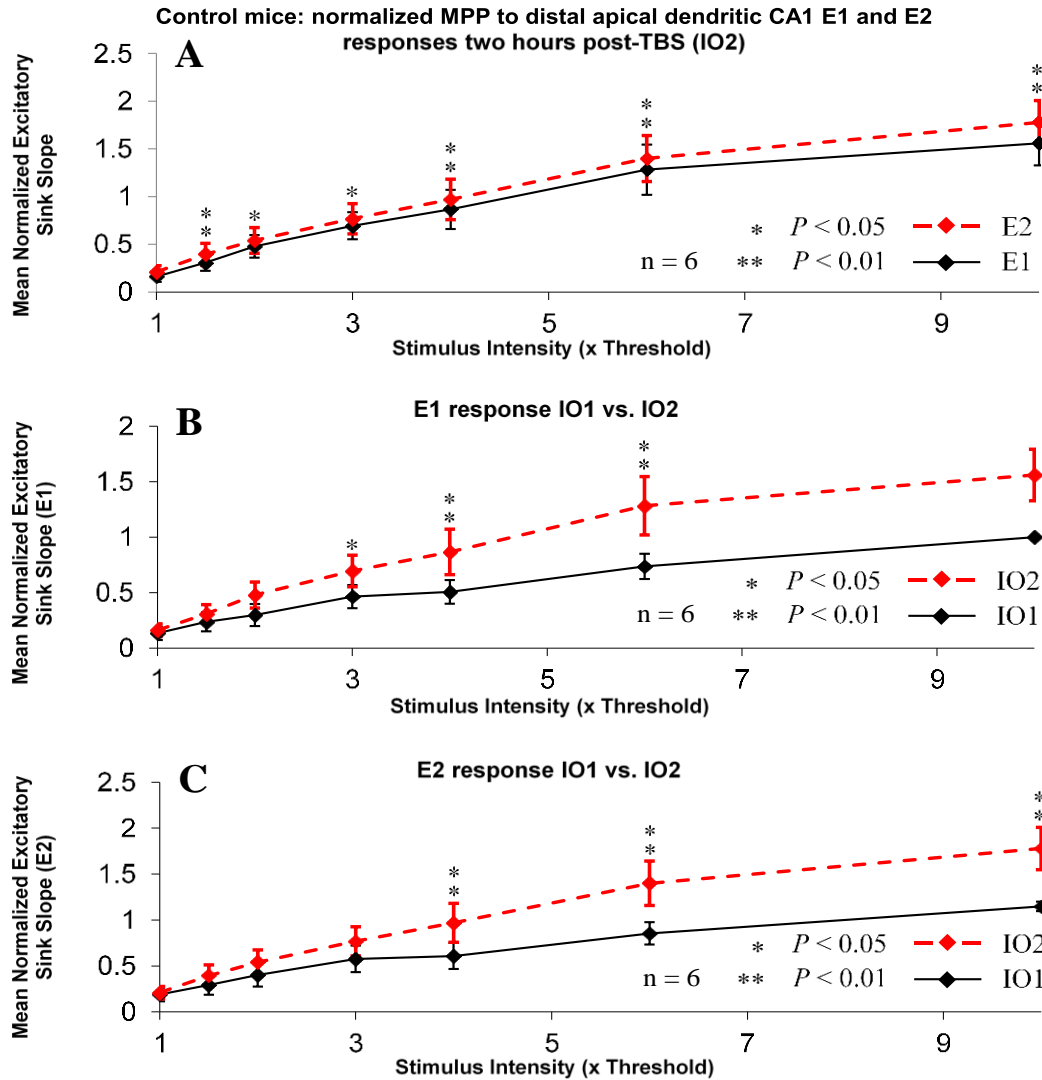


Fig. 32. IO2 response for control mice confirmed LTP in the distal apical dendritic CA1 at different stimulus intensities following MPP TBS.

Mean normalized excitatory sink slope (\pm SEM) in distal apical dendritic CA1 region after first pulse (E1) and second pulse (E2) of MPP stimulation at increasing intensity (x-axis) two hours post-TBS (IO2) in control mice ($n = 6$). **A**) E1 and E2 response as a function of stimulus intensity. E2 was significantly greater than E1 at 1.5–10 x T ($p < 0.05$, Newman Keuls post-hoc comparisons following significant two-way randomized block ANOVA). **B**) E1 response plotted for baseline (IO1) and IO2. E1 responses in IO2 were significantly greater than in IO1 at stimulus intensities of 3–6 x T ($p < 0.05$). **C**) Same as (B) except E2 responses were plotted with significant post-hoc differences after a significant group x intensity interaction effect in two-way ANOVA.

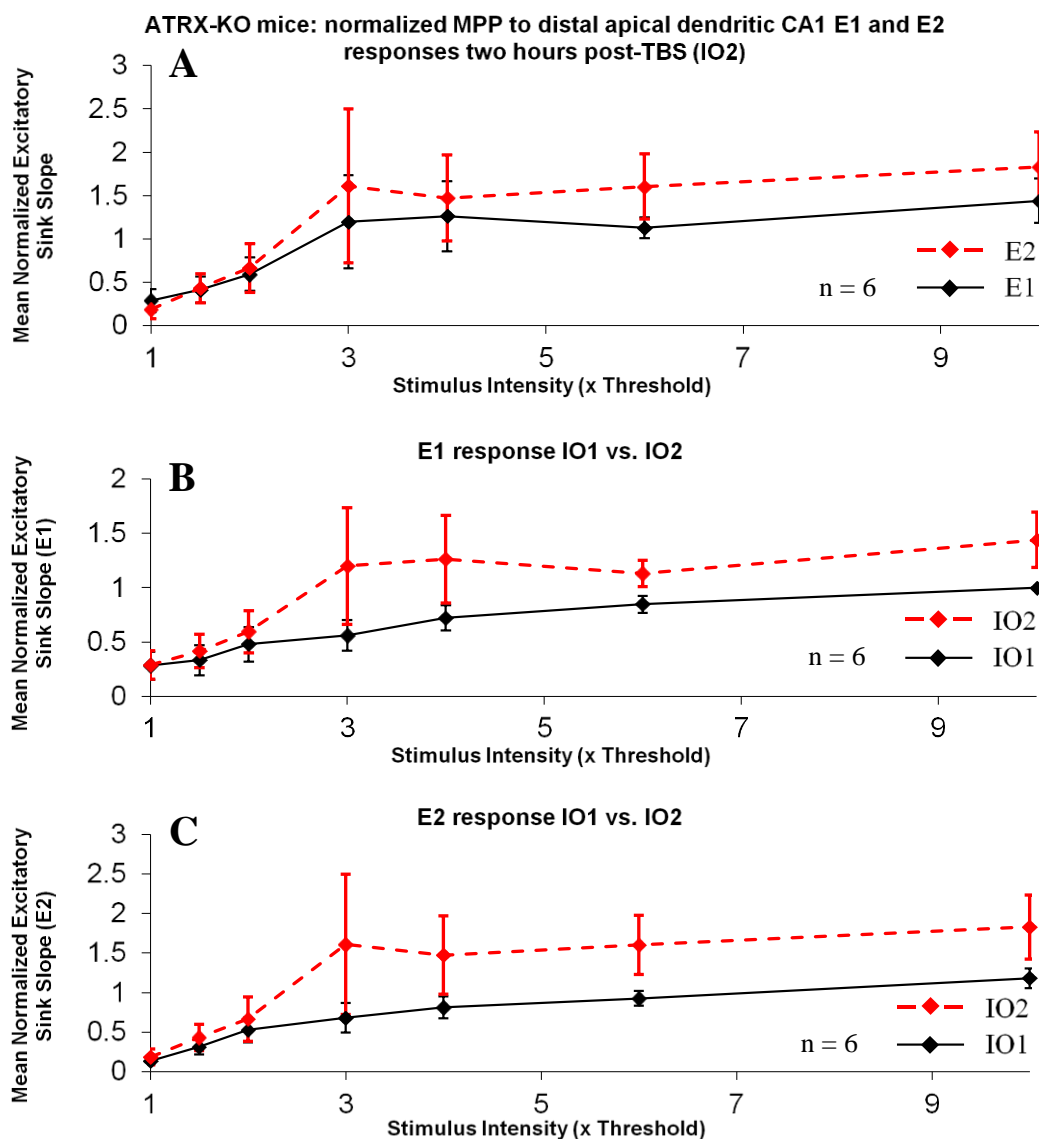


Fig. 33. IO2 response for ATRX-KO mice displays trend of potentiated E1 and E2 responses compared to IO1.

Mean normalized excitatory sink slope (\pm SEM) in distal apical dendritic CA1 region after first pulse (E1) and second pulse (E2) of MPP stimulation at increasing intensity (x-axis) two hours post-TBS (IO2) in ATRX-KO mice ($n = 6$). **A**) E1 and E2 response as a function of stimulus intensity. There were no differences between E1 and E2 response in IO2 (two-way randomized block ANOVA). **B**) E1 response plotted for baseline (IO1) and IO2. E1 responses in IO2 were not significantly different than in IO1 (two-way randomized block ANOVA, see Results). **C**) Same as (B) except E2 responses were plotted with no significant differences in E2 response between IO1 and IO2 (see Results).

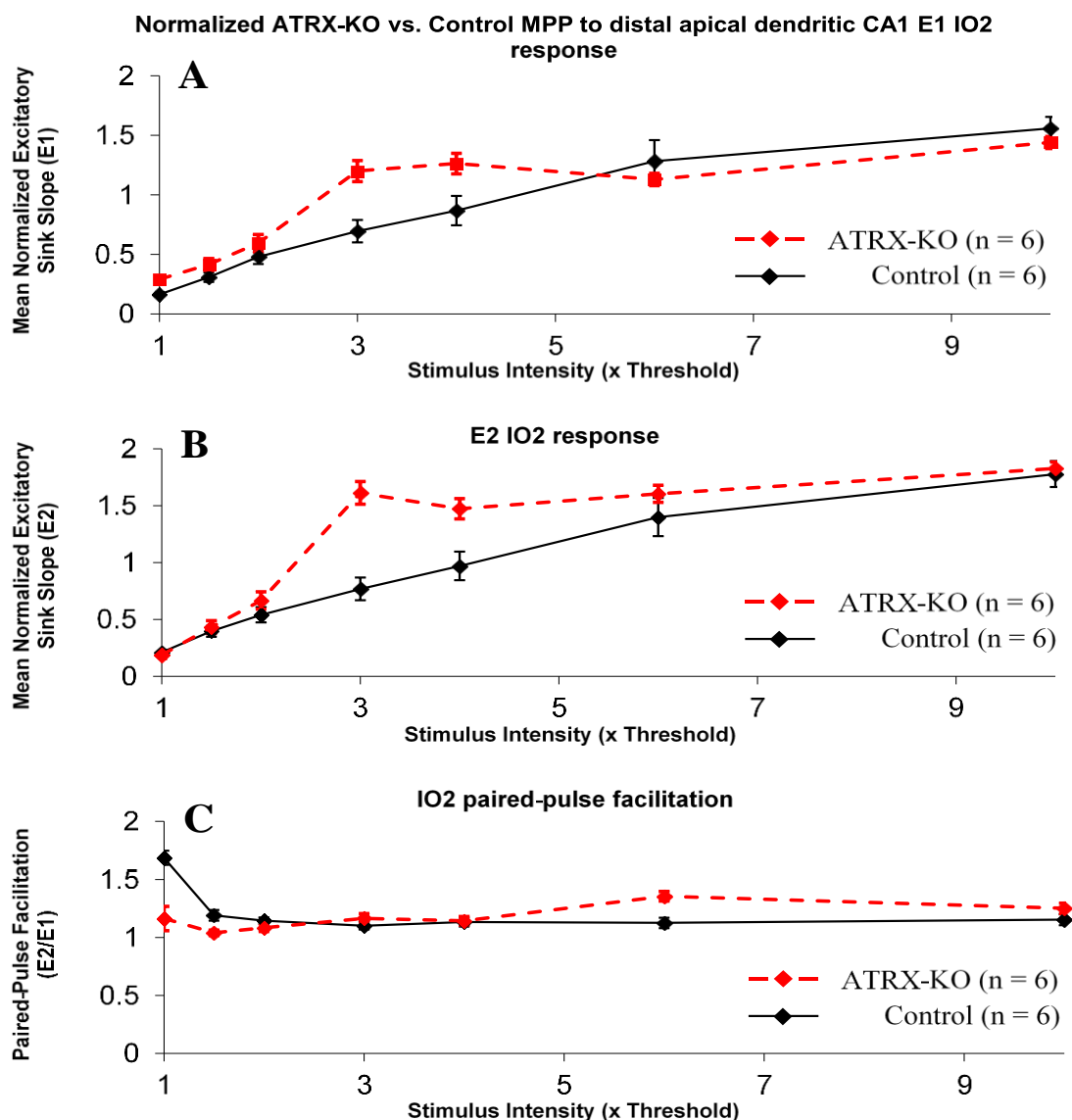


Fig. 34. No significant differences between control and ATRX-KO mice in E1, E2, or E2/E1 response in IO2.

Mean normalized excitatory sink slope (\pm SEM) in distal apical dendritic CA1 region after first pulse (E1) and second pulse (E2) of MPP stimulation at increasing intensity (x-axis) two hours post-TBS (IO2), as well as distal apical dendritic paired-pulse facilitation (PPF) in control (n = 6) and ATRX-KO mice (n = 6). **A**) E1 response in IO2 displayed no significant differences between control and ATRX-KO mice, as shown by two-way repeated measures ANOVA (see Results). **B**) Same as (A) but E2 response was plotted instead of E1. **C**) PPF, measured by E2/E1, at increasing MPP stimulus intensity displayed no significant group or group x intensity interaction effect between control and ATRX-KO mice (two-way repeated measures ANOVA).

3.4 MPP stimulation produces long-latency excitation in the proximal apical dendritic CA1 region of hippocampal pyramidal cells

Stimulation of MPP, in some instances, caused a long-latency (>10 ms onset) proximal apical dendritic CA1 region excitation (Fig. 35), presumably excited by the MPP-DG-CA3-CA1 trisynaptic circuit, in addition to distal apical dendritic CA1 excitation. As a result, control (n = 3) and ATRX-KO mice (n = 3) which displayed both responses were analyzed separately for long-latency proximal apical dendritic CA1 LTP following MPP TBS. All electrode and recording probe locations remained identical to the MPP to distal apical dendritic experiments performed above. Average evoked potentials (AEPs) were recorded from the long-latency proximal apical dendritic sink in CA1 following paired-pulse stimulation (PPS) of MPP at 2 x MPP to distal apical dendritic-threshold intensity. CSD analysis yielded long-latency proximal apical dendritic excitatory sinks and corresponding sources in the CA1 pyramidal cell layer.

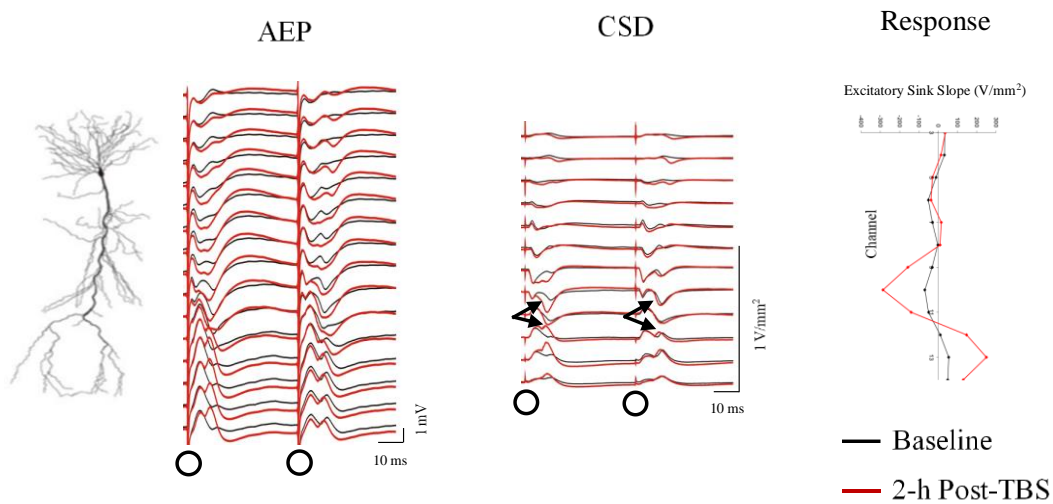


Fig. 35. Representative control mouse displaying long-latency excitation of the proximal apical dendrites of CA1 following MPP stimulation.

MPP stimulation was delivered at $40 \mu\text{A}$ ($2 \times$ threshold) stimulus intensity. Schematic pyramidal cell is depicted on the left with basal dendrites projecting upwards from the cell body and apical dendrites projecting downwards. Paired-pulse stimulation (indicated by black circles) of MPP resulted in average evoked potentials (AEP; average of 8 sweeps) across 16 channels of the recording probe, which were analyzed for current source densities (CSDs) in the middle diagram. CSD response as a function of channel depth (3–14) is shown on the right. Current sink (upward black arrow) indicates long-latency excitation of the proximal apical dendrites of the CA1 pyramidal cells, and current source (downward black arrow) indicates reversal at the CA1 stratum lacunosum moleculare cell layer. Black traces indicate baseline and red traces display recordings taken 2 hours post-MPP-TBS, showing increased responses after TBS.

3.4.1 Baseline input-output relation: ATRX-KO mice display baseline PPD rather than PPF at high stimulus intensities

Baseline relation between long-latency proximal apical dendritic excitation and MPP stimulus intensity was studied using input-output (I/O) curves for both control ($n = 3$) and ATRX-KO mice ($n = 3$). The excitatory sink amplitude at the proximal apical dendritic CA1 following the first pulse (A1) or the second pulse (A2) was observed to increase gradually with MPP stimulus intensity in control mice (Fig. 36) and in ATRX-KO mice (Fig. 37). Excitatory amplitudes in each mouse were normalized by the maximal A1 during baseline at $10 \times T$ stimulus intensity. Preliminary data comparing control and ATRX-KO long-latency proximal apical dendritic CA1 response following MPP stimulation at increasing intensity displayed no statistically significant group (control versus ATRX-KO) or group \times intensity interaction effect for A1 (Fig. 38A), or A2 response (Fig. 38B) (two-way randomized block ANOVA). However, control mice displayed signs of paired-pulse facilitation (PPF; $A2 > A1$) whereas ATRX-KO mice exhibited the opposite phenomenon, paired-pulse depression (PPD; $A2 < A1$). Although PPF was not significantly different between control and ATRX-KO mice following stimulation of MPP at any intensity (Fig. 38C), a trend of group effect was discovered ($F_{1,4} = 5.75, p = 0.075$), suggesting that ATRX-KO mice display PPD (PPF ratio < 1) whereas controls display PPF (PPF ratio > 1) at high stimulus intensities ($>3 \times T$) during IO1.

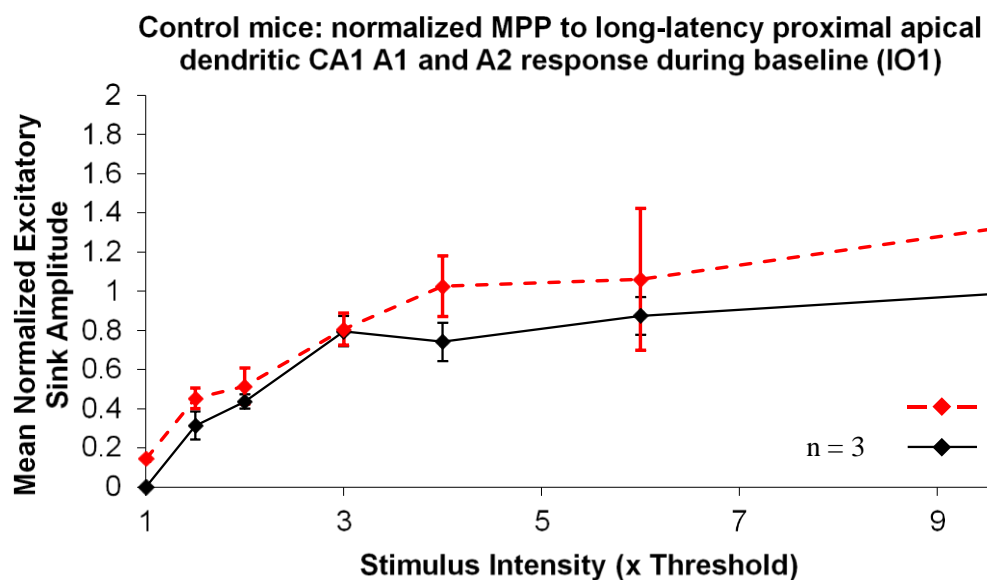


Fig. 36. No significant difference in pre-TBS long-latency proximal apical dendritic A1 and A2 response following MPP stimulation in controls.

Preliminary data displaying mean normalized excitatory sink amplitude (\pm SEM) (y-axis) in the proximal apical dendritic CA1 region following first pulse (A1) and second pulse (A2) of MPP stimulation at increasing intensity (x-axis) in control mice ($n = 3$). A1 and A2 responses were not significantly different during baseline (two-way randomized block ANOVA, see Results). 10 x T difference between A1 and A2 was not considered due to normalizing procedure resulting in SEM of 0 for A1 at 10 x T.

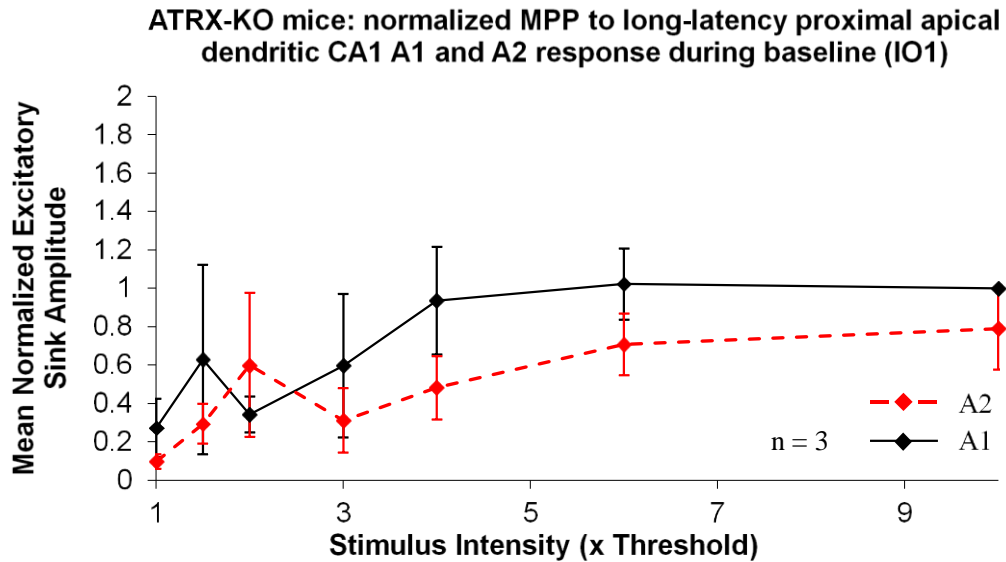


Fig. 37. No significant difference in pre-TBS long-latency proximal apical dendritic A1 and A2 response following MPP stimulation in ATRX-KO mice.

Preliminary data displaying mean normalized excitatory sink amplitude (\pm SEM) (y-axis) in the proximal apical dendritic CA1 region following first pulse (A1) and second pulse (A2) of MPP stimulation at increasing intensity (x-axis) in ATRX-KO mice ($n = 3$). A1 and A2 responses were not significantly different during baseline (two-way randomized block ANOVA, see Results).

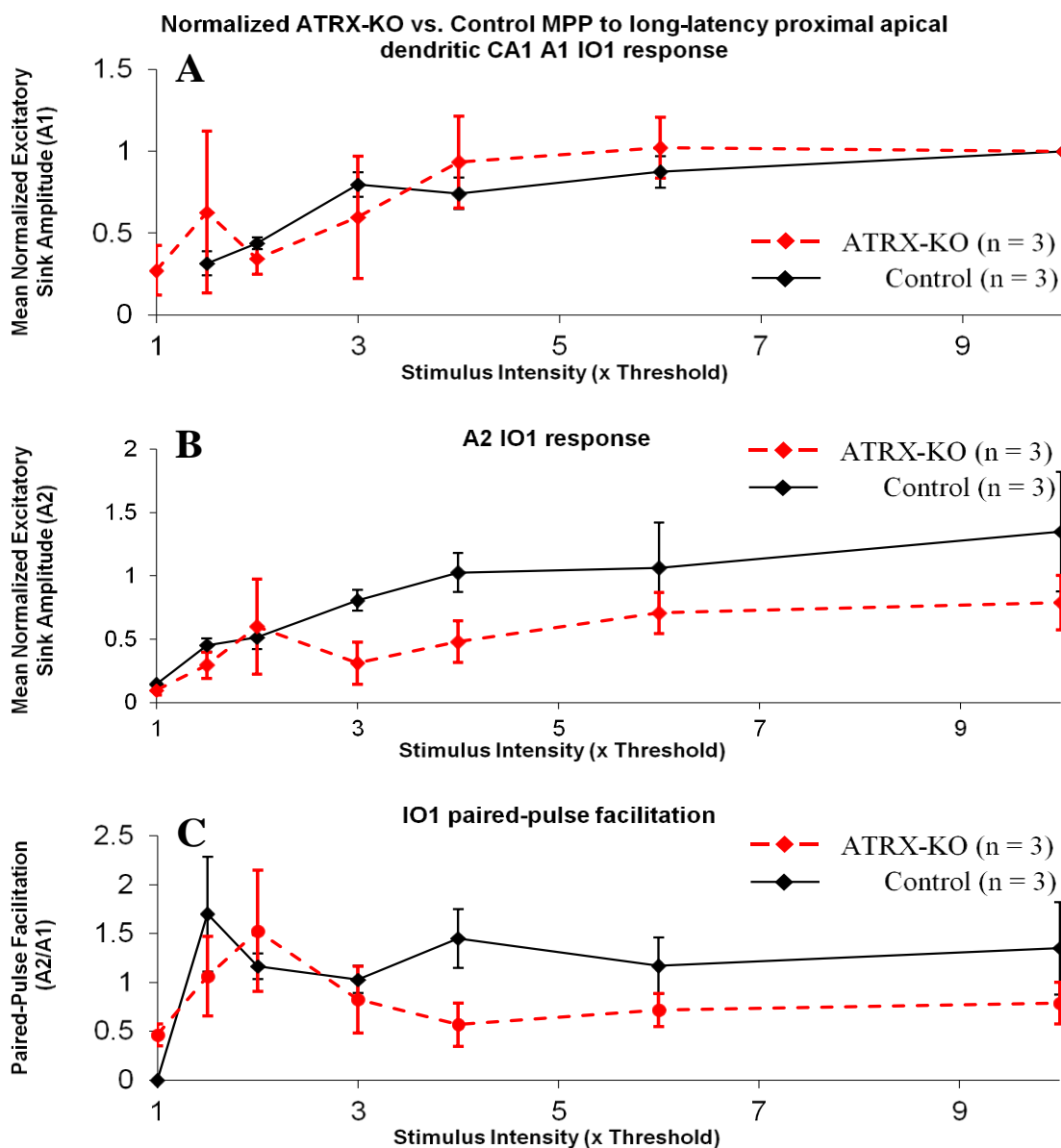


Fig. 38. No significant differences in A1, A2, or A2/A1 pre-TBS long-latency proximal apical dendritic responses post-MPP stimulation between control and ATRX-KO mice.

Preliminary data displaying mean normalized excitatory sink amplitude (\pm SEM) (y-axis) in the proximal apical dendritic CA1 region following first pulse (A1) and second pulse (A2) of MPP stimulation at increasing intensity (x-axis), as well as proximal apical dendritic paired-pulse facilitation (PPF) in control (n = 3) and ATRX-KO mice (n = 3). **A**) A1 response in pre-TBS I/O curve (IO1) was not different between control and ATRX-KO mice (two-way repeated measures ANOVA). **B**) Same findings as (A), but for A2 response. **C**) Group effect trend of long-latency proximal apical dendritic PPF < 1 in ATRX-KO mice was found (see Results).

3.4.2 Time course analysis: ATRX-KO mice are impaired compared to controls in long-latency proximal apical dendritic CA1 LTP following MPP TBS

LTP was demonstrated as an increase in long-latency proximal apical dendritic CA1 response two hours post-MPP-TBS (Fig. 35). For statistical analysis, each measure was averaged from five consecutive time points, and the post-TBS times started at 12 min and ended at 112 min. Statistically significant changes were found for A1 of control (Fig. 39; one-way repeated measures ANOVA: $F_{22,44} = 15.83$, $p < 0.0001$) and A2 of ATRX-KO mice (Fig. 40; $F_{22,44} = 2.17$, $p = 0.014$). Furthermore, two-way repeated measures ANOVA comparing A1 LTP and A2 LTP between groups (Fig. 41A, B) indicated a significant group (control versus ATRX-KO) x time interaction effect for A1 ($F_{20,80} = 3.39$, $p < 0.0001$) and for A2 ($F_{20,80} = 1.94$, $p = 0.020$), where ATRX-KO A1 and A2 LTP was significantly impaired compared to controls at multiple time points post-MPP-TBS. There were no significant differences in normalized A2/A1 long-latency proximal apical dendritic response following MPP TBS between groups (Fig. 41C), but a trend indicating increased PPF in ATRX-KO compared to controls was discovered ($F_{1,4} = 5.29$, $p = 0.083$). We conclude that ATRX-KO mice displayed impaired long-latency proximal apical dendritic A1 LTP compared to controls from approximately one-hour post-TBS onwards. There was no significant difference between controls and ATRX-KO mice in A2 LTP. ATRX-KO mice are deficient in mechanisms that are required to sustain LTP for longer than one hour in the trisynaptic circuit.

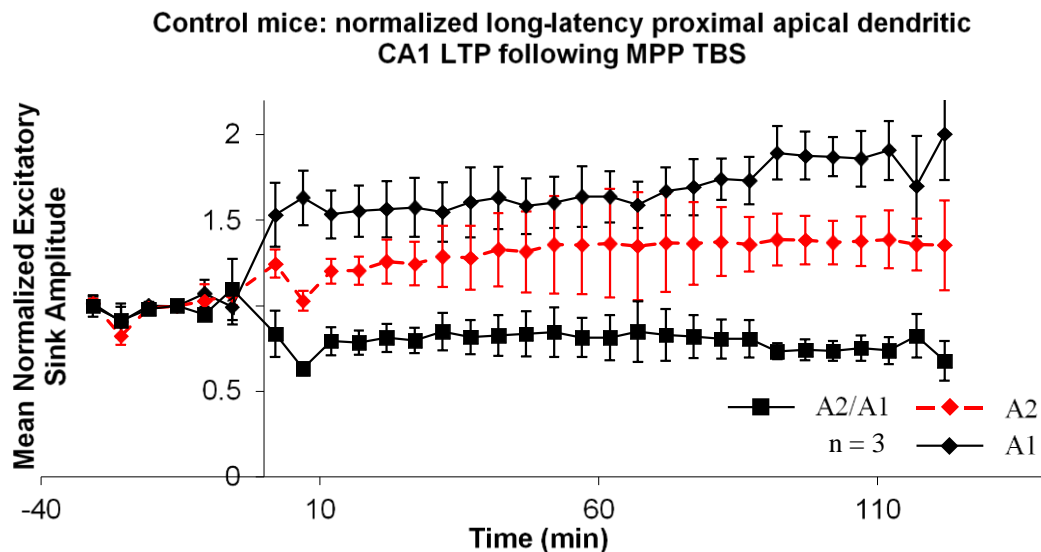


Fig. 39. Time courses of long-latency proximal apical dendritic sinks A1, A2, and A2/A1 following MPP TBS in controls mice.

Preliminary data displaying mean normalized excitatory sink amplitude (\pm SEM) (y-axis) in the proximal apical dendritic CA1 region (A1, A2 and A2/A1) as a function of time (x-axis) both before and after LTP induction by MPP TBS (time = 0) in control mice ($n = 3$). Response following first pulse (A1), second pulse (A2), and ratio (A2/A1) were normalized by their respective baseline mean measure and further averaged across 5 consecutive time points, except responses at 2, 7, 117, and 122 min post-TBS and -5, -10, -25, -30 min pre-TBS represent non-averaged responses. One-way repeated measures ANOVA indicated a significant increase in A1 response from 12–112 min post-TBS ($p < 0.05$, Newman Keuls multiple post-hoc comparisons, see Results), but no significant difference in A2 response post-TBS relative to baseline. Normalized A2/A1 ratio did not change post-TBS compared to baseline.

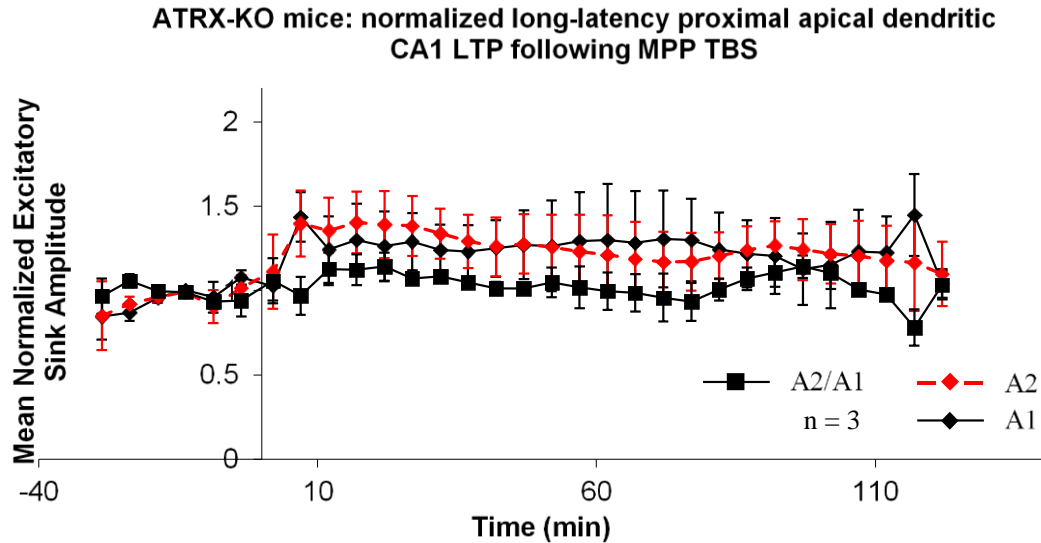


Fig. 40. Time course of long-latency proximal apical dendritic sinks A1, A2, and A2/A1 following MPP TBS in ATRX-KO mice.

Preliminary data displaying mean normalized excitatory sink amplitude (\pm SEM) (y-axis) in the proximal apical dendritic CA1 region as a function of time (x-axis) both before and after LTP induction by MPP TBS (time = 0) in ATRX-KO mice ($n = 3$). Response following first pulse (A1), second pulse (A2), and ratio (A2/A1) were normalized by their respective baseline mean measure and further averaged across 5 consecutive time points, except responses at 2, 7, 117, and 122 min post-TBS and -5, -10, -25, -30 min pre-TBS were not averaged. One-way repeated measures ANOVA indicated a significant increase in A2 response 27–32 min post-MPP-TBS ($p < 0.05$, Newman Keuls multiple post-hoc comparisons, see Results), with no significant change in A1 response. Normalized A2/A1 ratio did not change post-TBS compared to baseline. ATRX-KO mice exhibit A2 LTP at some time points in the proximal apical dendritic CA1 region following MPP TBS.

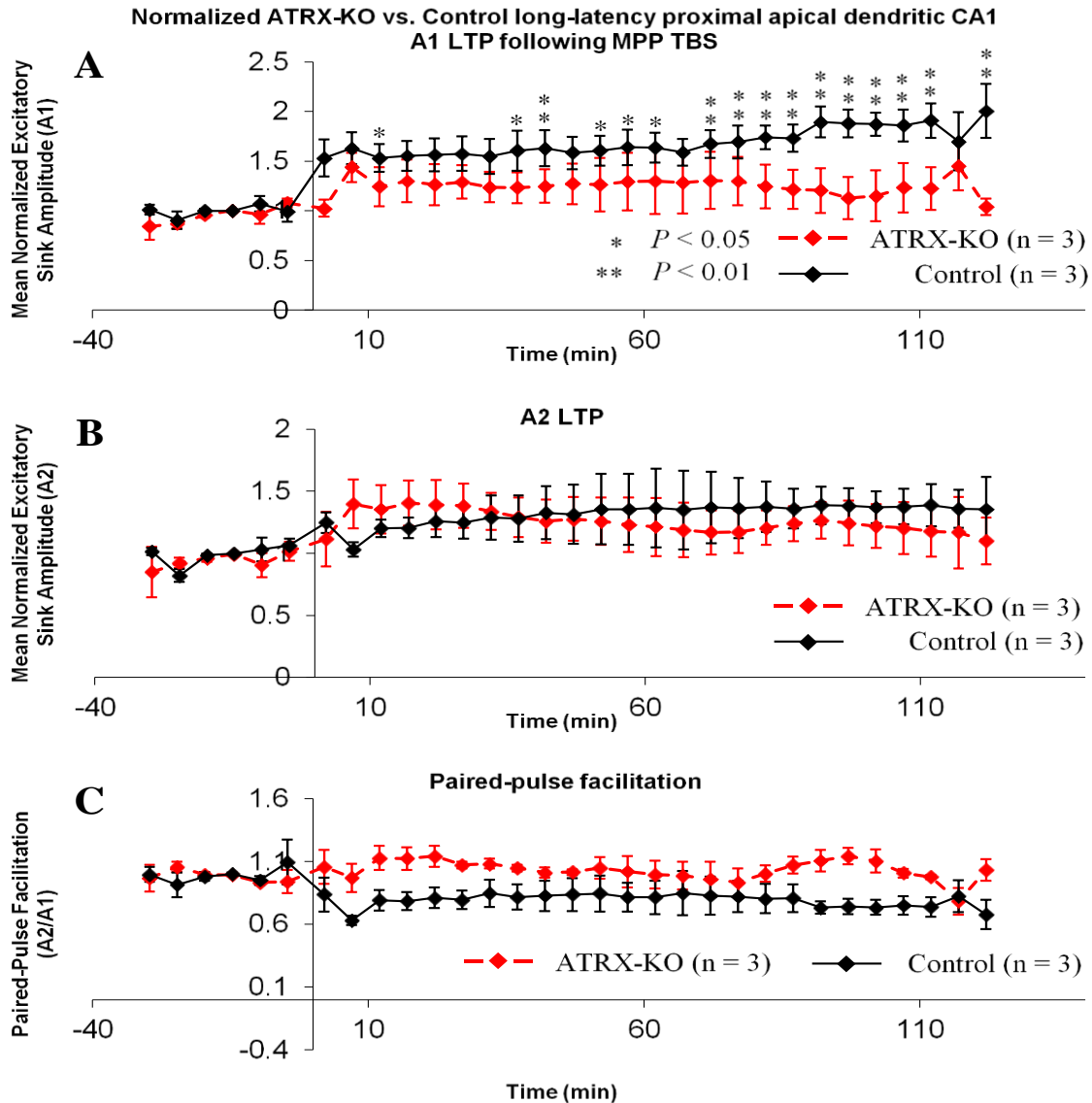


Fig. 41. Impaired long-latency proximal apical dendritic A1 LTP following MPP TBS in ATRX-KO mice compared to controls.

Mean normalized excitatory sink amplitude (\pm SEM) (y-axis) in the proximal apical dendritic CA1 region as a function of time (x-axis) both before and after LTP induction by MPP TBS (time = 0) in control (n = 3) and ATRX-KO mice (n = 3). Response following first pulse (A1), second pulse (A2), and ratio (A2/A1) were normalized and averaged (see Methods). **A**) A1 was decreased in ATRX-KO mice at 17, 37–42, 52–62, and 72–120 min post-TBS ($p < 0.05$, Newman Keuls post-hoc difference). **B**) Same as (A) but A2 was plotted, with no difference between groups. **C**) Trend indicating increased PPF in ATRX-KO mice relative to controls post-MPP-TBS (see Results).

3.4.3 Input-output relation two hours post-TBS: ATRX-KO mice displayed impaired long-latency proximal apical dendritic LTP post-TBS compared to controls

A final I/O curve (IO2) was generated for the MPP to long-latency proximal apical dendritic CA1 two hours post-MPP-TBS for both control ($n = 3$) and ATRX-KO mice ($n = 3$). Neither control nor ATRX-KO mice displayed statistically significant paired-pulse facilitation (PPF) in the proximal apical dendrites of CA1 following MPP stimulation two hours post-TBS (Fig. 42A and 43A, respectively). Comparison of A1 and A2 response between IO1 and IO2 (Fig. 42B, C) in control mice revealed a significant group x intensity interaction effect (two-way randomized block ANOVA; A1: $F_{4,8} = 4.96$, $p = 0.026$; A2: $F_{6,12} = 4.26$, $p = 0.016$), where A1 and A2 were significantly increased in IO2 relative to IO1 at several MPP stimulus intensities ($p < 0.05$). These findings confirmed LTP in the long-latency proximal apical dendritic response in control mice following MPP TBS. ATRX-KO mice did not display any significant differences in A1 or A2 response, when compared between IO1 and IO2 (Fig. 43B, C), but there was a trend indicating A2 potentiation in IO2 vs. IO1 ($F_{6,12} = 2.59$, $p = 0.076$). Overall, this confirmed a lesser extent of LTP of the MPP to CA1 trisynaptic response in ATRX-KO mice compared to controls. Comparison of A1 and A2 response in IO2 between control and ATRX-KO mice (Fig. 44A, B) displayed no significant group or group x intensity effects between groups (verified by two-way repeated measures ANOVA). However, a group effect trend indicated that ATRX-KO mice had impaired long-latency proximal apical dendritic responses for A1 ($F_{1,4} = 5.98$, $p = 0.071$) and A2 ($F_{1,4} = 4.15$, $p = 0.11$) compared to controls in IO2 (two-way repeated measures ANOVA). Paired-pulse facilitation has been investigated in I/O curves post-TBS and compared between control and ATRX-KO mice (Fig. 44C). No significant difference was found between groups for long-latency proximal apical dendritic PPF in IO2. To conclude, ATRX-KO mice displayed impaired long-latency proximal apical dendritic A1 and A2 responses in IO2, compared to controls.

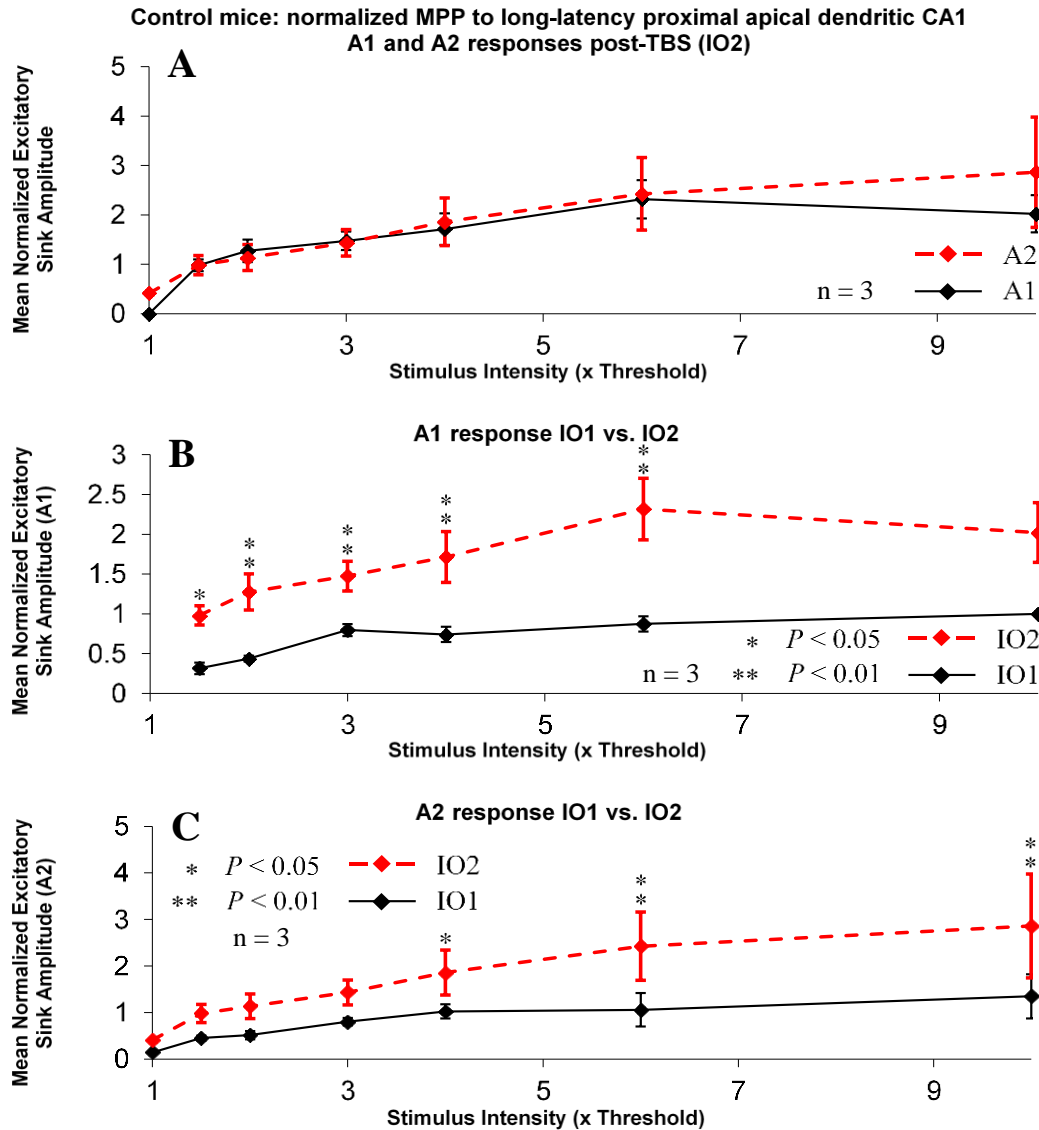


Fig. 42. IO2 response for control mice confirmed LTP in the long-latency proximal apical dendritic sink following MPP TBS.

Mean normalized excitatory sink amplitude (\pm SEM) in proximal apical dendritic CA1 region after first pulse (A1) and second pulse (A2) of MPP stimulation at increasing intensity (x-axis) two hours post-TBS (IO2) in control mice ($n = 3$). **A**) A1 and A2 response as a function of stimulus intensity, with no significant differences between the two. **B**) A1 response plotted for baseline (IO1) and IO2. A1 responses in IO2 were significantly greater than in IO1 at stimulus intensities of 1.5–6 x T ($p < 0.05$, Newman Keuls multiple post-hoc comparisons). **C**) Same as (B) except A2 responses were plotted with significant post-hoc differences after a significant group x intensity interaction effect in two-way randomized block ANOVA.

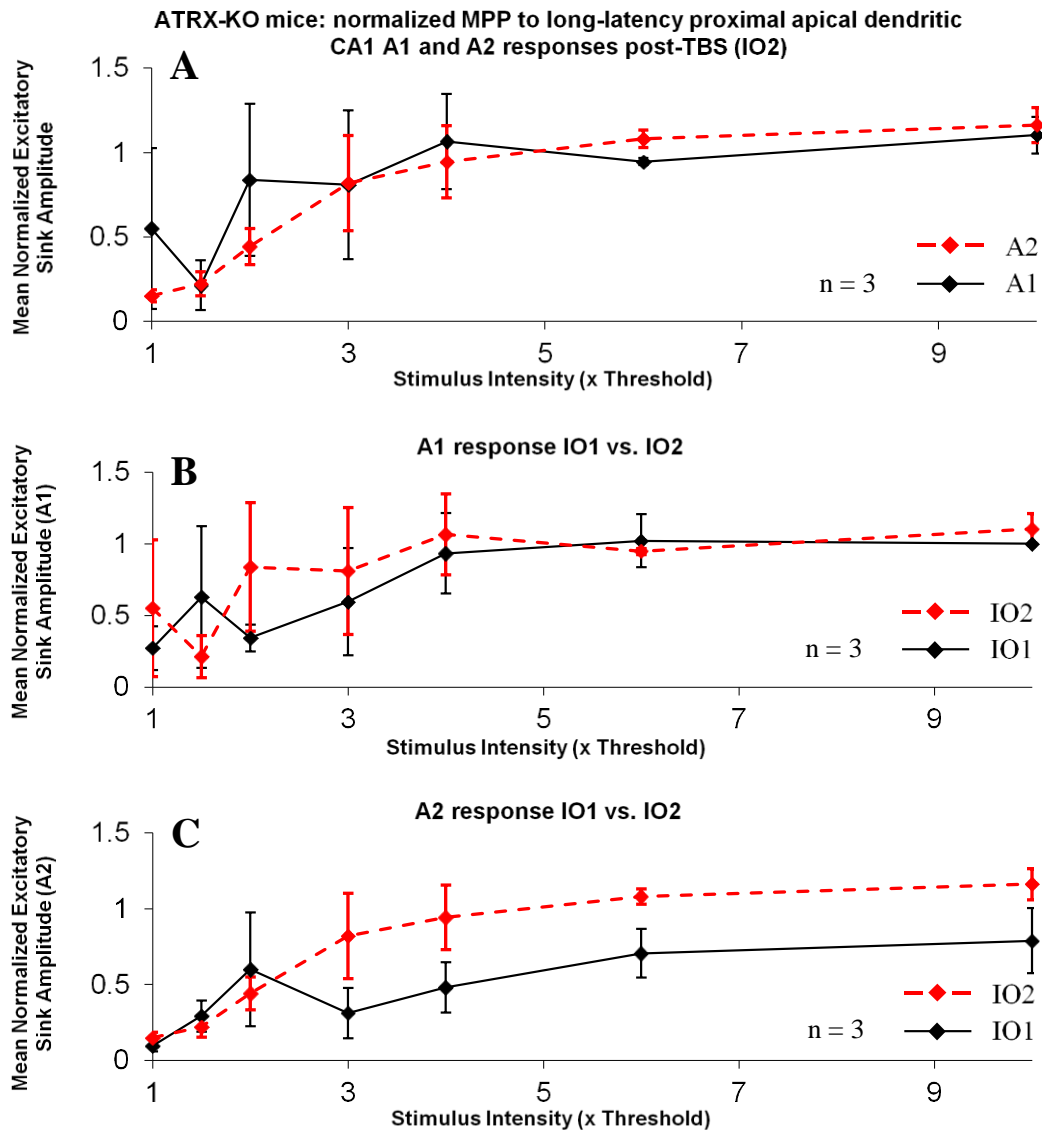


Fig. 43. IO2 response for ATRX-KO mice displayed trend of potentiated A2 long-latency proximal apical dendritic CA1 response following MPP TBS.

Mean normalized excitatory sink amplitude (\pm SEM) in proximal apical dendritic CA1 region after first pulse (A1) and second pulse (A2) of MPP stimulation at increasing intensities (x-axis) two hours post-TBS (IO2) in ATRX-KO mice (n = 3). **A**) A1 and A2 response as a function of stimulus intensity. There were no differences between A1 and A2 response in IO2 (two-way randomized block ANOVA). **B**) A1 response plotted for baseline (IO1) and IO2. A1 responses in IO2 were not significantly different than in IO1 (two-way randomized block ANOVA, see Results). **C**) Same as (B) except A2 responses were plotted, with trend indicating potentiation of A2 long-latency proximal apical dendritic response in IO2 compared to IO1 (see Results).

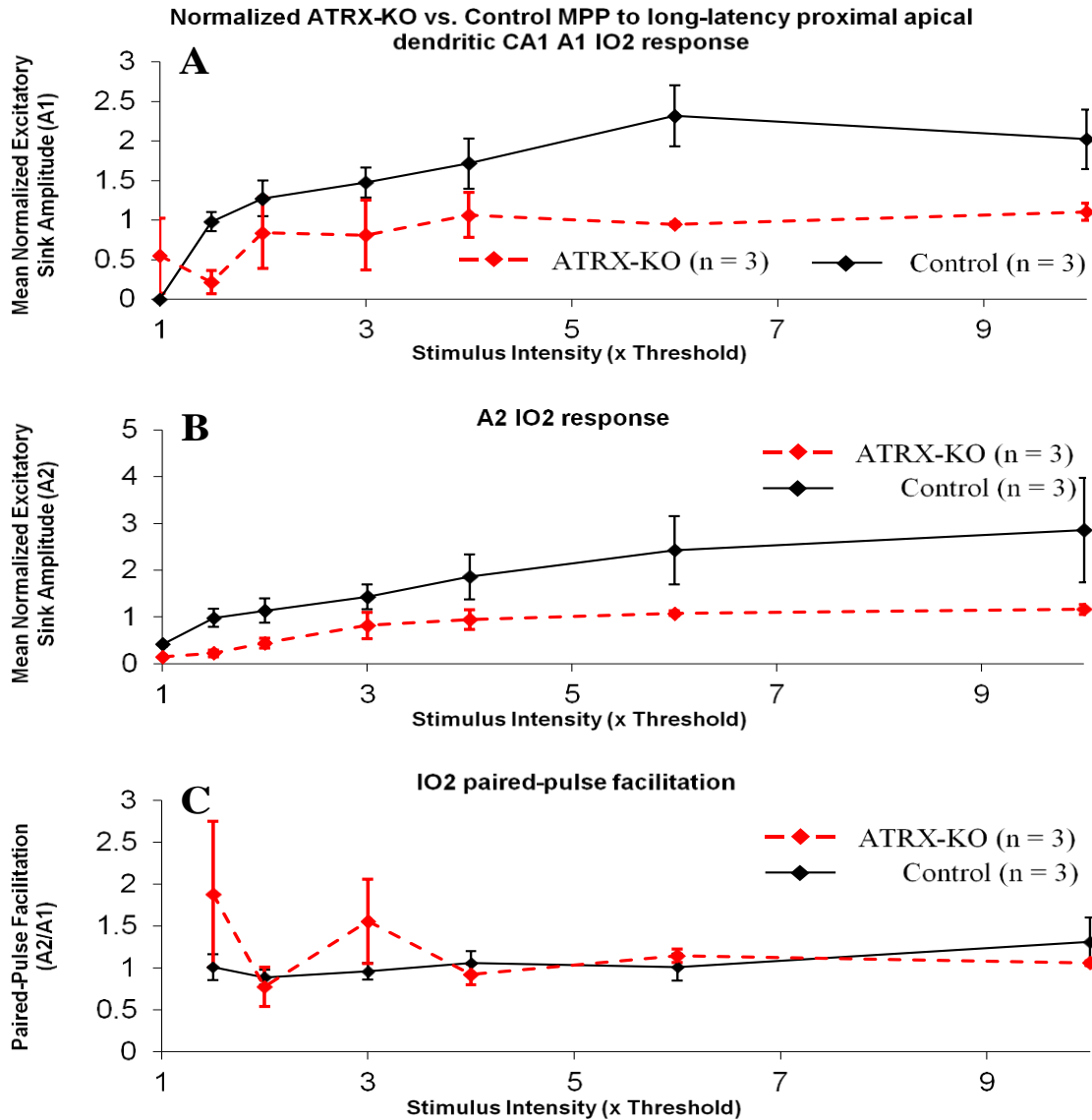


Fig. 44. Trend indicating impaired A1 and A2 long-latency proximal apical dendritic response in ATRX-KO mice compared to controls.

Mean normalized excitatory sink amplitude (\pm SEM) in proximal apical dendritic CA1 region after first pulse (A1) and second pulse (A2) of MPP stimulation at increasing intensity (x-axis) two hours post-TBS (IO2), as well as long-latency proximal apical dendritic paired-pulse facilitation (PPF) in control (n = 3) and ATRX-KO mice (n = 3). **A**) Trend of decreased A1 response in ATRX-KO mice compared to controls (two-way repeated measures ANOVA, see Results). **B**) Same as (A) but A2 response was plotted, displaying similar trend (see Results). **C**) PPF, measured by A2/A1, displayed no significant differences between control and ATRX-KO mice.

Chapter 4

4 Discussion

4.1 *In vivo* synaptic transmission and LTP in a mouse model of intellectual disability

The objective of this study was to examine changes in hippocampal synaptic transmission and LTP *in vivo* to understand the biological basis of memory impairment in ATRX-KO mice. We hypothesized that postnatal conditional ablation of the *ATRX* gene in neurons would disrupt hippocampal synaptic transmission and plasticity. We investigated several hippocampal synaptic pathways using paired-pulse stimulation at different stimulus intensities, and two major synapses, on the basal dendrites and distal apical dendrites of CA1 pyramidal cells. We also provide preliminary results on LTP of the MPP to CA1 polysynaptic pathway, thought to be one of the primary routes of information propagation through the hippocampus. We found that ATRX-KO mice exhibited basal dendritic LTP following stratum oriens TBS, which was highly similar in magnitude and consistency to that of controls. This LTP was confirmed at multiple stimulus intensities in both groups by post-TBS I/O curves. In contrast, ATRX-KO mice were deficient in distal apical dendritic (via temporoammonic pathway) as well as long-latency proximal apical dendritic (via trisynaptic circuit) LTP one-hour post-MPP-TBS, revealing impairments in the ability of ATRX-KO mice to maintain long-lasting synaptic potentiation in these pathways. These findings may reveal hippocampal pathway-specific deficiencies in ATRX-KO mice which underlie their impairments in long-term hippocampus-dependent spatial memory tasks.

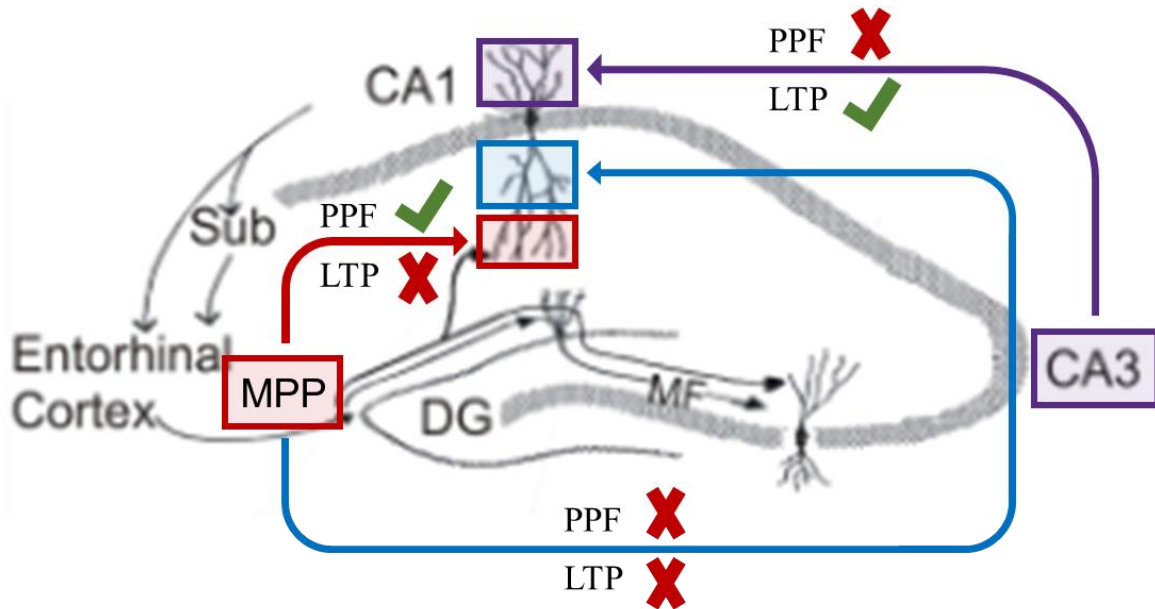


Fig. 45. Summary schematic of hippocampal pathway-specific findings.

Coronal section of the mouse hippocampus adapted from Fig. 2 displaying hippocampal pathway-specific findings. The stratum oriens to basal dendritic projection (indicated by purple labels) featured impaired paired-pulse facilitation (PPF) at baseline but normal LTP following stratum oriens TBS in ATRX-KO mice. The MPP monosynaptic projection to the distal apical dendritic CA1 (red labels) displayed normal PPF at baseline but impaired LTP following MPP TBS in ATRX-KO mice compared to controls. The MPP trisynaptic projection to the proximal apical dendritic CA1 (blue labels) featured ATRX-KO impairments in baseline PPF and LTP following MPP TBS.

4.2 Synaptic transmission during baseline

Baseline (before LTP induction) input-output relation of several hippocampal synaptic pathways of control and ATRX-KO mice were studied, including the stratum oriens to basal dendritic CA1, MPP to middle molecular layer of DG, MPP to distal apical dendritic CA1, and MPP to long-latency proximal apical excitation via the trisynaptic circuit.

4.2.1 Stratum oriens to basal dendritic CA1

Stratum oriens stimulation of the hippocampus is known to preferentially excite the afferents from CA3 and CA2 to the basal dendrites of the CA1 region (Ishizuki et al. 1990; Li et al. 1994; Shinohara et al. 2012). Our results for hippocampal synaptic transmission in this pathway at baseline largely show no difference between controls and ATRX-KO mice. Both groups displayed basal dendritic paired-pulse facilitation (PPF) following stratum oriens stimulation at multiple intensities. PPF is commonly thought to occur due to leftover Ca^{2+} in the synapse following the first pulse (E1) resulting in increased Ca^{2+} influx into the presynaptic terminal following the second pulse (E2) and a larger E2 response (Zucker and Regehr 2002). High-intensity paired-pulse field responses *in vivo* may also involve postsynaptic factors, such as saturation of population EPSP, and inhibitory conductance effect on E2 response (Leung et al. 2008). Although ATRX-KO mice demonstrated a larger E2 compared to E1 response, the PPF observed in the basal dendritic CA1 in ATRX-KO mice was smaller than that in control mice following stratum oriens stimulation at increasing intensity. It is possible that the basal dendritic environment of ATRX-KO mice has a lower electromotive force (emf) for pEPSP, or a higher inhibitory conductance at E2. Nevertheless, ATRX-KO mice displayed similar absolute and normalized E1 response to controls at a fixed stimulus intensity, so it is likely that their basic properties of synaptic transmission, like Ca^{2+} influx and neurotransmitter mobilization at the presynaptic neuron are normal.

4.2.2 MPP to middle molecular layer of DG

Investigation of the MPP to middle molecular layer of the DG pathway revealed differences in synaptic transmission between control and ATRX-KO mice at baseline. While both control and ATRX-KO mice displayed significant PPF ($E2 > E1$) in the range of 1.1–1.3 at 50 ms inter-pulse interval (IPI) at several stimulus intensities, ATRX-KO mice displayed saturation of DG middle molecular layer E1 and E2 response following MPP stimulation at a lower intensity compared to controls. In other words, the proportion of maximal response (response at $10 \times T$ for each group) achieved by ATRX-KO mice at $3\text{--}6 \times T$ was significantly larger than that of control mice at the same intensity. In addition, ATRX-KO mice displayed a plateau in DG middle molecular layer response at $6 \times T$ MPP stimulation, whereas controls continued to display an upward trend of

increased response following increased stimulus intensity. There may be several reasons why there was a significant difference between E1 DG middle molecular layer response as a function of MPP stimulus intensity in ATRX-KO mice compared to controls. One possibility is that the synapses of ATRX-KO mice, compared to control mice, may be clustered together such that neurotransmitter released by adjacent synapses, which are activated by increasing stimulus intensity, may not increase the total postsynaptic response. As a result, a fixed stimulus intensity (as a function of threshold) may activate more excitatory synapses simultaneously in ATRX-KO than control mice, thus producing larger depolarization at low intensity and reaching saturation earlier. Another possibility is that the DG of ATRX-KO mice is composed of a more homogeneous group of large-diameter fibers—which have a lower threshold intensity for activation than small-diameter fibers—such that high-intensity stimulation recruits fewer small-diameter axons and produces less total excitation compared to controls.

4.2.3 MPP to distal apical dendritic CA1

The MPP to CA1 distal apical dendritic pathway displayed PPF ($E2 > E1$) for both control and ATRX-KO mice at baseline. The degree of PPF ($E2/E1 \sim 1.1$) was modest at 50 ms IPI but it was uniform across stimulus intensity for both control and ATRX-KO mice (Fig. 24). ATRX-KO mice and control mice did not significantly differ in $E1$, $E2$, or $E2/E1$ at the MPP to CA1 distal apical dendritic synapse at baseline.

4.2.4 MPP to CA1 polysynaptic pathway

The most striking differences in baseline synaptic transmission between controls and ATRX-KO mice were discovered in the long-latency proximal apical dendritic CA1 response following MPP stimulation. This trisynaptic circuit activation involves layer II cells of the entorhinal cortex (EC) synapsing onto the DG, mossy fiber projections from DG to the CA3, and Schaffer collateral projection from CA3 to the CA1 proximal apical dendrites. Preliminary data indicate that PPF was not discovered at low stimulus intensities ($\leq 3 \times T$) for control or ATRX-KO mice. At high stimulus intensities ($> 4 \times T$), there were no within-group differences in paired-pulse plasticity, but between-group comparisons revealed a trend of PPF in controls and paired-pulse depression (PPD) in ATRX-KO mice. This suggests that there are differences in synaptic transmission along

the trisynaptic circuit in ATRX-KO mice compared to controls at baseline. However, other than PPF at most glutamatergic synapses in the polysynaptic pathway, firing of action potentials and inhibition evoked in DG and CA3 may affect the A2 response in CA1. Thus, the exact hippocampal area(s) of difference between ATRX-KO and control mice are not known.

4.3 LTP time course analyses

4.3.1 Stratum oriens to basal dendritic CA1 LTP and associated control pathway

The stratum oriens was tetanized using a theta-burst stimulation (TBS) to reliably induce LTP in the basal dendritic CA1 region, as was done previously by our lab (Leung et al. 1992; Kaibara and Leung 1993; Leung and Shen 1995; Fung et al. 2016). There were no significant differences in magnitude or extent of LTP between controls and ATRX-KO mice, as confirmed by time course analysis (of 2 x T responses) before and after TBS. The rapid onset of LTP as well as gradual but slight degradation of LTP in both groups was very similar. I/O curves performed two hours post-TBS confirmed basal dendritic LTP in both groups and showed that E1 potentiation extended to responses of higher than 2 x T intensity in both controls and ATRX-KO mice. No differences were found regarding E2 or E2/E1 responses during the time course analysis or the post-TBS I/O curves. In the MPP to middle molecular layer of DG synaptic pathway (which served as a non-tetanized control pathway), it was observed that both control and ATRX-KO mice displayed a slight positive trend of E1 response throughout the 2-hour monitoring period. While DG middle molecular layer responses in control mice were not significantly different two hours post-TBS compared to baseline, ATRX-KO mice had a significantly potentiated 115-min time point DG response following MPP stimulation. I/O curves performed post-TBS confirmed LTP in the ATRX-KO mice but not control mice. The post-TBS I/O curves also suggest that PPF, which was present during baseline in controls and ATRX-KO mice, has disappeared for both groups. Finally, post-TBS I/O curves still displayed the same trend for more rapid DG response saturation in ATRX-KO mice compared to controls, but this difference between groups was no longer significant.

The small late potentiation (averaging ~10%) in control and ATRX-KO mice in the non-tetanized MPP to middle molecular layer of DG pathway was not expected. It may have occurred because

of small instability over the two hours. In addition, we suggest that it could be caused by the spread of stimulating currents during stratum oriens TBS. In the mouse, stratum oriens is about 0.5 mm away from the perforant path fibers, some of which synapse in DG but continue to the distal apical dendrites of CA2/CA3. TBS of 4 x T delivered to the CA3, of ~120 μ A stimulus intensity, could activate the perforant path fibers (of 16 μ A mean threshold) located ~0.5 mm away. In the I/O determination of some mice, a DG middle molecular layer sink (typical of MPP activation) could be observed at high-intensity single-pulse stimulation of stratum oriens. Nevertheless, the E1 potentiation that occurred in the MPP-DG synapse after stratum oriens TBS was small, compared to the LTP of the CA1 basal dendrites, in either control or ATRX-KO mice.

4.3.2 MPP to distal apical dendritic CA1 LTP and associated control pathway

Differences between control and ATRX-KO mice were found for LTP of the MPP to distal apical dendritic synapse. Distal apical dendritic LTP in both controls and ATRX-KO mice increased gradually at a similar rate but differed in temporal maintenance and stability. Whereas control LTP was sustained for two hours post-MPP-TBS, ATRX-KO distal apical dendritic LTP began to degrade approximately one-hour post-TBS. Between-group comparisons revealed a significant decrease in ATRX-KO mice distal apical dendritic LTP compared to controls at 1–2 hours post-TBS, and this difference was reflected in both E1 and E2 responses. Whereas ATRX-KO mice displayed normal basal dendritic LTP following stratum oriens TBS, they were deficient in distal apical dendritic LTP following MPP TBS. Studies have shown that the basal and apical dendrites of CA1 mediate LTP using different mechanisms with different intracellular targets (Brzdak et al. 2017). In control mice, LTP was confirmed by the post-TBS I/O curves, which displayed greater E1 response at most stimulus intensities post-TBS compared to baseline. In ATRX-KO mice, however, mean E1 and E2 were larger post-TBS compared to baseline, but there was no significant difference in E1 or E2 response between post-TBS and baseline. The small LTP may not be observed in the I/O curve likely because of the high variability of the responses (average of 4 traces) recorded for I/O, as compared to an average of 8 sweeps for the AEPs recorded during time course analysis, and then further averaging of AEPs across 5 adjacent time points, effectively averaging 40 sweeps. At 2 hours after TBS, E1 and E2 responses of ATRX-KO mice appeared to saturate or plateau at 3 x T MPP stimulus intensity, whereas

responses of control mice gradually increased until 10 x T stimulus intensity. This difference between I/O curves of ATRX-KO and control mice was only apparent after MPP TBS, but the physiological mechanisms at play are unknown.

In the CA3 to proximal apical dendritic Schaffer collateral control pathway, we encountered difficulties isolating a short-latency proximal apical dendritic sink in some mice. In mice that showed a clear proximal apical dendritic sink in CA1, no synaptic potentiation of the latter sink was found after TBS of the MPP. This was expected as MPP stimulation of layer III EC cells projects directly to the distal apical dendrites of CA1 through the temporoammonic pathway. In the event that MPP stimulation also resulted in trisynaptic circuit activation, increase in a long-latency proximal apical sink in CA1 was observed, but the potentiation may occur at multiple synapses in the trisynaptic circuit, or distributed across different CA3 subregions along the septohippocampal axis, such that stimulation of afferents from a small part of CA3 may not be potentiated.

4.3.3 MPP to CA1 polysynaptic pathway LTP

In some mice, MPP stimulation produced a long-latency proximal apical dendritic CA1 response via the trisynaptic circuit, which was investigated for LTP. Because this response involved a polysynaptic pathway, its time of onset was delayed (>10 ms) compared to the other responses we have studied (<5 ms). After TBS of the MPP, control mice displayed LTP of the 1st pulse response (A1), accompanied by PPD, whereas ATRX-KO mice only displayed LTP of the 2nd pulse response (A2), with no change in PPF. It is unknown whether PPF at the proximal apical dendrites of CA1 is influenced by LTP. Some studies suggest a negative correlation between LTP and PPF in the proximal apical dendritic CA1 Schaffer collateral pathway (Christie and Abraham 1994; Schulz et al. 1994), whereas others suggest no correlation (Manabe et al. 1993). Between-group comparisons revealed significantly reduced A1 response in ATRX-KO mice compared to controls at several time points post-MPP-TBS. I/O curves performed at 2 h post-TBS confirmed that A1 was potentiated at 2 x T as well as at higher stimulus intensities for control mice, whereas no significant change was found for A1 or A2 response of ATRX-KO mice post-TBS compared to baseline. The relatively high variability of the responses acquired during I/O likely accounts for the inability to detect a small LTP of the MPP to CA1 long-latency

proximal apical dendritic responses in ATRX-KO mice. The results suggest that ATRX-KO mice may be deficient in LTP of the trisynaptic circuit compared to controls. However, it is not known which synapse of this polysynaptic circuit may be deficient.

4.4 Relation of electrophysiological measures to structural and behavioural findings in ATRX-KO mice

Imaging and behavioural studies have been performed on control and ATRX-KO mice used in the present thesis (Tamming et al. unpublished). In ATRX-KO mice, electron microscopy images of the CA1 stratum radiatum have revealed synapses with significantly decreased presynaptic vesicle count, wider synaptic cleft and larger postsynaptic density, as compared to control mice. However, no differences in apical dendritic branching were found between ATRX-KO and control mice.

In this thesis, we reported that ATRX-KO mice, compared to control mice, generally showed decreased hippocampal synaptic transmission, as indicated by lower PPF of the CA1 basal dendritic synapse, lower PPF of the MPP to CA1 distal apical dendritic synapse after TBS, and decreased LTP of the CA1 distal apical dendritic synapse and the MPP to CA1 trisynaptic response. However, a direct relation of the decrease in electrophysiological measures of synaptic transmission/plasticity to ultrastructural parameters remains unclear. Also, ultrastructural data were available only for stratum radiatum, where the Schaffer collaterals synapse on the proximal apical dendrites. We did not have PPF measures for the proximal apical dendritic synapses in CA1 stratum radiatum. The fact that some CA3 cells project to both stratum oriens and stratum radiatum (Amaral and Witter 1989; Li et al. 1994) may suggest similar morphological features in stratum oriens as well. Fewer presynaptic vesicles are more rapidly depleted and may not leave sufficient vesicles for release with the 2nd pulse, thus, leading to a decrease in PPF. A decrease in PPF of individual hippocampal synapses may also contribute to the overall PPD of the MPP to CA1 trisynaptic response in ATRX-KO mice, which again could be related to a limit in glutamatergic synaptic vesicles in hippocampal glutamatergic terminals.

Behavioural studies have demonstrated that ATRX-KO mice are impaired in hippocampus-dependent long-term spatial memory tasks, such as the Morris water maze, contextual fear conditioning, and paired-associate operant learning task (Tamming et al. unpublished). ATRX-

KO mice compared to control mice were not different in basal dendritic LTP in CA1 but were significantly impaired in distal apical dendritic LTP following MPP stimulation. In addition, there was an impairment in the trisynaptic MPP to CA1 LTP, as measured at the proximal apical dendritic CA1. Ultrastructural imaging has not been done in the stratum lacunosum moleculare layer of CA1, which corresponds to the distal apical dendrites. There is, however, evidence that the temporoammonic pathway is implicated in long-term spatial memory consolidation (Brun et al. 2002; Brun et al. 2008), which is encouraging. The latter may explain impairment of 12-day versus 5-day retention results of ATRX-KO mice in the Morris water maze (Tamming et al. unpublished).

In general, ATRX-KO mice, while normal in basal dendritic LTP following stratum oriens TBS, are impaired in both distal and long-latency proximal apical dendritic CA1 LTP following MPP TBS. The mechanisms underlying these LTP impairments are likely different from those responsible for basal dendritic LTP. In addition, ATRX-KO mice have displayed impaired 2nd pulse response compared to controls in several instances which may be in accordance with ultrastructural abnormalities found in the stratum radiatum cell layer of CA1. These findings are encouraging as we were able to find deficiencies in major hippocampal synaptic pathways which may underlie the long-term hippocampus-dependent spatial memory deficits found in ATRX-KO mice.

4.5 Future Studies

Further studies will aim to directly investigate the CA3 to proximal apical dendritic CA1 pathway because our investigation of the trisynaptic circuit as well as ultrastructural imaging studies (Tamming et al. unpublished) point to the Schaffer collaterals to stratum radiatum CA1 synapse as a potential area of abnormality in ATRX-KO mice. As one of the most well-studied hippocampal synaptic pathways with implications in spatial learning and memory, our investigation of the Schaffer collaterals to proximal apical dendritic CA1 would allow us to establish a comprehensive study of major excitatory hippocampal synaptic pathways synapsing onto different regions of CA1 pyramidal neurons.

Another approach to LTP and synaptic transmission is to undertake these studies in behaving animals without anesthesia. The physiological measures can then be directly correlated with the

animal's performance in a particular spatial learning and memory task. As our study only investigated hippocampal excitatory synaptic pathways, future studies could also focus on the investigation of inhibitory synaptic pathways in animal models of intellectual disability. We hope to one day unravel the functionality of the different hippocampal synaptic pathways and understand how they contribute to deficits in hippocampus-dependent memory.

References

Aapola U, Shibuya K, Scott HS, Ollila J, Vihinen M, Heino M, Shintani A, Kawasaki K, Minoshima S, Krohn K, Antonarakis SE, Shimizu N, Kudoh J, Peterson P. Isolation and initial characterization of a novel zinc finger gene, DNMT3L, on 21q22. 3, related to the cytosine-5-methyltransferase 3 gene family. *Genomics* 65: 293–298, 2000.

Abraham WC. How long will long-term potentiation last? *Philosophical Transactions of the Royal Society of London Series B: Biological Sciences* 358: 735–744, 2003.

Abraham WC, Otani S. Macromolecules and the maintenance of long-term potentiation. *Kindling and synaptic plasticity* 92–109, 1991.

Amaral DG, Witter MP. The three-dimensional organization of the hippocampal formation: a review of anatomical data. *Neuroscience* 31: 571–591, 1989.

Andersen P, Morris R, Amaral D, O'Keefe J, Bliss T. *The hippocampus book*. Oxford University Press, 2007.

Argentaro A, Yang J, Chapman L, Kowalczyk MS, Gibbons RJ, Higgs DR, Neuhaus D, Rhodes D. Structural consequences of disease-causing mutations in the ATRX-DNMT3-DNMT3L (ADD) domain of the chromatin-associated protein ATRX. *Proceedings of the National Academy of Sciences* 104: 11939–11944, 2007.

Badens C, Lacoste C, Philip N, Martini N, Courier S, Giuliano F, Verloes A, Munnich A, Leheup B, Burglen L. Mutations in PHD-like domain of the ATRX gene correlate with severe psychomotor impairment and severe urogenital abnormalities in patients with ATRX syndrome. *Clinical genetics* 70: 57–62, 2006.

Badens C, Martini N, Courier S, DesPortes V, Touraine R, Levy N, Edery P. ATRX syndrome in a girl with a heterozygous mutation in the ATRX Zn finger domain and a totally

skewed X-inactivation pattern. *American Journal of Medical Genetics Part A* 140: 2212–2215, 2006.

Bagal AA, Kao JP, Tang C-M, Thompson SM. Long-term potentiation of exogenous glutamate responses at single dendritic spines. *Proceedings of the National Academy of Sciences* 102: 14434–14439, 2005.

Benke TA, Lüthi A, Isaac JT, Collingridge GL. Modulation of AMPA receptor unitary conductance by synaptic activity. *Nature* 393: 793, 1998.

Bérubé NG, Healy J, Medina CF, Wu S, Hodgson T, Jagla M, Picketts DJ. Patient mutations alter ATRX targeting to PML nuclear bodies. *European Journal of Human Genetics* 16: 192, 2008.

Bérubé NG, Jagla M, Smeenk C, De Repentigny Y, Kothary R, Picketts DJ. Neurodevelopmental defects resulting from ATRX overexpression in transgenic mice. *Human molecular genetics* 11: 253–261, 2002.

Bérubé NG, Mangelsdorf M, Jagla M, Vanderluit J, Garrick D, Gibbons RJ, Higgs DR, Slack RS, Picketts DJ. The chromatin-remodeling protein ATRX is critical for neuronal survival during corticogenesis. *The Journal of clinical investigation* 115: 258–267, 2005.

Bérubé NG, Smeenk CA, Picketts DJ. Cell cycle-dependent phosphorylation of the ATRX protein correlates with changes in nuclear matrix and chromatin association. *Human molecular genetics* 9: 539–547, 2000.

Bir SC, Ambekar S, Kukreja S, Nanda A. Julius Caesar Arantius (Giulio Cesare Aranzi, 1530-1589) and the hippocampus of the human brain: history behind the discovery. *J Neurosurg* 122: 971–975, 2015.

Blackstad TW. On the termination of some afferents to the hippocampus and fascia dentata. *Cells Tissues Organs* 35: 202–214, 1958.

Bliss TV, Lømo T. Long-lasting potentiation of synaptic transmission in the dentate area of the anaesthetized rabbit following stimulation of the perforant path. *The Journal of physiology* 232: 331–356, 1973.

Bliss TV, Collingridge GL. A synaptic model of memory: long-term potentiation in the hippocampus. *Nature* 361: 31, 1993.

Brun VH, Leutgeb S, Wu H, Schwarcz R, Witter MP, Moser EI, Moser M. Impaired spatial representation in CA1 after lesion of direct input from entorhinal cortex. *Neuron* 57: 290–302, 2008.

Brun VH, Otnæss MK, Molden S, Steffenach H-A, Witter MP, Moser M-B, Moser EI. Place cells and place recognition maintained by direct entorhinal-hippocampal circuitry. *Science* 296: 2243–2246, 2002.

Brzdak P, Wójcicka O, Zareba-Koziol M, Minge D, Henneberger C, Włodarczyk J, Mozrzymas JW, Wójtowicz T. Synaptic potentiation at basal and apical dendrites of hippocampal pyramidal neurons involves activation of a distinct set of extracellular and intracellular molecular cues. *Cerebral Cortex* 29: 283–304, 2017.

Capocchi G, Zampolini M, Larson J. Theta burst stimulation is optimal for induction of LTP at both apical and basal dendritic synapses on hippocampal CA1 neurons. *Brain Res* 591: 332–336, 1992.

Cardoso C, Timsit S, Villard L, Khrestchatisky M, Fontès M, Colleaux L. Specific Interaction between the XNP ATR-X Gene Product and the SET Domain of the Human EZH2 Protein. *Human molecular genetics* 7: 679–684, 1998.

Christie BR, Abraham WC. Differential regulation of paired-pulse plasticity following LTP in the dentate gyrus. *Neuroreport* 5: 385–388, 1994.

Colbert CM, Levy WB. Electrophysiological and pharmacological characterization of perforant path synapses in CA1: mediation by glutamate receptors. *Journal of neurophysiology* 68: 1–8, 1992.

Cutsuridis V, Cobb S, Graham BP. Encoding and retrieval in a model of the hippocampal CA1 microcircuit. *Hippocampus* 20: 423–446, 2010.

Daily DK, Ardinger HH, Holmes GE. Identification and evaluation of mental retardation. *Am Fam Physician* 61: 1059–1067, 1070, 2000.

des Portes V. X-linked mental deficiency. *Handb Clin Neurol* 111: 297–306, 2013.

Dhayalan A, Tamas R, Bock I, Tattermusch A, Dimitrova E, Kudithipudi S, Ragozin S, Jeltsch A. The ATRX-ADD domain binds to H3 tail peptides and reads the combined methylation state of K4 and K9. *Human molecular genetics* 20: 2195–2203, 2011.

Dudek SM, Bear MF. Homosynaptic long-term depression in area CA1 of hippocampus and effects of N-methyl-D-aspartate receptor blockade. In: *How We Learn; How We Remember: Toward An Understanding Of Brain And Neural Systems: Selected Papers of Leon N Cooper.* World Scientific, 1995, p. 200–204.

Durkin M. The epidemiology of developmental disabilities in low-income countries. *Mental retardation and developmental disabilities research reviews* 8: 206–211, 2002.

Eustermann S, Yang J-C, Law MJ, Amos R, Chapman LM, Jelinska C, Garrick D, Clynes D, Gibbons RJ, Rhodes D. Combinatorial readout of histone H3 modifications specifies localization of ATRX to heterochromatin. *Nature structural & molecular biology* 18: 777, 2011.

Paxinos G, Franklin KB. *The mouse brain in stereotaxic coordinates.* Gulf professional publishing, 2004.

Freund TF, Buzsaki G. Interneurons of the hippocampus. *Hippocampus* 6: 347–470, 1996.

Fung TK, Law CS, Leung LS. Associative spike timing-dependent potentiation of the basal dendritic excitatory synapses in the hippocampus in vivo. *Journal of neurophysiology* 115: 3264–3274, 2016.

Garrick D, Samara V, McDowell TL, Smith AJ, Dobbie L, Higgs DR, Gibbons RJ. A conserved truncated isoform of the ATR-X syndrome protein lacking the SWI/SNF-homology domain. *Gene* 326: 23–34, 2004.

Garrick D, Sharpe JA, Arkell R, Dobbie L, Smith AJ, Wood WG, Higgs DR, Gibbons RJ. Loss of Atrx affects trophoblast development and the pattern of X-inactivation in extraembryonic tissues. *PLoS genetics* 2: e58, 2006.

Gecz J, Pollaord H, Consalez G, Villard L, Stayton C, Millasseau P, Khrestchatisky M, Fontes M. Cloning and expression of the murine homologue of a putative human X-linked nuclear protein gene closely linked to PGK1 in Xq13. 3. *Human molecular genetics* 3: 39–44, 1994.

Gibbons R. Alpha thalassaemia-mental retardation, X linked. *Orphanet journal of rare diseases* 1: 15, 2006.

Gibbons RJ, Higgs DR. Molecular–clinical spectrum of the ATR-X syndrome. *American journal of medical genetics* 97: 204–212, 2000.

Gibbons RJ, Picketts DJ, Villard L, Higgs DR. Mutations in a putative global transcriptional regulator cause X-linked mental retardation with α -thalassemia (ATR-X syndrome). *Cell* 80: 837–845, 1995.

Gibbons RJ, Suthers GK, Wilkie AO, Buckle VJ, Higgs DR. X-linked alpha-thalassemia/mental retardation (ATR-X) syndrome: localization to Xq12-q21.31 by X inactivation and linkage analysis. *American journal of human genetics* 51: 1136–1149, 1992.

Gibbons RJ, Wilkie AO, Weatherall DJ, Higgs DR. A newly defined X linked mental retardation syndrome associated with alpha thalassaemia. *Journal of medical genetics* 28: 729, 1991.

Glees P, Griffith HB. Bilateral destruction of the hippocampus (cornu ammonis) in a case of dementia. *European Neurology* 123: 193–204, 1952.

Gottlieb DI, Cowan WM. Autoradiographic studies of the commissural and ipsilateral association connection of the hippocampus and dentate gyrus of the rat. I. The commissural connections. *J Comp Neurol* 149: 393–422, 1973.

Hebb DO. *The organization of behavior: A neuropsychological theory.* Psychology Press, 2005.

Higgs DR, Vickers MA, Wilkie AO, Pretorius IM, Jarman AP, Weatherall DJ. A review of the molecular genetics of the human alpha-globin gene cluster. *Blood* 73: 1081–1104, 1989.

Hitti FL, Siegelbaum SA. The hippocampal CA2 region is essential for social memory. *Nature* 508: 88–92, 2014.

Hutchison RM, Chidiac P, Leung LS. Hippocampal long-term potentiation is enhanced in urethane-anesthetized RGS2 knockout mice. *Hippocampus* 19: 687–691, 2009.

Insausti R. Comparative anatomy of the entorhinal cortex and hippocampus in mammals. *Hippocampus* 3: 19–26, 1993.

Ishizuka N, Weber J, Amaral DG. Organization of intrahippocampal projections originating from CA3 pyramidal cells in the rat. *Journal of comparative neurology* 295: 580–623, 1990.

Ishov AM, Sotnikov AG, Negorev D, Vladimirova OV, Neff N, Kamitani T, Yeh ET, Strauss JF, Maul GG. PML is critical for ND10 formation and recruits the PML-interacting protein daxx to this nuclear structure when modified by SUMO-1. *The Journal of cell biology* 147: 221–234, 1999.

Iwase S, Xiang B, Ghosh S, Ren T, Lewis PW, Cochrane JC, Allis CD, Picketts DJ, Patel DJ, Li H. ATRX ADD domain links an atypical histone methylation recognition mechanism to human mental-retardation syndrome. *Nature structural & molecular biology* 18: 769, 2011.

Johnston D, Williams S, Jaffe D, Gray R. NMDA-receptor-independent long-term potentiation. *Annual review of Physiology* 54: 489–505, 1992.

Johnston D, Wu SM. *Foundations of cellular neurophysiology*. MIT press, 1994.

Kaibara T, Leung LS. Basal versus apical dendritic long-term potentiation of commissural afferents to hippocampal CA1: a current-source density study. *Journal of neuroscience* 16: 2391–2404, 1993.

Kernohan KD, Jiang Y, Tremblay DC, Bonvissuto AC, Eubanks JH, Mann MR, Bérubé NG. ATRX partners with cohesin and MeCP2 and contributes to developmental silencing of imprinted genes in the brain. *Developmental cell* 18: 191–202, 2010.

Knowles WD. Normal anatomy and neurophysiology of the hippocampal formation. *Journal of Clinical Neurophysiology* 9: 253–263, 1992.

Kvarnung M, Nordgren A. Intellectual disability & rare disorders: a diagnostic challenge. In: *Rare Diseases Epidemiology: Update and Overview*. Springer, 2017, p. 39–54.

Lashley KS. In search of the engram. *physiological mechanisms* 454, 1950.

Leung LS. Generation of theta and gamma rhythms in the hippocampus. *Neuroscience & Biobehavioral Reviews* 22: 275–290, 1998.

Leung LS, Peloquin P, Canning KJ. Paired-pulse depression of excitatory postsynaptic current sinks in hippocampal CA1 in vivo. *Hippocampus* 18: 1008–1020, 2008.

Leung LS, Shen B. Long-term potentiation at the apical and basal dendritic synapses of CA1 after local stimulation in behaving rats. *Journal of neurophysiology* 73: 1938–1946, 1995.

Leung LS, Shen B, Kaibara T. Long-term potentiation induced by patterned stimulation of the commissural pathway to hippocampal CA1 region in freely moving rats. *Neuroscience* 48: 63–74, 1992.

Levy MA, Kernohan KD, Jiang Y, Bérubé NG. ATRX promotes gene expression by facilitating transcriptional elongation through guanine-rich coding regions. *Human molecular genetics* 24: 1824–1835, 2014.

Lewis PW, Elsaesser SJ, Noh K-M, Stadler SC, Allis CD. Daxx is an H3. 3-specific histone chaperone and cooperates with ATRX in replication-independent chromatin assembly at telomeres. *Proceedings of the National Academy of Sciences* 107: 14075–14080, 2010.

Li X-G, Somogyi P, Ylinen A, Buzsáki G. The hippocampal CA3 network: an in vivo intracellular labeling study. *Journal of comparative neurology* 339: 181–208, 1994.

Logie LJ, Gibbons RJ, Higgs DR, Brown JK, Porteous ME. Alpha thalassaemia mental retardation (ATR-X): an atypical family. *Archives of disease in childhood* 70: 439–440, 1994.

Lorente de Nó R. Studies on the structure of the cerebral cortex. II. Continuation of the study of the ammonic system. *Journal für Psychologie und Neurologie*, 1934.

Malenka RC, Bear MF. LTP and LTD: an embarrassment of riches. *Neuron* 44: 5–21, 2004.

Malinow R, Malenka RC. AMPA receptor trafficking and synaptic plasticity. *Annual review of neuroscience* 25: 103–126, 2002.

Manabe T, Wyllie DJ, Perkel DJ, Nicoll RA. Modulation of synaptic transmission and long-term potentiation: effects on paired pulse facilitation and EPSC variance in the CA1 region of the hippocampus. *Journal of neurophysiology* 70: 1451–1459, 1993.

Maulik PK, Mascarenhas MN, Mathers CD, Dua T, Saxena S. Prevalence of intellectual disability: a meta-analysis of population-based studies. *Research in developmental disabilities* 32: 419–436, 2011.

McDowell TL, Gibbons RJ, Sutherland H, O'Rourke DM, Bickmore WA, Pombo A, Turley H, Gatter K, Picketts DJ, Buckle VJ. Localization of a putative transcriptional regulator (ATRX) at pericentromeric heterochromatin and the short arms of acrocentric chromosomes. *Proceedings of the National Academy of Sciences* 96: 13983–13988, 1999.

Milner B. Les troubles de la memoire accompagnant des lesions hippocampiques bilaterales. *Physiologie de l'hippocampe* 257–272, 1962.

Mishkin M. Memory in monkeys severely impaired by combined but not by separate removal of amygdala and hippocampus. *Nature* 273: 297, 1978.

Miyamoto E, Fukunaga K. A role of Ca²⁺/calmodulin-dependent protein kinase II in the induction of long-term potentiation in hippocampal CA1 area. *Neurosci Res* 24: 117–122, 1996.

Nabavi S, Fox R, Proulx CD, Lin JY, Tsien RY, Malinow R. Engineering a memory with LTD and LTP. *Nature* 511: 348–352, 2014.

Nakashiba T, Young JZ, McHugh TJ, Buhl DL, Tonegawa S. Transgenic inhibition of synaptic transmission reveals role of CA3 output in hippocampal learning. *Science* 319: 1260–1264, 2008.

Nan X, Hou J, Maclean A, Nasir J, Lafuente MJ, Shu X, Kriaucionis S, Bird A. Interaction between chromatin proteins MECP2 and ATRX is disrupted by mutations that cause inherited mental retardation. *Proceedings of the National Academy of Sciences* 104: 2709–2714, 2007.

Nogami T, Beppu H, Tokoro T, Moriguchi S, Shioda N, Fukunaga K, Ohtsuka T, Ishii Y, Sasahara M, Shimada Y. Reduced expression of the ATRX gene, a chromatin-remodeling factor, causes hippocampal dysfunction in mice. *Hippocampus* 21: 678–687, 2011.

Palaniappan C, Ramalingam R. Deciphering the Molecular Effects of Mutations on ATRX Cause ATRX Syndrome: A Molecular Dynamics Study. *Journal of cellular biochemistry* 118: 3318–3327, 2017.

Patja K, Iivanainen M, Vesala H, Oksanen H, Ruoppila I. Life expectancy of people with intellectual disability: a 35-year follow-up study. *Journal of intellectual disability research* 44: 591–599, 2000.

Pelkey KA, Chittajallu R, Craig MT, Tricoire L, Wester JC, McBain CJ. Hippocampal GABAergic Inhibitory Interneurons. *Physiol Rev* 97: 1619–1747, 2017.

Picketts DJ, Higgs DR, Bachoo S, Blake DJ, Quarrell OW, Gibbons RJ. ATRX encodes a novel member of the SNF2 family of proteins: mutations point to a common mechanism underlying the ATR-X syndrome. *Human molecular genetics* 5: 1899–1907, 1996.

Picketts DJ, Tastan AO, Higgs DR, Gibbons RJ. Comparison of the human and murine ATRX gene identifies highly conserved, functionally important domains. *Mammalian genome* 9: 400–403, 1998.

Ramón y Cajal S. Histogénèse du cervelet. In *Histologie du Système Nerveux de l'Homme et des Vertébrés*. Instituto Ramón y Cajal del CSIC Madrid, 1911.

Ratnakumar K, Duarte LF, LeRoy G, Hasson D, Smeets D, Vardabasso C, Bönisch C, Zeng T, Xiang B, Zhang DY. ATRX-mediated chromatin association of histone variant macroH2A1 regulates α -globin expression. *Genes & development* 26: 433–438, 2012.

Raymond CR. LTP forms 1, 2 and 3: different mechanisms for the ‘long’ in long-term potentiation. *Trends in neurosciences* 30: 167–175, 2007.

Saha A, Wittmeyer J, Cairns BR. Chromatin remodeling by RSC involves ATP-dependent DNA translocation. *Genes & development* 16: 2120–2134, 2002.

Schenkel LC, Kernohan KD, McBride A, Reina D, Hodge A, Ainsworth PJ, Rodenhiser DI, Pare G, Bérubé NG, Skinner C, Boycott K, Schwartz C, Sadikovic B. Identification of epigenetic signature associated with alpha thalassemia/mental retardation X-linked syndrome. *Epigenetics & chromatin* 10: 10, 2017.

Schulz PE, Cook EP, Johnston D. Changes in paired-pulse facilitation suggest presynaptic involvement in long-term potentiation. *Journal of Neuroscience* 14: 5325–5337, 1994.

Scoville WB, Milner B. Loss of recent memory after bilateral hippocampal lesions. *Journal of neurology, neurosurgery, and psychiatry* 20: 11, 1957.

Seah C, Levy MA, Jiang Y, Mokhtarzada S, Higgs DR, Gibbons RJ, Bérubé NG. Neuronal death resulting from targeted disruption of the Snf2 protein ATRX is mediated by p53. *Journal of Neuroscience* 28: 12570–12580, 2008.

Shinohara Y, Hosoya A, Yahagi K, Ferecskó AS, Yaguchi K, Sík A, Itakura M, Takahashi M, Hirase H. Hippocampal CA3 and CA2 have distinct bilateral innervation patterns to CA1 in rodents. *European Journal of Neuroscience* 35: 702–710, 2012.

Shonesy BC, Jalan-Sakrikar N, Cavener VS, Colbran RJ. CaMKII: a molecular substrate for synaptic plasticity and memory. *Prog Mol Biol Transl Sci* 122: 61–87, 2014.

Similä S, von Wendt L, Rantakallio P. Kehitysvammaisten kuolleisuus lapsuusiässä/Mortality among mentally retarded children up to 18 years of age. *Sosiaalilääketieteellinen aikakauslehti. Journal of Social Medicine* 24: 33–39, 1987.

Soderling TR, Derkach VA. Postsynaptic protein phosphorylation and LTP. *Trends in neurosciences* 23: 75–80, 2000.

Song I, Huganir RL. Regulation of AMPA receptors during synaptic plasticity. *Trends in neurosciences* 25: 578–588, 2002.

Squire LR, Zola-Morgan M. The cognitive neuroscience of human memory since HM. *Annual review of neuroscience* 34: 259–288, 2011.

Stayton CL, Dabovic B, Gulisano M, Gecz J, Broccoll V, Glovanazzl S, Bossolasco M, Monaco L, Rastan S, Boncinelli E. Cloning and characterization of a new human Xq13 gene, encoding a putative helicase. *Human molecular genetics* 3: 1957–1964, 1994.

Stevenson RE. Alpha-thalassemia X-linked intellectual disability syndrome. In: *GeneReviews*®[Internet]. University of Washington, Seattle, 2014.

Stevenson RE, Schwartz CE, Rogers RC. *Atlas of X-linked intellectual disability syndromes.* Oxford University Press, 2012.

Tang J, Wu S, Liu H, Stratt R, Barak OG, Shiekhattar R, Picketts DJ, Yang X. A novel transcription regulatory complex containing death domain-associated protein and the ATR-X syndrome protein. *Journal of Biological Chemistry* 279: 20369–20377, 2004.

Torii S, Egan DA, Evans RA, Reed JC. Human Daxx regulates Fas-induced apoptosis from nuclear PML oncogenic domains (PODs). *The EMBO journal* 18: 6037–6049, 1999.

Tsien JZ, Chen DF, Gerber D, Tom C, Mercer EH, Anderson DJ, Mayford M, Kandel ER, Tonegawa S. Subregion-and cell type–restricted gene knockout in mouse brain. *Cell* 87: 1317–1326, 1996.

Villard L, Fontes M. Alpha-thalassemia/mental retardation syndrome, X-Linked (ATR-X, MIM #301040, ATR-X/XNP/XH2 gene MIM #300032). *European journal of human genetics* 10: 223–225, 2002.

Villard L, Toutain A, Lossi A-M, Gecz J, Houdayer C, Moraine C, Fontes M. Splicing mutation in the ATR-X gene can lead to a dysmorphic mental retardation phenotype without alpha-thalassemia. *American journal of human genetics* 58: 499, 1996.

Voon HP, Hughes JR, Rode C, Inti A, Jenuwein T, Feil R, Higgs DR, Gibbons RJ. ATRX plays a key role in maintaining silencing at interstitial heterochromatic loci and imprinted genes. *Cell reports* 11: 405–418, 2015.

Wada T, Sugie H, Fukushima Y, Saitoh S. Non-skewed X-inactivation may cause mental retardation in a female carrier of X-linked alpha-thalassemia/mental retardation syndrome (ATR-X): X-inactivation study of nine female carriers of ATR-X. *American journal of human genetics part A* 138: 18–20, 2005.

Watson LA, Solomon LA, Li JR, Jiang Y, Edwards M, Shin-ya K, Beier F, Bérubé NG. Atrx deficiency induces telomere dysfunction, endocrine defects, and reduced life span. *The Journal of clinical investigation* 123: 2049–2063, 2013.

Weatherall DJ, Higgs DR, Bunch C, Old JM, Hunt DM, Pressley L, Clegg JB, Bethlenfalvay NC, Sjolin S, Koler RD, Magenis E, Francis J, Bebbington D. Hemoglobin H

disease and mental retardation: a new syndrome or a remarkable coincidence? *New England Journal of Medicine* 305: 607–612, 1981.

White WF, Nadler JV, Hamberger A, Cotman CW, Cummins JT. Glutamate as transmitter of hippocampal perforant path. *Nature* 270: 356, 1977.

Wigström H, Gustafsson B. Postsynaptic control of hippocampal long-term potentiation. *J Physiol* 81: 228–236, 1986.

Wilkie AO, Pembrey ME, Gibbons RJ, Higgs DR, Porteous ME, Burn J, Winter RM. The non-deletion type of alpha thalassaemia/mental retardation: a recognisable dysmorphic syndrome with X linked inheritance. *J Med Genet* 28: 724, 1991.

World Health Organization. ICD-10 guide for mental retardation. http://www.who.int/mental_health/media/en/69.pdf [20 Dec. 2018].

Wu LG, Saggau P. Presynaptic calcium is increased during normal synaptic transmission and paired-pulse facilitation, but not in long-term potentiation in area CA1 of hippocampus. *J Neurosci* 14: 645–654, 1994.

Xie S, Wang Z, Okano M, Nogami M, Li Y, He WW, Okumura K, Li E. Cloning, expression and chromosome locations of the human DNMT3 gene family. *Gene* 236: 87–95, 1999.

Xue Y, Gibbons R, Yan Z, Yang D, McDowell TL, Sechi S, Qin J, Zhou S, Higgs D, Wang W. The ATRX syndrome protein forms a chromatin-remodeling complex with Daxx and localizes in promyelocytic leukemia nuclear bodies. *Proc Natl Acad Sci USA* 100: 10635–10640, 2003.

Yang X, Khosravi-Far R, Chang HY, Baltimore D. Daxx, a novel Fas-binding protein that activates JNK and apoptosis. *Cell* 89: 1067–1076, 1997.

Zola-Morgan S, Squire LR, Amaral DG. Human amnesia and the medial temporal region: enduring memory impairment following a bilateral lesion limited to field CA1 of the hippocampus. *J Neurosci* 6: 2950–2967, 1986.

Zucker RS, Regehr WG. Short-term synaptic plasticity. *Annu Rev Physiol* 64: 355–405, 2002.

Curriculum Vitae

Name: Radu Gugustea

Post-secondary Education and Degrees: The University of Western Ontario
London, Ontario, Canada
2013–2017 B.MSc

The University of Western Ontario
London, Ontario, Canada
2017–2019 M.Sc

Honours and Awards: Western Scholarship of Excellence
2013

Dean’s Honour List
2013–2017

Western Graduate Research Scholarship
2017–2019

Related Work Experience Teaching Assistant
The University of Western Ontario
BIOLOGY 1001B
Jan 2018–April 2018

Teaching Assistant
The University of Western Ontario
PHYSIOLOGY 4710A
Sep 2018–Dec 2018

Publications:

Physiology and Pharmacology Research Day Poster Presentation 2017

Gugustea R, Leung LS. Effect of dopamine on synaptic transmission and long-term potentiation in the distal apical dendrites of a B6-strain mouse hippocampus, 2017.

Southern Ontario Neuroscience Association Poster Presentation 2018

Gugustea R, Tamming RJ, Bérubé NG, Leung LS. Effect of ATRX inactivation on hippocampal synaptic plasticity in mice. Manuscript in preparation, 2018.

London Health Research Day Platform Presentation 2018

Gugustea R, Tamming RJ, Bérubé NG, Leung LS. Effect of ATRX inactivation on hippocampal synaptic plasticity in mice. Manuscript in preparation, 2018.

London Health Research Day Poster Presentation 2019

Gugustea R, Tamming RJ, Bérubé NG, Leung LS. Effect of ATRX inactivation on hippocampal synaptic plasticity in mice. Manuscript in preparation, 2019.